3-2004

Stress corrosion cracking studies

K. S. Raja

S. Namjoshi

Amy J. Smiecinski
University of Nevada, Las Vegas, smiecins@unlv.nevada.edu

FINAL TECHNICAL REPORT

STRESS CORROSION CRACKING STUDIES

TASK NO. 17
Document ID: TR-03-007
SIP No: SIP-UNR-014
Final Report: Revision 1

Originator: [redacted]
K. S. Raja U. — 03/16/04 Date

Approvals:

[redacted]
Technical Reviewer, S. Namjoshi — 3/16/04 Approval Date

[redacted]
Principal Investigator, S. Namjoshi — 3/16/04 Approval Date

[redacted]
QA Manager, A. Smiecinski — 3-17-04 Approval Date

REVISION HISTORY

Revision Number	Effective Date	Reason for Change
0	02/23/2004	Initial Issue
1	03/17/2004	Inserted acknowledgments. Added opening paragraph to Subsections 2-5 to clarify their final status. Changed subsections 2 and 4 subheadings to "Method Development/Corroborative Work" and "Corroborative Data - For Information Only" to tables and figures of these subsections.

TABLE OF CONTENTS

LIST OF TABLES

LIST OF FIGURES

Acknowledgement

We would like to acknowledge the advice and support from Dr. Gerald Gordon and Dr. Pasu Pasupathi of Bechtel-SAIC Company LLC, Dr. Raul Rebak, Dr. Frank Wong & Dr. Tiangan Lian of Lawrence Livermore National Laboratory, Paige Russell of the DOE, Bob Fish of Booz-Allen & Hamilton Inc., and Dr. Digby Macdonald of Pennsylvania State University. We would also like to thank Amy Smiecinski, Morrie Roosa, Terry Mueller, Robert Fulwider, Raymond Keeler, and Barbara Roosa of the UCCSN Quality Assurance Program for their continuous guidance and helpful editorial reviews of reports. We are thankful to Dr. Manoranjan Misra, Dr. Jeff LaCombe, and Dr. S. Chen of the University of Nevada Reno for helping with the project management, technical report writing, and consulting during the illness and after the death of the PI Dr. Denny Jones. Finally, the financial support from the Department of Energy through the Harry Reid Center is gratefully acknowledged without which none of this work would have been possible.

Summary

This document reports on the activities for Task 17 of the U.S. DOE/UCCSN Cooperative Agreement Number DE-FC28-98NV12081. There are three subtasks in this Task, the experimental results, discussions, and conclusions of which are presented in the following sections.

Data Sources and Electronic Data Control

The Data Identification numbers for the data, graphs, and tables in this report, as submitted to the Data Management Database, are tabulated below. The table also includes the source files for the said data as well as the corresponding scientific notebooks where the data can be found.

All data in the Q section of the report are qualified as the relevant notebooks have completed the Technical and QA review process.

The following Implementing Procedures were used in the course of this work:
IPR-014: User Calibration of Gamry Potentiostat PC3/CMS100
IPR-015: User Calibration of Gamry Potentiostat PC4/30mA/DC105 (Femtostat)
IPR-018: Electrochemical Corrosion Testing
IPR-019: Stress Corrosion Cracking Testing
IPR-020: User Calibration of Gamry Potentiostats PC4/300mA/DC105 and PC4/750mA/DC105
IPR-020: User Calibration of Gamry Potentiostats PC4/300mA/DC105 and PC4/750mA/DC105
IPR-025: User Calibration and Use of the Cole-Parmer/Oakton pH/mV/oC Meter
IPR-026: Constant Load Creep/Environmentally Assisted Cracking Testing

Table of DIN/DIDs, Source Files and Corresponding Notebooks For Task 17

#	DTN/DID	Source File	SN
Table 1.1	017KR.008	Fig 1-3.xls, Fig 1-4.xls, Fig 1-9.xls, Fig 1-10 & 1-11.xls, Fig 1-12 to 1-15.xls	UNR 028 vol.5, UNR 028 vol.7
Fig. 1.1	Not Applicable	Schematic	Not Applicable
Fig. 1.2	017KR.008	Fig 1-2.xls	UNR 028 vol.5
Fig. 1.3	017KR.008	Fig 1-3.xls	UNR 028 vol.5
Fig. 1.4	017KR.008	Fig 1-4.xls	UNR 028 vol.5
Fig. 1.5	017KR.008	Fig 1-5.xls	UNR 028 vol.7
Fig. 1.6	017KR.008	Fig 1-6.xls	UNR 028 vol.7
Fig. 1.7	017KR.008	Fig 1-7.xls	UNR 028 vol.5
Fig. 1.8	017KR.008	Fig 1-8.xls	UNR 028 vol.5
Fig. 1.9	017KR.008	Fig 1-9.xls	UNR 028 vol.7
Fig 1-10 Fig.1-11	017KR.008	Fig 1-10 & 1-11.xls	UNR 028 vol.7
Fig 1-12 Fig 1-13 Fig 1-14 Fig 1-15	017KR.008	Fig 1-12 to 1-15.xls	UNR 028 vol.5
Table 2.1	017KR.009 017KR.004	Carrier Charge Density and Film Thickness are in file "**Table 2-2.xls**" – 017KR.009. The Current Decay Exponent is calculated from files, "**Comparison of OCRE&PS data of 304.xls**", and "**Comparison of OCRE&PS data of alloy-22.xls**" from 017KR.004.	UNR 028 vol.2
Fig. 2.1	Not Applicable	Schematic	Not Applicable
Fig 2.2	017KR.004	Polarization curves of 304&alloy22 in 1 N H2SO4.xls	UNR 028 vol.2
Fig. 2.3	017KR.004	Comparison of OCRE&PS data of 304.xls	UNR 028 vol.2
Fig. 2.4	Not Applicable	Schematic fig.	UNR 028 vol.2
Fig. 2.5	017KR.004	Comparison of OCRE&PS data of alloy-22.xls	UNR 028 vol.2
Fig. 2.6	017KR.004	Comparison of OCRE results of 304 & alloy-22.xls	UNR 028

			vol.2
Fig. 2.7	017KR.004	MS plots of passivated 304.xls	UNR 028 vol.2
Fig. 2.8	017KR.004	MS plots of passivated alloy-22.xls	UNR 028 vol.2
Fig. 3.1	017KR.009	Schematic	-NA-
Fig. 3.2	017KR.009	Schematic	-NA-
Fig. 3.3	017KR.009	Figures3.3.xls	UNR 028 vol.4
Fig. 3.4 Fig. 3.5 Fig. 3.6	017KR.009	Figures3.4-3.6.xls	UNR 028 vol.4
Fig. 3.7 Fig. 3.8 Fig. 3.9	017KR.009	Figures3.7-3.9.xls	UNR 028 vol.4
Fig. 3.10a Fig 3.10b	017KR.009	Figures3.10.xls	UNR 028 vol.4
Fig. 3.11	Not Applicable	Schematic	Not Applicable
Fig. 4.1a Fig. 4.1c Fig. 4.1c	Not Applicable	Schematic/Photograph of Experimental setup	Not Applicable
Fig. 4.2 Fig. 4.3 Fig. 4.4	017KR.009	Fig 4-2 to4-4.xls	UNR 028 vol.5
Fig. 4.5	017KR.009	Fig 4-5.xls	UNR 028 vol.5
Fig. 4.6	017KR.009	Fig 4-6.xls	UNR 028 vol.5
Fig. 4.7	017KR.009	Fig 4-7.xls	UNR 028 vol.7
Fig. 4.8a Fig. 4.8b Fig. 4.8c Fig. 4.8d	017KR.009	Fig 4-8a to 4-8d.xls	UNR 028 vol.5
Fig. 4.9a Fig. 4.9b Fig. 4.9c	017KR.009	Fig 4-9a to 4-9c.xls	UNR 028 vol.7
Fig. 5.1	Not Applicable	Schematic (Example of power law relationship for earthquakes with a threshold (M=1) imposed on lower magnitudes)	Not Applicable
Fig. 5.2	Not Applicable	Schematic (Examples of earthquake recurrence curves using a = 3.0 and b = 1.0 in the recurrence relation.)	Not Applicable
Fig. 5.3	017SN.001	10000-year catalog of predicted significant seismic events at Yucca Mountain.dat	Not Applicable

		The figure is generated by cumulatively counting the frequency of occurrence of the Moment magnitude data in column 3 of the above file and plotting it as the number of occurrences vs the magnitude. For example, the number of earthquakes of magnitude 3 or larger is ~ 10,000 (1×10^5) while the number of earthquakes of magnitude 10 or larger is ~ 10 (1×10^1)	
Fig. 5.4	017SN.001	10000-year catalog of predicted significant seismic events at Yucca Mountain.dat The figure is generated by cumulatively counting the frequency of occurrence of the Predicted peak ground accelerations (PGA) data in column 6 of the above file and plotting it as the number of occurrences vs the log of the magnitude of the PGA. For example, the number of earthquakes of peak ground accelerations of magnitude 10^{-6} m/s^2 or larger is ~ 10,000, while the number of earthquakes of peak ground accelerations of magnitude 10^{-1} m/s^2 or larger is ~ 40	Not Applicable
Fig. 5.5	017SN.001	10000-year catalog of predicted significant seismic events at Yucca Mountain.dat The figure is generated by cumulatively counting the frequency of occurrence of the duration of earthquakes data in column 8 of the above file and plotting it as the number of occurrences vs duration in seconds. For example, the number of earthquakes of duration 200 seconds or greater is ~ 200, while the number of earthquakes of duration 600 seconds or greater is ~ 10	Not Applicable

Q-SECTION

1. SUBTASK 1b - Plasticity Enhanced by High Anodic Current Densities at Film Rupture Sites

1.1 Introduction

Jones[1,2] has proposed a model describing the unified mechanism of stress corrosion cracking. This model proposes that brittle crack initiation could occur due to the development of a local plastic region beneath the passive film rupture sites (FRS). The FRS are believed to be mechanically constrained by surrounding rigid metal covered by passive film. Anodic dissolution at the film rupture sites generates divacancies, which annihilate strain hardening and promote local plastic regions at the near-surface volume of the slip bands. It is expected that the vacancy-dislocation interaction, leading to relief of strain hardening, would result in increased creep strain[2]. Many researchers have observed the correlation between creep and Stress Corrosion Cracking (SCC). Andresen and Ford's model on SCC crack growth[3], considers the rupture of passive film to occur due to the accumulation of creep strain. Was and co-workers[4,5,6] have also considered creep as a predominant factor controlling SCC of Alloy 600 components in pressurized water reactor environments. An increased steady-state creep rate was observed in water compared to an argon (inert) environment at 360°C[5].

In SCC studies of austenitic and ferritic stainless steels in 0.83 M H_2SO_4 and 0.83 M HCl solutions at 80°C, Nishimura and co-workers observed a correlation between steady state creep rate and SCC failure time[7,8,9,10]. The deformation of specimens exposed to corrosive environments revealed three regions of creep similar to those of high temperature creep. The three regions observed were: 1) primary creep region (controlled by applied stress and considered as the crack incubation period), 2) secondary creep region (which showed a steady state elongation correlated to the crack induction process), and 3) tertiary creep region (which occurred due to crack propagation and reduction in the net-cross section leading to fracture). SCC failures on a laboratory scale required a minimum steady state creep rate of 10^{-10} m/s.

The effect of impressed anodic and cathodic currents on the creep behavior of thin copper wire in deaerated acetate buffer solutions was studied by Revie and Uhlig[11]. In the

---

[1] D.A Jones, Metall. Trans. 16A (1985) 1133
[2] D. A. Jones, Corrosion 52 (1996) 356
[3] P.L.Andresen and F. P. Ford, Mater. Sci and Eng., A103(1988)167
[4] G. S. Was, J. K. Sung and T. M. Angeliu, Metall. and Materials Trans. 23A (1992) 3343
[5] T. M. Angeliu and G. S. Was, Metall. And Materials Trans. 25A (1994) 1169
[6] V. Thaveeprungsriporn, G. S. Was, Metall. And Materials Trans. 28A (1997) 2101
[7] R. Nishimura, Corrosion 46(1990) 311-318
[8] R. Nishimura, Corrosion 48 (1992) 882-890
[9] R. Nishimura, Corrosion 49 (1993) 796- 801
[10] R. Nishimura and Y. Maeda, Corrosion Sci., 45 (2003) 1847-1862
[11] R. W. Revie and H. H. Uhlig, Acta Metall., 22 (1974) 619

absence of corrosion, as in the case of ambient air, the creep strain followed a logarithmic relation with time. However, when an external anodic current (0.9 mA/cm^2, corresponding to a dissolution rate of 0.33 nm/s) was impressed on the specimens under a tensile load, the creep rate increased by several folds. Similar effects were observed for impressed cathodic currents as well.

Although, low temperature creep is not a predominant failure mechanism for engineering components not exposed to corrosive environments, creep strain has been associated with SCC failures. Therefore in order to understand its effect on SCC, it is important to study the low temperature creep behavior of Alloy-22 in corrosive environments. In general, SCC is reported to occur over a range of electrochemical potentials, at which passivity is observed. In the presence of dissolved oxidizers, the corrosion potential of an ambient environment drifts in the noble direction. Therefore, creep experiments conducted under constant electrochemical potentials may not represent actual environmental conditions. In order to investigate the passivation behavior by simulating the enoblement/drifting of potential in the presence of dissolved oxidizers, an open circuit reference electrode (OCRE) technique was proposed[12]. In this technique, the potential of the working electrode (WE) in a de-aerated environment is potentiostatically controlled to follow the corrosion potential of a reference electrode (RE). The RE is identical to the WE in chemistry and geometry and is exposed to the environment with dissolved oxidizers.

Therefore, the objectives of this study are:
1) a) To investigate the creep behavior of Alloy-22 in chloride containing environments and b) to correlate the observed current transients to the creep elongation with crack initiation events.
2) To compare the creep-corrosion interaction in 304-SS in chloride containing environments , as it is expected that SCC could be observed in 304-SS but not in Alloy-22.
3) To understand the role of vacancy flux (created during corrosion processes) on the creep deformation and its implication on SCC.

1.2 Experimental

Material
Alloy-22 was investigated in mill-annealed condition (27-339670-01 Hastelloy C-22 Plate Heat # 2277-1-3148.75, Tested and approved by Laboratory Testing Inc. Certificate # UNR001-02-02-03568). The chemical composition of the wrought material used in this investigation with a yield strength of ~53800 psi, was:
Cr - 21.70 %
Mo - 13.10 %
Fe - 03.50 %
W - 02.80 %
Co - 01.30 %
Mn - 00.24 %

[12] K. S. Raja and D. A. Jones, "Continuous Passive Current Measurements of Stainless Alloys In Simulated Oxygenated Conditions Using An Open Circuit Reference Electrode" Paper # 03396 Corrosion 2003, NACE.

V - 00.15 %
Si - 00.03 %
P - 00.01 %
C - 0.002 %
S - <0.01 % and
Ni - Remainder

Tensile Specimen
Tensile specimens with a gage length of 25.4 mm (1.0 in) and gage diameter of 5.1 mm (0.2 in) were machined out of the as-received plate stock. Detailed specimen dimensions are shown in figure 1.1(a). A thin epoxy coating was used to mask the specimen shoulders to avoid any type of crevice corrosion between the O-ring seal and the metal surface. The gage length of the specimen was polished down to 600 grit (using emery paper), and thoroughly washed with alcohol and distilled water before introducing it into the electrochemical cell.

Environment
The creep tests of Alloy-22 were carried out in 3.9 M NaCl + 0.1 M HCl solution at 80°C. A PID temperature controller and a J-type thermocouple were used to control temperatures.

Electrochemical Cell
The electrochemical test cell, figure 1.1(b), has a 130 mm diameter, is 100 mm long, with a 7 mm thick wall glass tube secured between two 12.5 mm thick PTFE circular lids. Four 4 mm diameter stainless steel tie rods are used to secure the circular lids. Two O-rings provide a leak proof seal between the flat ends of the glass tube and the PTFE lids. The PTFE lid provided the required number of ports to accommodate the following: tensile specimen, counter electrode (2 mm Pt rod), reference electrode (Ag/AgCl), heating element, gas purge, thermocouple, and a condenser. An extra port was provided to accommodate the open-circuit reference electrode (OCRE). The OCRE technique was used to study the current transient behavior of the creeping specimen. The corrosion potential of the stressed specimens (WE) was polarized to follow the potential of the open circuit reference electrode (OCRE), which was an unstressed specimen with identical material conditions. The OCRE, an 11 mm diameter and 100 mm long cylindrical rod, was immersed to about 50 mm in the environment with dissolved oxygen. It should be noted that, the only difference between the WE and the OCRE was that the OCRE was in an unstressed condition. The environments for the WE and OCRE were identical. The solution was heated with a quartz heating element (16 mm dia. and 75 mm heating length, Glo-quartz, Tucson, AZ)

Creep Loading Frame
Constant load type creep frames (Applied Test System, PA) with a lever-arm ratio of 20 were used for creep studies (Fig. 1.1(c)). The weights in the loading pan and the resulting load on the specimens were calibrated against a NIST certified load cell using standard QA procedures (Bechtel Nevada). The error in the load calculations using a magnification factor of 20 was less than 0.2 % between 0-20000 lbs. The loading lever was maintained in the horizontal position as the specimen deformed with the help of a

magnetic-level relay circuit. The lever adjusted itself to the initial horizontal position to the ground for every 0.08 mm elongation of the specimen.

Measurement of Deformation

Creep deformation was measured using a plunger-type digital indicator with a least count of 0.01 mm (Mitutoyo, Digimatic Model-S1012E). The digital indicator was mounted on a low-alloy steel bracket, which was secured to the end of one shoulder of the specimen using two nuts. The plunger of the indicator was activated by attaching a long cylindrical rod-bracket assembly to the other end of the shoulder of the specimen. Thus, the extension of the specimen recorded included not only the extension of the gage length but also the entire length of the specimen excluding the threaded portions. As the diameter of the specimen shoulder was more than two times of the gage diameter, the observed creep elongation could be attributed only to the reduced cross section.

Constant Load Creep Testing Under Electrochemical Conditions

Constant-load creep tests were carried out on Alloy-22 mill-annealed (as received) specimens in different electrochemical conditions viz., 1. under an applied constant potential, 2. under an applied constant current (galvanostatic) and 3. under the OCRE condition. In the OCRE condition, the free corrosion potential of the unstressed specimen is duplicated as the corrosion potential of the stressed creep tensile specimen. As mentioned before, the OCRE specimen has identical chemistry and geometry to that of creep specimen. For the OCRE test condition, the connection of the potentiostat to the electrochemical cell is as follows: the WE (creep tensile specimen) is connected to the WE terminal of the potentiostat, the platinum counter electrode (CE) is connected to the auxiliary electrode lead, and the OCRE (unstressed identical material specimen) is connected to the reference lead of the potentiostat. In order to duplicate the corrosion potential of the OCRE in the WE, the applied potential is set to zero with respect to the reference electrode (OCRE) in the potentiostatic menu.

Before loading, the specimen is conditioned at a predetermined constant potential or current or at the OCRE condition for about an hour. If the specimen is passivated at a constant potential, a sufficient length of time is allowed to pass so that a quasi steady state passive current value is reached before stressing the specimen. Typically, a 5μA current value was used as a measure for assuming that the quasi-steady state was achieved. After reaching a quasi steady state current (in case of potentiostatic or OCRE conditions) or potential (in galvanostatic condition), the specimen is loaded to the required stress level by adding weights to the weight pan of the creep frame. The creep frame has lever-arm ratio of 20:1, which means that 1 lb in the weight pan results in a load of 20 lbs on the specimen.

In this investigation, the specimens were potentiostatically passivated at +400 mV and + 100 mV (vs. Ag/AgCl).. Galvanostatic creep tests were carried out at applied constant current values of +1mA & +10 mA (anodic), and -1 mA and -10 mA (cathodic). Creep tests in OCRE conditions also were carried out at 90 and 110 % of yield strength levels. The weight required on the pan is calculated as:

$$W = (SxA)/R \quad (1.1)$$

where, W = weight on the pan, pounds, S = required stress on the specimen, in psi, A = Area of the specimen gage cross section, in square inches, and R = lever arm ratio, (20:1 in this case). Any extra tare weight required for balancing the arm at zero load should be added to the calculated weight, W.

The calculations for the above are shown below:
The average yield strength of Alloy-22 = 53800 psi
Gage diameter = 0.2 inch
Area of cross section of the gage: $\pi D^2/4$ = 0.031416 sq.in or 20.27 mm^2
Load corresponding to yield = 53800*0.031416 = 1690 lbs ~1700 lbs
Load Corresponding to ~90% yield strength: 1700*0.9 = 1530 lbs ~1500lbs
Load Corresponding to ~110 % yield: 1700*1.1 = 1870 lbs ~1900lbs

The creep elongation measurement started as soon as the specimen was loaded in increments of 600 lbs. Immediately after loading the specimens to the desired stress level (generally varied from 90 – 110 % of the yield strength), the specimen deformed at a faster rate. The change in dial indicator reading was noted for every 15 seconds during initial hour after loading. When the deformation rate slowed down, the time taken for every 0.01 mm elongation was noted.

1.3 Results

Fig. 1.2 shows the results of the constant load creep tests under OCRE conditions at two initial stress levels corresponding to 90 and 110% of the 0.2% yield strength (YS) of Alloy-22. The creep strain is plotted on a linear scale while the corrosion current and time are plotted on a logarithmic scale. The total strain recorded during creep consists of elastic and inelastic strain. Inelastic strain includes both the instantaneous plastic and the time dependant creep strain. Time dependant inelastic strain was observed on the specimen loaded below the yield strength of the material. As the specimens were loaded abruptly to the desired load levels, very high plastic strains were observed. About 2.4% strain was observed on the specimen loaded to 90% YS and 7.8% strain was observed on the specimen loaded to 110% YS. The higher strains observed could be partly attributed to the higher corrosion currents. After exhaustion of primary creep, secondary creep was observed to have a linear relationship with logarithmic time. This semi-logarithmic relation indicates that the creep strain rate decreases with increasing time. The rate of deformation was observed to be higher immediately after loading and the creep rate decreased with time at a constant load. At the 110% YS stress level, the initial strain was observed to be greater than that of the 90% YS stress level. However, the creep behavior of Alloy-22 was found to be almost similar at both stress levels. Corrosion currents recorded during the creep process are shown in figure 1.2. The current has positive values and is therefore anodic. Based on the potentiostatic circuit, it should be noted that this current passes from the creep specimen to the auxiliary Pt electrode because of the corrosion processes. As the potential of the creep specimen was maintained at the potential of an unstressed Alloy-22 specimen (OCRE), the recorded anodic current

indicates anodic polarization of the creep specimen. Corrosion potential of the creep specimen could be more active in a stressed condition as compared to the unstressed condition. The change in corrosion potential due to stress can be expressed as

$$dE = -\sigma V_m/zF\ , \tag{1.2}$$

where, σ = tensile stress, Vm = molar volume, z = number of charge transfer, and F = Faraday's constant. The corrosion current observed due to anodic polarization could be attributed to the dissolution at the film rupture sites. The observed behavior of the anodic current as a function of creep strain/time is shown in figure 1.2. A direct relation could not be observed between the film fracture associated creep strain and the corrosion current. However, the final plateau or decrease in current could be attributed to formation of a dark colored film on specimen surfaces.

Fig. 1.3 and 1.4 illustrate on a logarithmic scale, variation of the creep strain rate with time at 90 and 110% YS loads respectively. A linear relation could be observed with a slope of -0.9 for 90% YS and -0.94 for 110 % YS load. For the 90% YS load condition, the initial creep rate was $8x10^{-4}$/s and it decreased logarithmically with time to a value of 9.8×10^{-9}/s after 233.5 hours of creep. For the 110% YS load condition the initial creep rate was $6.5x10^{-4}$/s and it decreased to 1.4×10^{-8}/s after 235 hours of creep.

Decreasing creep rate with time indicates a logarithmic creep strain relation expressed as

$$\varepsilon = \varepsilon_0 + \alpha \log(1+\beta t) \tag{1.3}$$

or alternatively

$$\varepsilon_c = \alpha \ln t + \beta \tag{1.4}$$

Differentiating (1.4) with respect to time yields

$$\dot{\varepsilon}_c = \frac{\alpha'}{t} \tag{1.4.1}$$

and taking logarithms on both side gives:

$$\log(\text{strain rate}) = \text{Constant} - \log(\text{time}) \tag{1.5}$$

A linear relationship between logarithmic creep strain rate and logarithmic time with a decreasing slope has been observed for a large number of metals and alloys at low temperatures (without aqueous corrosive environments). The initially observed higher strain rate is associated with larger density and higher velocity of mobile dislocations. The semi-logarithmic relation of creep strain with time is attributed to the strain hardening behavior of the material[13]. Strain hardening occurs because the mobile dislocations are trapped due to interactions with other dislocations probably forming a network, or due to Lomer-Cottrell barriers. Dislocation pile-ups at the barrier caused back stress and increase the drag force for un-trapped mobile dislocations decreasing their

[13] S. Usami, T. Mori, Cryogenics, 40 (2000) 117-126

velocity. The slightly steeper slope of creep strain rate vs time for 110% YS load indicates a larger drag on the mobile dislocations with increased loading.

Fig. 1.5 shows the results of creep testing of Alloy-22 potentiostatically passivated at 100 mV (Ag/AgCl), with two different constant load conditions. The results are presented as strain vs time and corrosion current during creep vs time plots. The specimen was passivated at 100 mV for 5700 seconds before loading the specimen to 90% of its yield strength . The strain recorded immediately after loading was about 1.135%. The insets in figure 1.5 show magnified views of region when loads were applied or increased. It can be seen that there was no increase in current in spite of considerable amount of plastic strain noted on the specimen. The creep strain increased with time following a semi-logarithmic relation, which resulted in a decrease in strain rate with time. During the constant load creep tests of the Alloy-22 specimen, passivated at 100 mV, the corrosion current decayed continuously. Figure 1.6 shows the current decay behavior on a log-log scale. The slope of the current transient during the no-load condition was -0.58 (during the initial 3000 seconds) and it decreased to -0.31 during creep. The decrease in slope of the current transient could be attributed to dislocation/vacancy interactions delaying the repassivation process. No correlation between current spikes and creep strain could be observed and this could be attributed to the absence of any crack initiation process in Alloy-22 in 3.9 M NaCl + 0.1 M HCl solution.

Fig. 1.7 shows the relation of creep strain and corrosion current with time during creep testing of Alloy-22 specimen passivated at 400 mV in 3.9 M NaCl +0.1 M HCl solution at 80°C. When the specimen was loaded to 90% of YS, an instantaneous strain of about 2% was observed and the creep strain increased with the constant load. The specimen was in the passive condition for more than an hour when the abrupt loading was started. As shown in figure 1.7, the plastic strain in the specimen due to the relatively higher loading rate did not increase the corrosion current. Small current peaks were observed after loading but they decayed at a fast rate and reached the base/steady-state value quickly. Figure 1.8 shows the current transient vs time during creep, on a log-log scale. When the specimen was not loaded the log-log plot of the current transient (passive current of Alloy-22 at 400 mV) showed a slope of -0.72. However, the slope decreased to -0.437 when the specimen was loaded to 1500 lbs and allowed to creep.

Fig. 1.9 shows the log-log plot of creep strain rate vs time for the 90% YS load condition. The creep rate initially at about 7×10^{-5}/s decreased to about 4.5×10^{-9}/s after 72 hours of creep. After reaching this low rate of creep strain, the load on the specimen was increased to 1900 lbs, which corresponds to 110% of yield strength of the material (w.r.t the initial cross section). It should be noted that this load would be higher than the expected 110% YS load as the specimen had already crept to 3.3% strain and there would be a corresponding reduction in the cross sectional area. However, the actual 3.6% increase in the initial applied stress against the intended load is considered to be within the experimental scatter of ±10% in these kinds of experiments. With the increase in load to above the yield point, there was an instantaneous increase in strain. It is predicted that an abrupt increase in the load, activates the trapped dislocations. As shown in figure 1.10, this results in an immediate increase in the creep strain rate to 3.7×10^{-4}/s. However, as

seen in figures 1.5 and 1.6, no increase in corrosion current could be observed. Similar to previous experiments, the creep rate decreased with time and after 86 hours of creep reached a value of 4.41 x 10^{-9}/s. The slope of the log-log plot of creep strain rate vs time was steeper than -1. When the creep strain rate dropped to very low values (4.4 x 10^{-9}/s) (at 1900 lbs load under 100 mV potentiostatically passivated condition), the electrochemical condition was changed. This was done by cathodically charging the specimen at -1 mA for 31 h, -10 mA for 70 h and -100 mA for 40 h. Figure 1.5 shows the increase in the creep strain with cathodic current charging With cathodic charging of -1 mA, the creep strain rate initially increased to 8.4x10^{-8}/s. However, there was no increase in the creep strain rate with continued cathodic current charging or with an increase in the charging current. As shown in figure 1.11, the creep rate decreased to a value of 1.2 x 10^{-8}/s with time. This result indicates that hydrogen charging did not result in continuous activation of the immobile dislocations.

As in the previous tests, the creep strain rate of the specimen passivated at 400 mV also decayed with time as shown in figures 1.12, 1.13, and 1.14. The initial creep strain rate of 1.26 x 10^{-4}/s decreased to 6.2 x 10^{-8}/s after 22 h of creep at 1500 lbs (figure 1.12). When the creep strain rate dropped to 6.2 x 10^{-8}/s at 1500 lbs, the load was increased to 1700 lbs (equivalent to the YS of the specimen w.r.t. original cross section). Figure 1.7 shows the resultant creep strain and current as functions of time. Upon increasing the load, the immobile dislocations were reactivated and the creep strain rate increased to 3.37 x 10^{-4}/s. Figure 1.13 shows the linear relationship between creep strain rate and time on a log-log scale. As before, the slope of the plot is approximately –1. The creep strain rate decreased with time and reached a value of 2.19 x 10^{-8}/s after 45.5 hours of creep. When the load on the specimen was further increased to 1900 lbs under the same potentiostatic conditions, the creep rate increased to the initial value of about 1.93 x 10^{-4}/s and decayed with time to 4.3 x 10^{-9}/s after 140 h of creep, as shown in figure 1.14. The corrosion current during creep was observed to reach a plateau after decaying during the initial test period. Current spikes could be observed during the test, which could potentially be due to some form of crevice corrosion between the O-ring and the specimen. The current transients could not be attributed to any crack initiation events, as no cracks were observed by visual inspection or optical/scanning electron microscopy. When the creep strain rate reached a very low value of 4.3 x 10^{-9} /s, the potentiostatic control of the creep specimen was changed to a galvanostatic control condition by applying a 1 mA current, without altering the load condition. Figures 1.7 and 1.15 show the results of creep strain measurements for different applied anodic currents (1 and 10 mA). There was a clear increase in the creep strain rate with the higher impressed anodic currents. The average creep strain rate increased to 6.5x10^{-8}/s, which is an order of magnitude increase as compared to the value observed prior to the galvanostatic condition. This increase in creep strain rate, which occurred without any change in loading could be attributed to the vacancies generated during the corrosion processes due to the applied anodic current. It should be noted that the reduction in cross section due to anodic current was insignificant.

1.4 Discussion

1.4.1 Creep-SCC Correlation

During creep tests, upon loading to the desired levels, there is a very fast increase in the strain observed. Many researchers including Cotrell have also observed these high instantaneous strain rates upon complete application of the desired stress to the specimens[14,15,16]. This occurrence of instantaneous high strain rate when the specimen is loaded to above the yield point and its subsequent decay upon holding the load at the desired value ($d\sigma/dt = 0$), is considered as an evidence that the strain rate has two components: loading strain rate and creep strain rate. It should be noted that in this work the initial instantaneous strain rate could not be determined as the strain increase was noted manually using the digital indicator. According to Alden[14], two kinds of strains are measured during deformation, which are caused by competition between thermal (viscous strain) and mechanical (plastic strain) release of dislocation segments from obstacles and sources. Plastic strain is proposed to be time independent while creep strain is recovery controlled. At a given strain rate, the deformation by plastic strain is accomplished by a small number of mobile dislocations moving at a high speeds[15]. However, in the case of time dependant viscous/creep strain, the dislocation release occurs due to thermal energy and the strain rate is a function of stress, temperature, and time. Viscous creep is glide controlled and viscous flow occurs due to a high density of mobile dislocations moving at lower speeds[14]. Low temperature creep in ambient non corrosive conditions has been observed for austenitic stainless steels at the stress levels as low as 25% of the yield strength[13]. Dislocations are responsible for plastic strain and the dislocation density is considered to be a function of applied stress. The total dislocation density in a material can be expressed as a function of applied stress as[14]:

$$\sigma = \sigma^* + \alpha.G.b.\rho_t^{0.5} \tag{1.6}$$

where, σ = applied stress, σ^*= threshold stress above which dislocations multiply, α = a constant, G = Shear Modulus, and ρ_t = total dislocation density

Generally it is very difficult to measure only the mobile dislocation density.

The creep strain rate is expressed as[15]:

$$\frac{d\varepsilon}{dt} = \rho_m b v \tag{1.7}$$

where, $d\varepsilon/dt$ = strain rate, v= dislocation velocity, b = Burgers vector, and ρ_m = mobile dislocation density

The decrease in creep strain rate with time is attributed to two effects[13,14,15,16], viz., 1. decrease in mobile dislocation density and 2. decrease in velocity of mobile dislocations due to viscous drag. These effects could affect the creep strain rate either individually or together. It has been observed that the mobile dislocation density is affected by the magnitude of stress, stress rate. The stress rate was also observed to affect dislocation velocity[17]. Oehlert and Atrens[17] observed that upon loading specimens at different stress

[14] T. H. Alden, Metall. Trans., 16A (1985) 375-392
[15] T. H. Alden, Metall. Trans., 18A (1987) 51-62
[16] A. H. Cottrell, J. Mech. Phys. Solids 1 (1952-53) 53
[17] A. Oehlert and A. Atrens, Acta Metal. Mater. 31 (1994) 1493-1528

rates to the desired level, the higher loading rates produced higher creep rates. However, in the present investigation, the loading rate (stress rate) was not monitored as weights were added in steps to load the specimen with increments of 600 lbs initially and 300 or 100 lbs thereafter to obtain the desired magnitude. The same procedure was followed in all the tests so that rate of loading was similar for all specimens.

As discussed earlier, decreasing creep strain rate is the result of mobile dislocations being trapped as they interact with other dislocations. The trapped dislocations progressively pile up at dislocation barriers, resulting in strain hardening of the material. These dislocation pile-ups result in a "back-stress", which retards the dislocation movement as a viscous drag acts on the mobile dislocations. In pure metals, like copper, viscous drag has been observed to be low compared to that in stainless steel[15]. The higher viscous drag could be attributed to the presence of solute atoms in substitutional and interstitial sites. It was observed that increased loads resulted in increased values of the decreasing creep rate. Oehlert and Atrens[17] have argued that trapped mobile dislocations may not be reactivated when the stress increased. This argument is based on their observation that the creep strain rate did not change when they unloaded the specimen by 25% and reloaded again back to the original value. According to equation (6), an increase in applied stress should result in increased total dislocation density. This indicates that new dislocations are emitted with an increase in the stress. It is reasonable to assume that these new dislocations are mobile before they get trapped. Overall, during low temperature constant load creep in an ambient non-corrosive environment, the continuous decrease in creep strain rate could be attributed to the strain hardening behavior of the material. In order to have a constant strain rate, the stress should be raised continuously so that the rate of trapping of mobile dislocation is equal to the rate of generation of mobile dislocations provided that the dislocation velocity remains constant. However, with strain hardening, more viscous drag is expected to occur resulting in a decreased mobile dislocation velocity. Therefore for a steady state creep rate, in order to compensate for the decreased mobile dislocation velocity, the density of mobile dislocations should increase with strain hardening. An increase in temperature could help reactivating the trapped mobile dislocations, as the barriers are short range ordered. However when creep occurs in a corrosive environment under active conditions, as investigated by Revie and Uhlig[11], a substantial increase in creep strain rate was observed as compared to that in ambient conditions. Vacancies or divacancies that were created during anodic dissolution diffused into the specimen and interacted with dislocation arrays. Vacancy-dislocation interaction resulted in dislocation climb and easier slip, which increased the creep strain rate during creep process under anodic dissolution conditions.

During OCRE tests in this present investigation, the stressed creep specimens were anodically polarized with respect to their unstressed counterparts. Although the difference between the corrosion potentials of stressed and unstressed specimens would be only a few millivolts, relatively large currents were observed in this study as predicted by the Nernst equation (1.1). During deformation, larger dislocation pile-ups can be expected, as surfaces act as a source of dislocations as well as obstacles for mobile dislocations[18]. At the dislocation pile-ups, the potential at the localized deformation sites

[18] R. M. Latanision and R. W. Staehle, Acta Metallurgica, 17 (1969) 307-319

can be more active than the surface, which is free of dislocation pile-ups. Assuming that there is a planar pile-up of n dislocations, the local deformation potential may be expressed as[19]:

$$\Delta\varphi = \frac{\varepsilon_F n(\mu b)^2 A_1}{6e\pi^2 r^2(1-\upsilon)^2} \tag{1.8}$$

where, $\Delta\varphi$ = deformation potential, εF = Fermi energy, μ = shear modulus, n = number of dislocations in the pile-up, b = Burgers vector, r = radius of dilatation ~ 10 b, υ = Poisson's ratio, e = electronic charge, and A1 = Constant

Assuming 10 dislocations in a pile-up the estimated difference in deformation potential is about -160 mV, for copper[18]. A similar active condition can be expected for Alloy-22, causing high local corrosion currents. However, the high corrosion current observed for Alloy-22 did not result either in a steady state or increased creep rate. The observed negative slope of creep strain rate vs time on a log-log scale indicates that the vacancies created during metal dissolution do not aid easy slip. Different reasons could be attributed to the absence of acceleration of creep. However, it should be noted that the slopes of the log stain rate vs log time plot of OCRE test conditions were marginally shallower than the generally reported slope of -1 for creep process in air for stainless steels[13] and the slopes of Alloy-22 in passivated conditions, as shown below.

Table 1.1: Experimental Conditions and Results from Creep Tests

Electrochemical Condition	Load in ~% of Yield Point	Slope of log creep strain rate vs. log time
OCRE	~90% (1500 lbs)	-0.9022
OCRE	~110% (1900 lbs)	-0.9482
Passivated at 100 mV	~90% (1500 lbs)	-1.1597
Passivated at 100 mV	~110% (1900 lbs)	-1.1303
Cathodically charged after crept at 100 mV	~110% (1900 lbs)	-1.3359
Passivated at 400 mV	~90% (1500 lbs)	-1.0419
Passivated at 400 mV	~100% (1700 lbs)	-1.0172
Passivated at 400 mV	~110% (1900 lbs)	-1.0904

The specimen loaded to 90% YS showed a shallower slope than the specimen loaded to 110% YS as shown in Table 1.1. The charge liberated during the creep process under OCRE condition was about 15% higher for the 90% YS loaded specimen than that of the 110% YS loaded specimen. Therefore, the reduction in slope correlates well with an increase in dissolution or increase in the number of vacancies generated. A shallower slope under the OCRE condition as compared to the passivated condition clearly indicates that vacancies generated during the dissolution process slowed down the strain-hardening rate. The vacancies could interact with dislocation pile-ups causing dislocations to climb over obstacles. In this case, as generation of vacancies is a surface process, their diffusion into the bulk of specimen occurs at a much slower rate than that

[19] E. M. Gutman, "Mechanochemistry of Solid Surfaces" World Scientific, Singapore, (1994)

of dislocation trapping. Therefore, almost no effect of dissolution current on creep processes could be observed. However, Revie and Uhlig[11] have observed enhanced creep strain for larger grains and using very thin specimens (0.2 mm diameter) in order to have a high surface area to volume ratio. It should be noted that specimens used in this work had a 0.2 inch diameter (about 1110 grains in the cross section).

Creep under passivated conditions showed slightly steeper slopes than those reported for metals tested in ambient air. It was observed that abrupt loading did not result in a significant increase of the current. This indicates that the height of the slip steps emerging out of the specimen surface during creep processes was not sufficient to rupture the passive film formed prior to loading. Even though the desired load was applied at a relatively fast rate, the measured creep strain rate was of the order of 10^{-4}/s. This strain rate is probably not sufficient to create bare metal surface by film rupture faster than the repassivation rate to cause high oxidation currents. Continuous straining of specimens at faster strain rates (10^{-2}/s or 10^{-3}/s) resulted in increase in corrosion current when the straining continued after yield point[20]. Plotting the corrosion or passivation current in logarithmic scale against logarithmic time showed the effect of stressing the specimen on the passivation kinetics. Under the no-load condition, the specimen passivated at 100 mV showed a slope of -0.58, indicating that the current can be expressed as:

$$i = i_0 \left(\frac{t}{t_0} \right)^{-n} \tag{1.9}$$

where, i = passive current, i_0 = dissolution current of the bare metal at time t_0 , t = time, and n = the repassivation kinetic exponent.

When the specimen was loaded the slope became shallower to a value of n = -0.3. Similar observations were made for the specimens passivated at 400 mV. The reduction in slope indicates slower repassivation kinetics of the material in the stressed condition. After a sufficient length of time, the passivation or corrosion current during creep reached almost a steady state value. Increase in load on the specimen did not affect the passive current if the material was already strain hardened. A similar kind of behavior was observed on the specimens strained at constant strain rates[20]. Mill-annealed specimens showed high peak currents during straining in the plastic region. If the strained specimen was unloaded and reloaded again (in which case, the initial condition becomes strain hardened or cold worked) the observed peak current was much less than that observed for initial mill-annealed material. Repeated loading-unloading-reloading cycles did not alter the peak current significantly, if the material was already strain hardened[20]. Minimum changes in surface dislocation structure are indicated by the negligible change in corrosion current of passivated material in a strain-hardened condition during increased load conditions. When the mill-annealed specimen is stressed, dislocation generation is concentrated near the specimen surface. As corrosion is a surface phenomenon, a maximum peak current was observed in this scenario. Once the material is strained, reloading affects the

[20] K. S. Raja, F. M. Song, D. A. Jones, S. A. Namjoshi and L. G. McMillion , "Correlation of Current Transients to Film Rupture Sites during Tensile Loading of Type 304 SS and Alloy-22 in 4 M NaCl Solution at 60°C" Paper # 03540, Corrosion 2003, NACE.

dislocation structure predominantly in the bulk of the material. Therefore, in the absence of cracks, no significant surface effects can be expected during reloading or an increase in the loading.

As seen in Table 1.1, the specimen passivated at 100 mV showed a much steeper slope than the specimen passivated at 400 mV. Assuming that the thickness of the passive film increases with increasing passivation potential, this could be attributed to the thicker passive films having more misfit dislocations and in turn resulting in easier slip as compared to the thinner passive films. However, continued work is necessary to substantiate this kind of reasoning. It is interesting to note that the slope of log strain rate vs log time plots remained the same in a given passivated condition for all applied loads, even though the specimen was strain hardened by earlier smaller load. In other words, successive loading and prior strain hardening did not affect the dislocation dynamics. This behavior could be an indication that increasing the stress resulted both in generation of mobile dislocations and reactivation of the trapped dislocations. As the initial creep strain rate was almost same for initial mill-annealed condition and the strain hardened (by previous creep) condition, the mobile dislocation density generated during subsequent loading should have been much higher to compensate the decreased dislocation velocity in the strain-hardened material. As the corrosion current was very low, contribution of vacancies in aiding creep strain would be negligible. The steeper slope of log strain rate vs log time plot for passivated specimens clearly indicates that presence of the passive film on the surface acted as an obstacle for dislocation movement.

The specimen crept under 110% YS load in the passivated condition at 100 mV was charged with cathodic current of different magnitude. The application of a cathodic current resulted in an increase in creep strain rate by an order of magnitude. Revie and Uhlig[11] also observed higher creep strain when a copper specimen was cathodically polarized and attributed it to the Rehbinder effect. The role of hydrogen in enhancing the creep strain in the present case cannot be ruled out. Large dislocation pile-ups could be expected as the passive film present prior to cathodic charging acts as an obstacle. Cathodic polarization could cause higher hydrogen concentration at the specimen surface and hydrogen atoms could be transported across the aged passive film. Hydrogen would be easily trapped at the dislocation pile-ups and the flux of hydrogen could result in increased mobile dislocation densities and thus increase the creep strain rate.

When the specimen crept under 110% YS load at 400 mV passive condition was anodically charged with different current densities the creep strain rate increased and reached an almost a steady state of 6.5×10^{-8}/s. The increase in creep rate without increasing the load could be attributed to the effect of vacancy-dislocation interaction. During anodic current charging a very high potential was recorded. Therefore, it is reasonable to assume that all the anodic current was not due to metal dissolution. Concomitant evolution of oxygen also would have significantly contributed to the anodic current. However, a considerable amount of metal dissolution also occurred as the color of the solution changed to bluish green in the cell. A conservative estimate of the metal dissolution during anodic polarization assuming a 1 mA/cm^2 of current (without taking oxygen evolution into account) should result in reduction in diameter of 1.1μm/h.

However, the increase in stress value because of the reduction in cross section by metal dissolution would be about 6% after 75 h of creep. Hence the reduction in gage diameter of the specimen may not contribute significantly to the increased creep rate. Therefore, the observed steady state creep rate could be attributed to the vacancy interaction causing dislocation climb and dislocation glide. Another possible reason for the increased creep rate could be the active surface state of the specimen. During anodic dissolution, it is reasonable assume that the passive film would not be stable. Therefore, surface film would not impede dislocation movement. However, experimental evidence needs to be generated to prove that passive film was not present during impressed anodic current density. Even in the presence of a film, the anodic current density would cause dissolution. In the absence of film, dissolution would create vacancies or divacancies on the surface of the metal and vacancies will not be charged. If the film is present, metal cations in the passive film would dissolve, creating negatively charged vacancies. According to the point defect model[21] these charged cation vacancies would migrate to the metal/film interface due to the field across the passive film and be annihilated. If the rate of arrival of vacancies at the metal/film interface is higher than the rate of annihilation, the vacancies might condense to form a void. However, it is envisaged that dislocation pile-ups would occur at the metal/film interface, which locally increases the internal energy level.. Vacancies reaching the metal/film interface would be attracted to the dislocation pile up sites because of the chemical potential gradient due to the local increase in internal energy. Interaction of vacancies with dislocation pile-up could cause dislocation climb and easy slip.

1.5 Conclusions

From the limited number of constant load experiments carried out on mill-annealed Alloy-22 specimens in 3.9 M NaCl + 0.1 M HCl solution at 80°C under different electrochemical conditions, the following conclusions could be drawn:

- The low temperature creep behavior of Alloy-22 followed a semi-logarithmic relation with time, expressed as $\varepsilon_c = \alpha \ln t + \beta$.
- The logarithmic creep strain rate of Alloy-22 linearly varied with logarithmic time and the slope varied from -0.9 to -1.15 depending on the electrochemical condition.
- In simulated open circuit conditions (OCRE tests), higher corrosion currents did not result in steady-state creep rate. However, the strain-hardening tendency slowed down as the slope of log strain rate vs log time was shallower than that at passivated conditions.
- Creep behavior of the passivated Alloy-22 showed increased strain hardening due to the presence of passive film.
- Dislocation activities were observed to be concentrated near the surface region if the initial condition of the material was mill-annealed. Increasing the stress on the already strain hardened material did not affect the surface conditions significantly.

[21] D. D. Macdonald, J. Electrochem. Society, 139 (1992) 3434

- Imposed anodic current on the passivated specimen increased the creep strain rate by an order of magnitude and a steady state creep rate could be observed. Imposed cathodic current initially increased the creep strain rate and later resulted in logarithmic strain behavior.

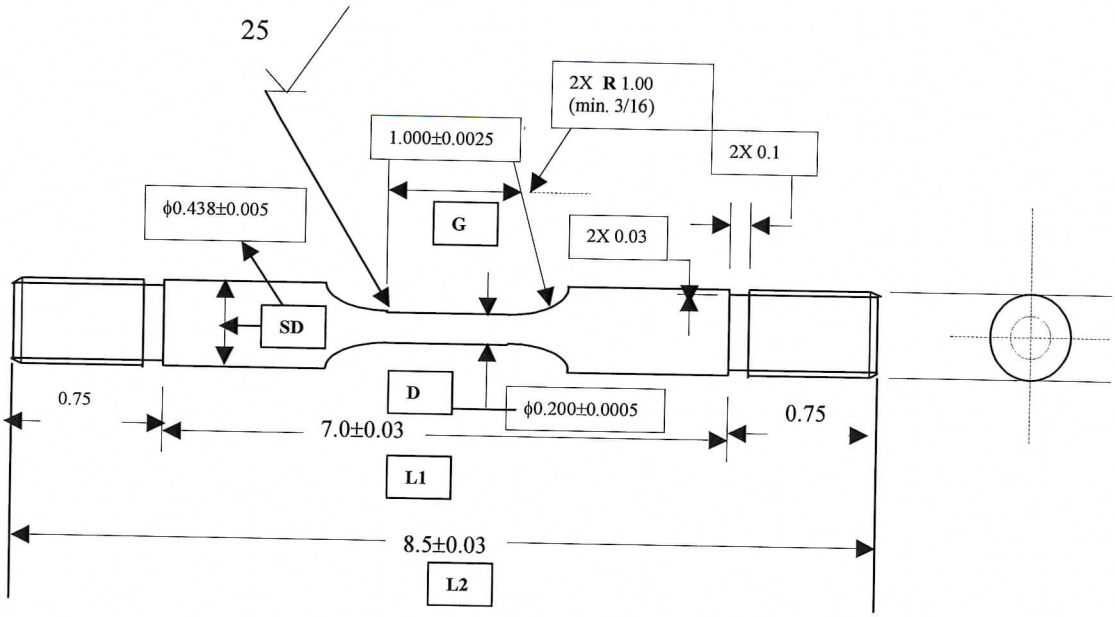

Figure. 1.1 (a) Schematic diagram of tensile specimen used in creep test.

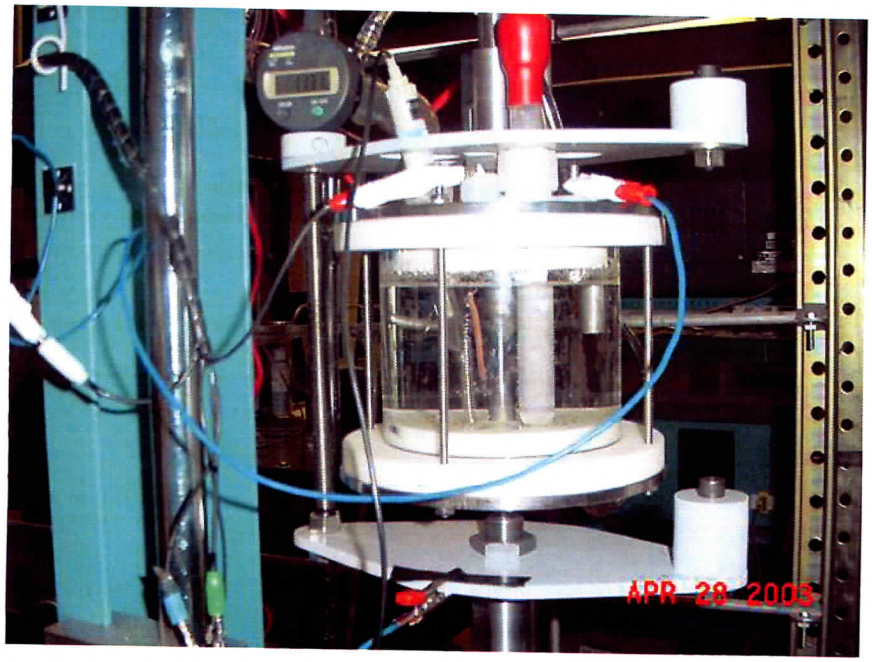

Figure. 1.1 (b) Electrochemical cell-dial indicator assembly for creep experiments

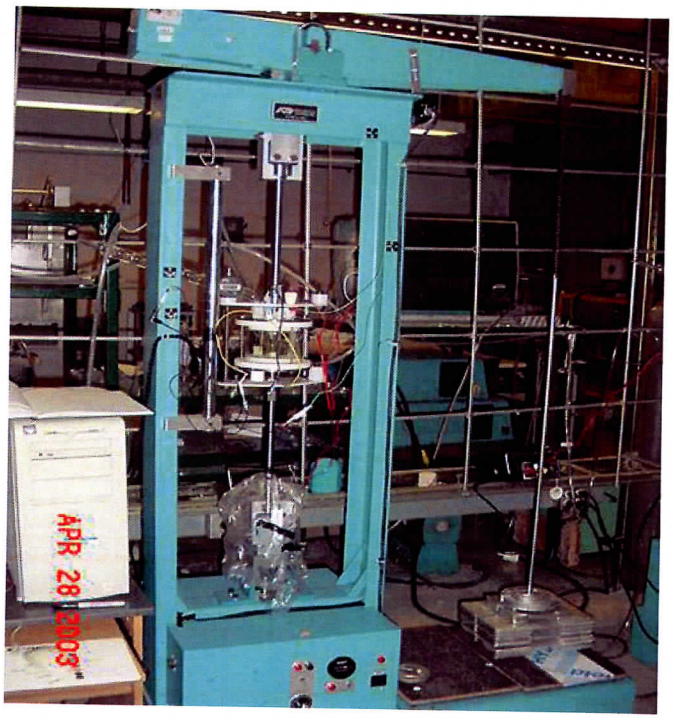

Figure. 1.1(c) Experimental Set-up for Creep Testing.

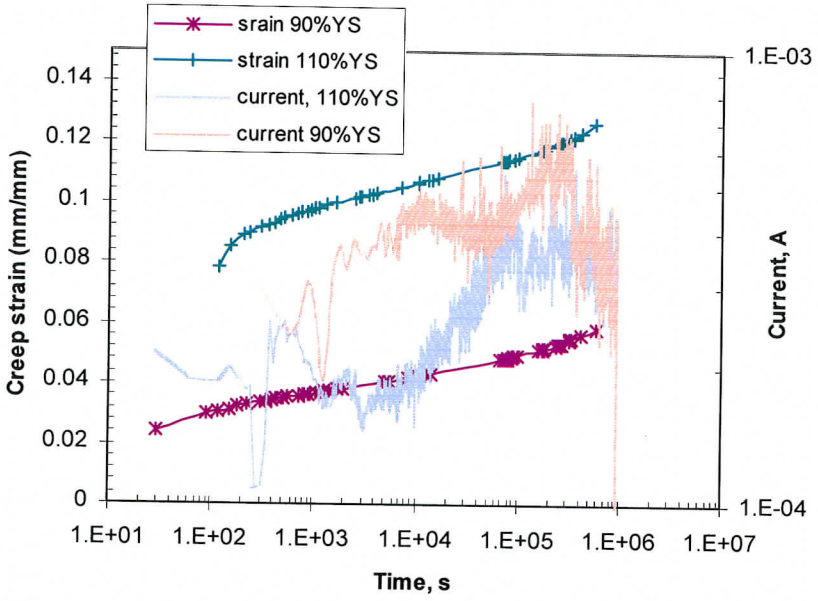

Figure. 1.2: Creep elongation and corrosion current vs. time plots for Alloy-22 in 3.9 M NaCl +0.1 HCl solution at 80°C under constant loads of 90% of and 110% of the yield strength (YS) of the material. The corrosion potential of the stressed specimen followed the open circuit potential of identical unstressed specimen (OCRE).

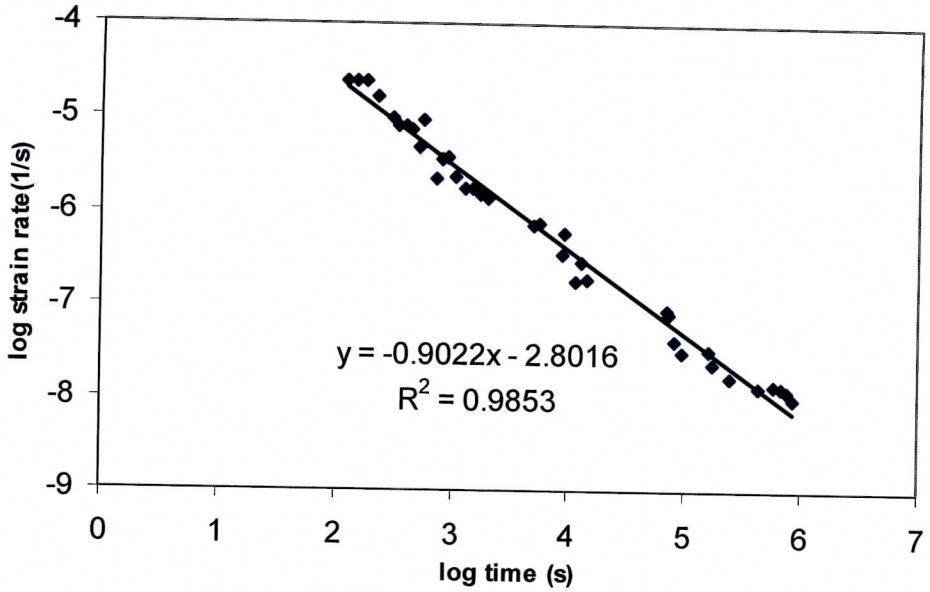

Figure. 1.3: Logarithmic decrease in creep strain rate with logarithmic time during creep of Alloy-22 in 3.9 M NaCl +0.1 M HCl solution at 80°C. The specimen was loaded to 90% of YS (1500 lbs).

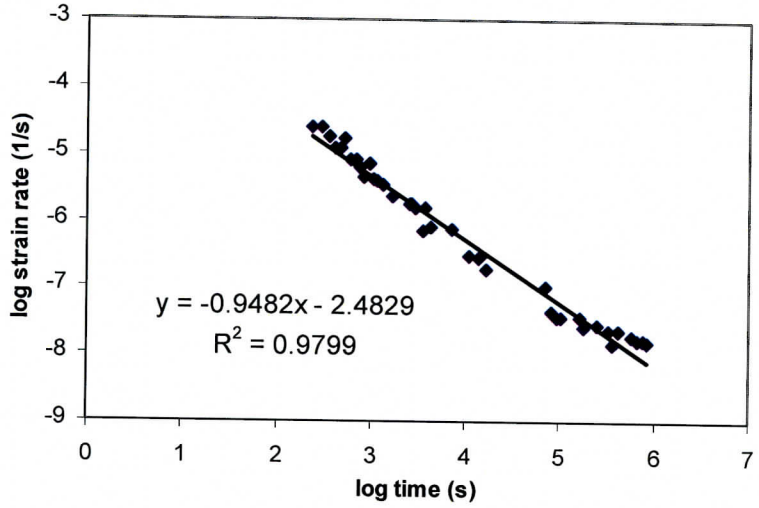

Figure. 1.4: Logarithmic decrease in creep strain rate with logarithmic time during creep of Alloy-22 in 3.9 M NaCl +0.1 M HCl solution at 80°C. The specimen was loaded to 110% of YS (1500 lbs).

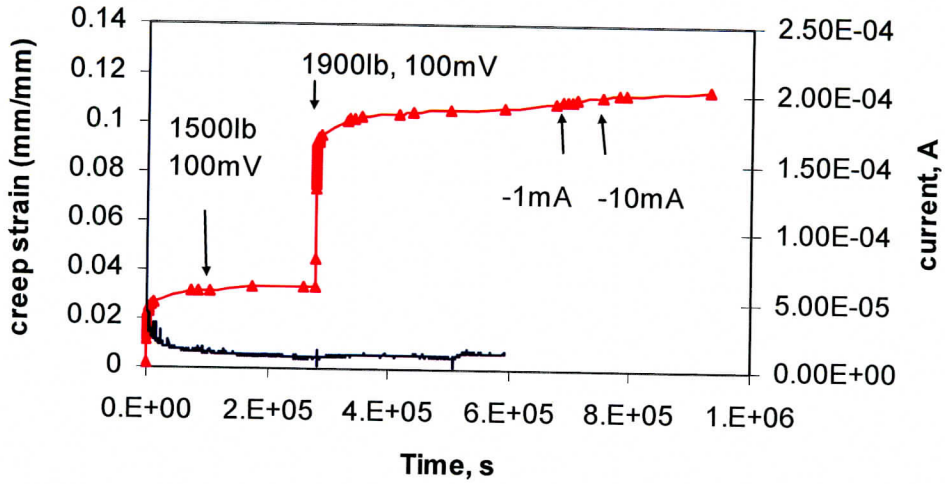

Figure. 1.5: Creep elongation and current transient vs. time of Alloy-22 in 3.9 M NaCl +0.1 M HCl solution at 80 C. Initially the load was 90% of yield strength (YS) (1500 lbs) and increased to 110 % of yield strength (1900 lbs). The specimen was passivated at 100 mV. Finally the specimen was cathodically charged with -1 and -10 mA currents.

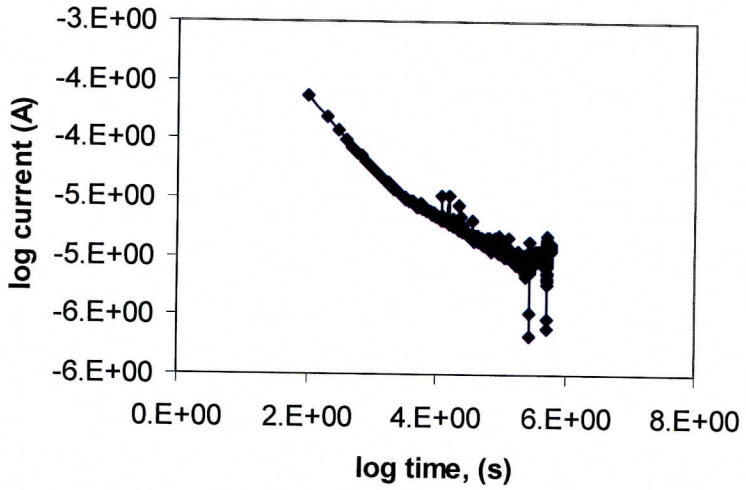

Figure. 1.6: Corrosion (passive) current transient during creep of Alloy-22 passivated at 100 mV plotted in log-log scale. Initial current transient was during no-load condition, with a slope of -0.58. After loading to 90% YS the slope changed to -0.3. Further increase in load to 110% YS did not alter the passivation kinetics.

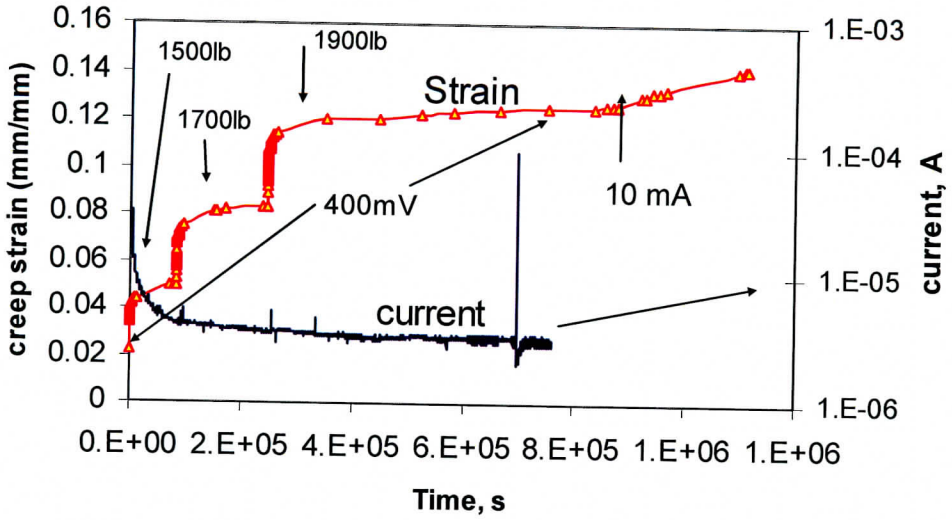

Figure. 1.7: Creep elongation and current transient vs. time of Alloy-22 in 3.9 M NaCl +0.1 M HCl solution at 80 C. The specimen was passivated at 400 mV. Initially the load was 90% of yield strength (YS) (1500 lbs) and subsequently increased to 100% (1700 lbs) and 110% of yield strength (1900 lbs). Finally the specimen was anodically charged with 1 and 10 mA currents. Increase in anodic current caused increase in creep strain and a steady state creep strain rate.

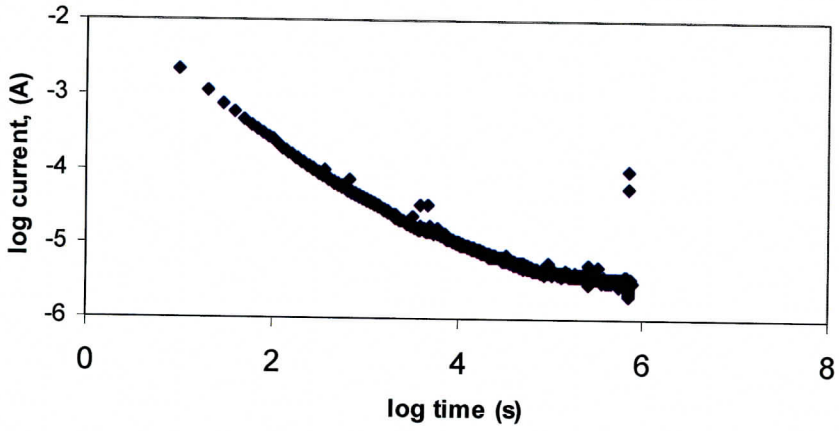

Figure. 1.8: Corrosion (passive) current transient during creep of Alloy-22 passivated at 400 mV plotted in log-log scale. Initial current transient was during no-load condition, with a slope of -0.72. After loading to 90% YS the slope changed to -0.43. Further increase in load to 100% and 110% YS did not alter the passivation kinetics.

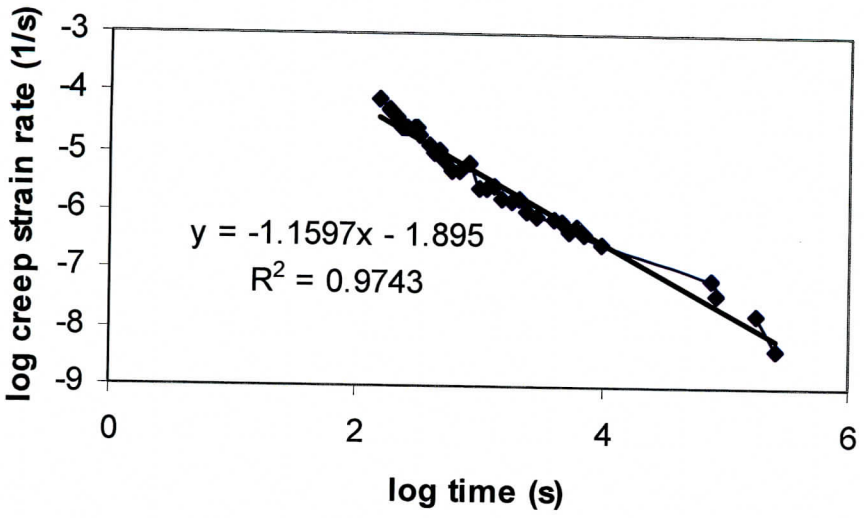

Figure. 1.9: Logarithmic decrease in strain rate with log time for Alloy-22 passivated at 100 mV in 3.9 M NaCl + 0.1 M HCl solution at 80 °C. The specimen was loaded to 90% YS (1500 lbs). The slope of the plot indicates the strain hardening behavior of the material. Presence of a passive film was found to increase the strain hardening of the material.

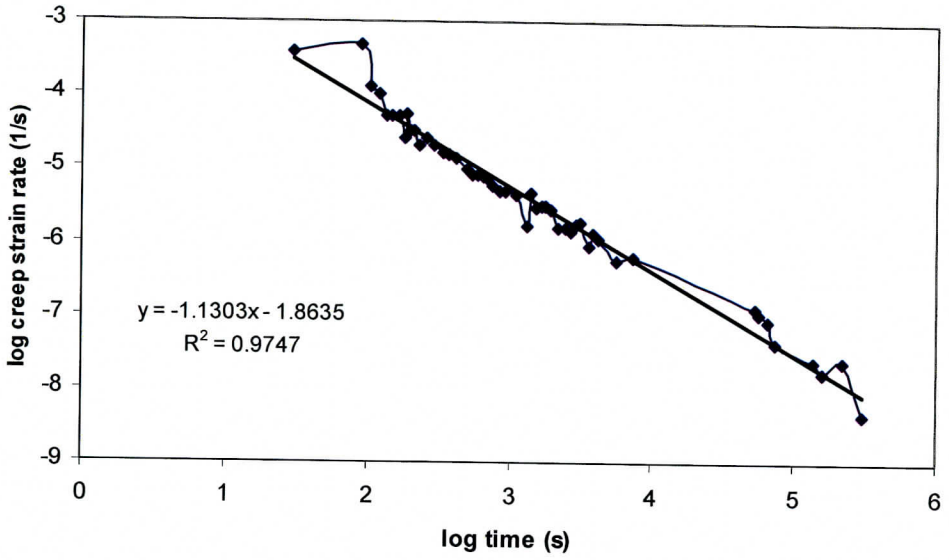

Figure. 1.10: Logarithmic decrease in strain rate with log time for Alloy-22 passivated at 100 mV in 3.9 M NaCl + 0.1 M HCl solution at 80 °C. The load on the specimen was increased to 110% YS (1900 lbs) from 90% YS (1500 lbs). The slope of the plot indicates the strain hardening behavior of the material. Increase in load reactivated the blocked dislocations. Presence of a passive film was found to increase the strain hardening of the material.

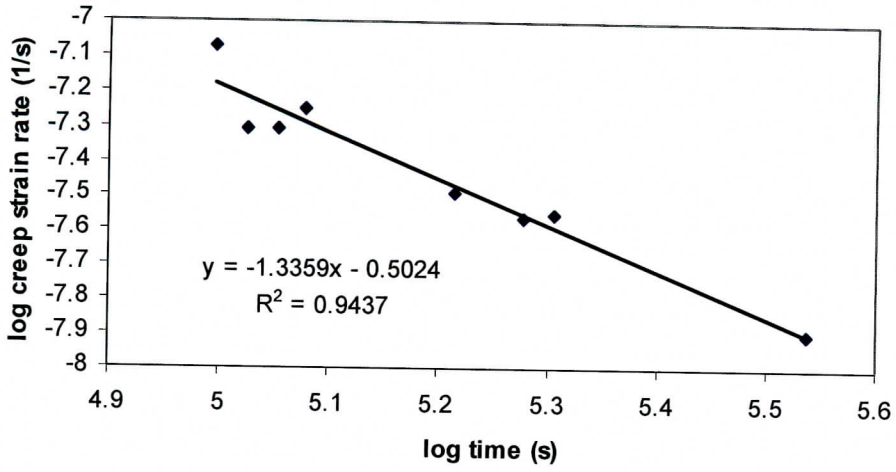

Figure. 1.11: Cathodic charging followed by passivation at 100 mV increased the creep strain rate initially. Continued cathodic charging with increased amount of current did not result in a steady state creep strain rate. Logarithmic decrease in strain rate with time was observed as in the case of increased load condition.

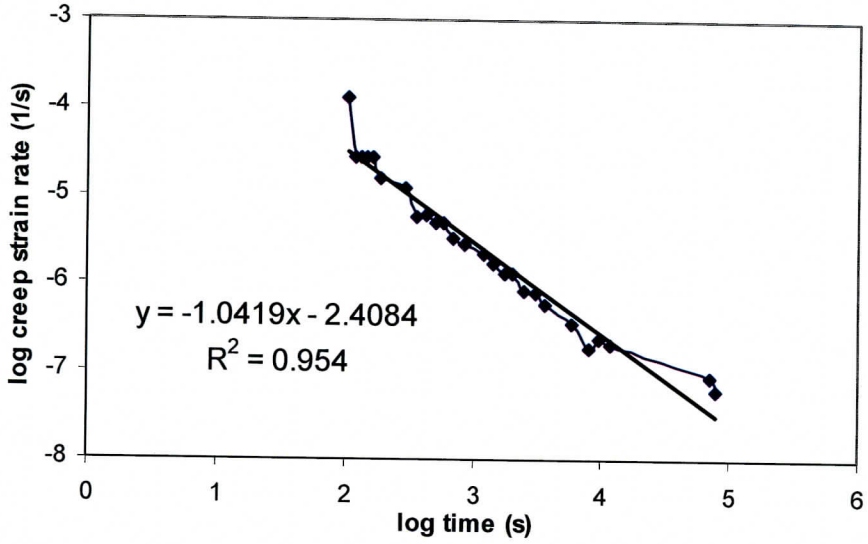

Figure. 1.12: Logarithmic decrease in strain rate with log time for Alloy-22 passivated at 400 mV in 3.9 M NaCl + 0.1 M HCl solution at 80 °C. The specimen was loaded to 90% YS (1500 lbs). The slope of the plot indicates the strain hardening behavior of the material. Presence of a thicker passive film was found to result in relatively less strain hardening as compared to that at 100 mV passivated condition.

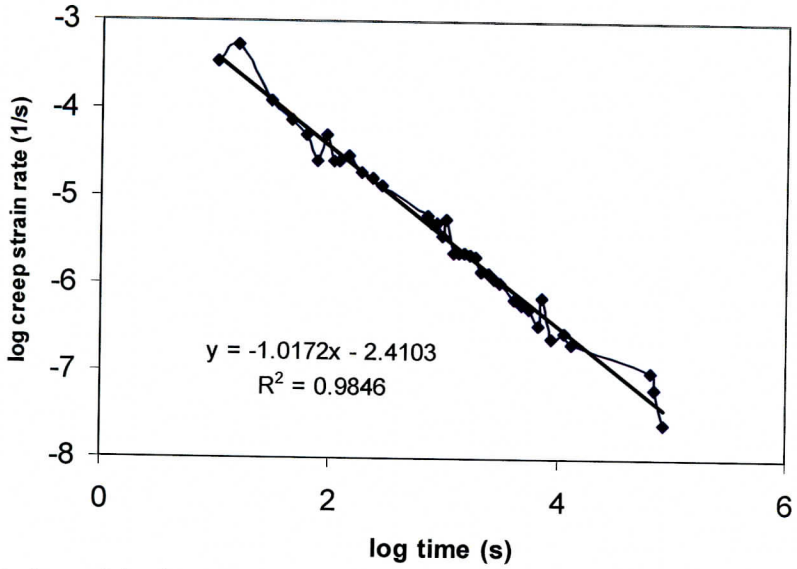

Figure. 1.13: Logarithmic decrease in strain rate with log time for Alloy-22 passivated at 400 mV in 3.9 M NaCl + 0.1 M HCl solution at 80 °C. The load on the specimen was increased to 100% YS (1700 lbs) from 90% YS (1500 lbs). The slope of the plot indicates the strain hardening behavior of the material. Increase in load reactivated the blocked dislocations. The strain hardening behavior was not affected by prior load history.

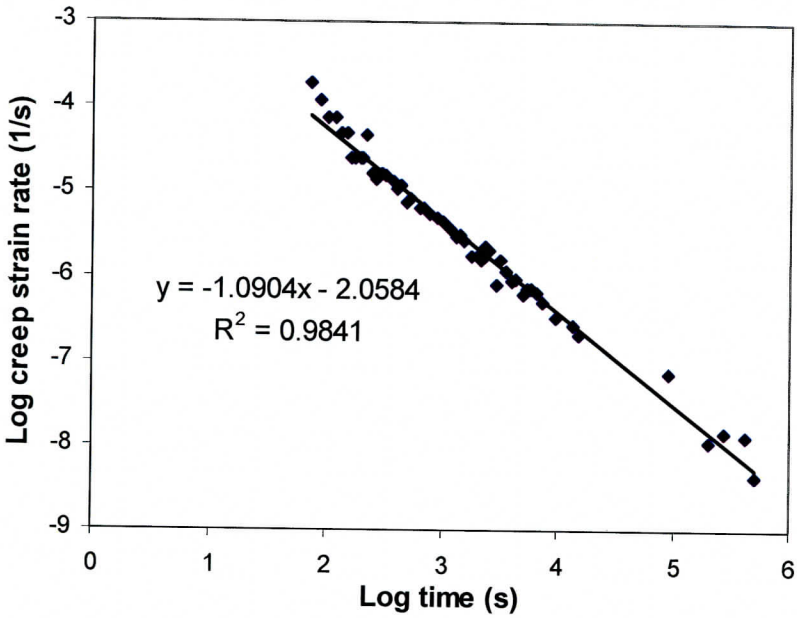

Figure. 1.14: Logarithmic decrease in strain rate with log time for Alloy-22 passivated at 400 mV in 3.9 M NaCl + 0.1 M HCl solution at 80 °C. The load on the specimen was increased to 110% YS (1900 lbs) from 100% YS (1700 lbs). The slope of the plot indicates the strain hardening behavior of the material. Increase in load reactivated the blocked dislocations. The strain hardening behavior was not affected by prior load history.

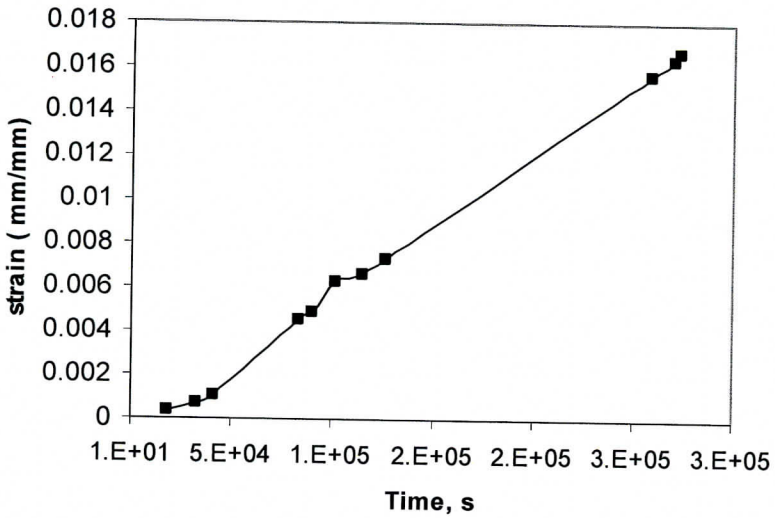

Figure. 1.15: Increase in creep strain and a steady state creep strain rate was observed when the specimen passivated at 400 mV and crept at 1900 lbs was anodically charged with ~1 mA/cm^2 current. The creep rate increased by an order of magnitude from $4.3x10^{-9}/s$ to $6.5x10^{-8}/s$.

Methodology Development/Corroborative Work: 2. SUBTASK 1a - Passive Corrosion Rate Measurements And Passive Film Characterization

2.1 Introduction

This subtask was added to the proposed work as a proof-of-concept demonstration of the newly-conceived Open Circuit Reference Electrode (OCRE) technique as an improvement in Stress Corrosion Cracking testing. In general, Stress Corrosion Cracking (SCC) is reported to occur over a range of electrochemical potentials, at which passivity is observed. In the presence of dissolved oxidizers, the corrosion potential of an ambient environment drifts in the noble direction. Therefore, creep experiments conducted under constant electrochemical potentials may not represent actual environmental conditions. The OCRE technique promises the investigation of the passivation behavior by simulating the enoblement/drifting of potential in the presence of dissolved oxidizers, leading to more realistic results. Unqualified Alloy 22 was used during the method development to conserve the more expensive and limited-quantity qualified Alloy 22 stock. Subtle technical aspects of the OCRE method resulted in more difficulty in method development than was anticipated, thus the time required to develop the OCRE methodology was underestimated by the PI. Because of this, results of this subtask are limited to demonstration of the OCRE as a viable test method. All other aspects of experiments performed during method development were carried out in compliance with the UCCSN QA Program. ***The OCRE technique was subsequently used to generate quality-affecting Alloy 22 data for the Q half of subtask #1b, "Plasticity Enhanced by High Anodic Current Densities at Film Rupture Sites."***

Passive current density, proportional to passive corrosion rate, is often accurately measured by applying a constant potential in the passive potential region using a potentiostat without any dissolved oxidizers in the electrolyte. The continuously recorded decay of passive current at a constant potential in the passive region measures kinetics of the passive film growth with time. For example, Jones and Greene[22] measured passive current decay on 304L stainless steel in deaerated 1-N H_2SO_4. They observed that the passive current density i followed the relation,

$$i = i_o t^n, \tag{2.1}$$

with time t. In log i-log t plots, the slope n was observed to be about –1 for all potentials tested between 100 and 300 mV vs. the saturated calomel electrode (SCE). Similar constant-potential passive current decay kinetics have been reported for iron and nickel base alloys in sodium chloride solutions[23,24,25,26].

Potentiostatic tests presumably simulate open-circuit passivation in the presence of dissolved oxidizers. However, potential is not constant but often increases in the

[22] D. A. Jones and N. D. Greene, Corrosion 22, 198 (1966).
[23] R. Kirchheim, Electrochimica Acta 32, 1619 (1987).
[24] W. Schwenk and A. Rahmel, Electrochimica Acta 5, 181 (1961).
[25] H. S. Kwon, E. A. Cho and K.A.Yeom, Corrosion 56, 33 (2000).
[26] N. Jallert and K. Vu Quang, Corrosion Science, 31, 539 (1989).

noble direction with time during open circuit passivation with dissolved oxidizers[22,27]. It is not known expressly whether passive current is affected by a continuously changing corrosion potential, although it is almost universally assumed that there is no effect. Furthermore, the passive film formed at open-circuit potential with dissolved oxidizers may be inherently different than one formed at a constant or variable potential applied with a potentiostat.

The objectives of the present investigation were to:

1. Design and experimentally verify a method whereby passive current can be measured under a controlled potential, which follows the variable open-circuit corrosion potential of a passive electrode in the presence of a dissolved oxidizer;
2. Compare the passive corrosion rates thus measured using dissolved oxygen, with those measured without dissolved oxygen under constant potential on representative stainless alloys, and
3. Characterize and compare the semiconducting properties of passive films formed by dissolved oxygen and formed by potentiostatic control at comparable passive potentials on the same alloys.

2.2 Experimental Procedures

2.2.1 Electrode and Solution Preparation:

Two alloys were investigated, AISI 304 (UNS S30400) stainless steel (304 SS) and Ni-Cr-Mo-W Alloy-22 (UNS N06022), both received from a commercial supplier as discs, 16 mm diameter and 6 mm thick in the as-received mill-annealed condition. The compositions as supplied by the manufacturer are given below:

	304 SS	Alloy-22
Cr:	19.6	22.3
Ni:	8.2	Balance
Mo:	--	13.1
Fe:	Balance	3.4
W:	--	2.9
Co:	--	0.8
Mn:	1.48	0.29
Si:	0.52	0.06
S:	0.001	<0.01
C:	0.046	0.004
P:	0.023	0.01
V:	--	0.15

Insulated copper wire was soldered to the back of the specimen for electrical connection, using silver-containing solder and acid flux. The melting point of the solder was <200° C; the soldering time was about 3 sec.; and the maximum temperature was 68.5°C as measured by a thermocouple placed 3 mm away from the solder. Thus, we conclude that soldering did not alter microstructure of the specimens or otherwise sensitize them to

[27] D. A. Jones, "Principles and Prevention of Corrosion, p.119, 2nd Ed. Prentice Hall, NY (1996).

intergranular corrosion. Soldered specimens were mounted in epoxy resin, exposing 2 cm^2 of surface area. The insulated lead wire passed through a glass tube, one end sealed in the epoxy mount to shield it from the test solution. The working surfaces of the specimens were polished with a series of emery papers down to 600 grit, cleaned with soap water, and rinsed in distilled water immediately before testing. For comparison with previously published results[22], all tests in this investigation were conducted in 1-N H_2SO_4 solution, prepared with reagent-grade concentrated sulfuric acid added to double-distilled water.

2.2.2 Conventional Polarization Tests:

Potentiodynamic polarization curves were obtained for reference at 24 ± 2°C, following ASTM standard G5 (scan rate 0.6 V/h). A conventional three-electrode system was used in a five-necked 1-liter flask with specimen test electrode and two Pt auxiliary (counter) electrodes (Ingold electrodes, Boston, MA) on opposing sides of the working electrode, for more uniform current distribution. A saturated calomel electrode (SCE) was used as the reference electrode with a solution bridge and Luggin probe. For each test, the solution electrolyte was deaerated for one hour prior to specimen immersion with a pure-nitrogen purge, which continued throughout the test.

Potentiostatic tests were conducted at constant potentials of 0.2 and 0.3 V (SCE). The resulting passive current was recorded continuously at 600-s intervals for 100-150 h.

2.2.3 Open Circuit Reference Electrode:

The open-circuit reference electrode (OCRE) was employed to measure the passive-current density (corrosion rate) during simulated free drift of corrosion potential in the presence of dissolved oxygen. Figure 2.1 shows the experimental set up schematically. The working electrode (WE) and OCRE were identical specimen electrodes, each of 2-cm^2 exposed area, as described above. Two five-necked glass cells were used as described previously, one as working cell containing the WE and a pair or Pt counter electrodes (AUX), and the other the reference cell containing the OCRE. Both were filled with the same test solution, 1-N H_2SO_4, to the same level, and the two were connected electrolytically by a solution bridge and Luggin capillary to the WE. Initially both cells were deaerated for one hour by bubbling pure nitrogen. WE and OCRE were then immersed simultaneously in working and reference cells respectively. The WE was connected to the working electrode terminal in the potentiostat (Gamry, model CM105, included as a hardboard in a conventional PC-compatible computer), and the OCRE was connected to the reference terminal of the potentiostat, replacing the usual reference electrode (REF) in a conventional polarization cell. The REF in Figure 2.1 served only to measure the time-drift potential of the OCRE with the high-impedance voltmeter, V.

The potentiostat was set to maintain constant zero-potential difference between WE and OCRE. Thus, the potentiostat forced the WE to follow the potential drift of the OCRE by supplying any necessary polarizing current. Initially, with both cells

deaerated, the unpolarized difference in corrosion potential between WE and OCRE was near zero, and the potentiostat also supplied zero current with only minor variation.

To begin an experiment, the nitrogen purge was replaced with a pure oxygen purge in the reference cell, while the nitrogen purge continued in the working cell. The increase in dissolved oxygen in the reference cell caused a noble increase in corrosion potential of the OCRE. The WE followed the OCRE into the passive-potential range from its initial active open circuit potential. The necessary anodic current, supplied from the potentiostat and proportional to corrosion rate, was recorded continuously every 600 seconds by the instrument software. Tests were continued for 100 - 150 h. The potential drift of the OCRE was recorded manually from the digital voltmeter, V, with reference to the REF (SCE) in Figure 2.1.

2.2.4 Mott-Schottky Measurements:

Mott-Schottky (M-S) measurements to investigate the electronic properties of the passive film[28,29,30,31,32,33,34] were conducted at the conclusion of passive film growth on the OCRE in open-circuit (oxygenated) conditions and on the WE in potential-control (deoxygenated) conditions. Auxiliary electrodes and a Luggin probe were available in the reference cell (Figure 2.1) to permit M-S measurements on the OCRE but are omitted from Figure 2.1 to avoid confusion in the earlier description of the passive-current measurements. The measurements were initiated first at the final passivation potential, and then as a function of decreasing 100-mV potential steps in the active direction down to -500 mV (SCE), using the CMS 300 electrochemical impedance system (Gamry Instruments Inc.). An ac voltage signal of 10-mV amplitude at 1 kHz was super imposed for 2 seconds at each potential step, and the resultant impedance was measured and recorded as a function of potential. The 1-kHz frequency was selected for comparison with literature data[34]. This series of 2-sec, 100-mV steps required a total measurement time of <20 sec., which is reported to be insufficient to alter the passive-film structure[30,31,32,33,34,35,36,37,38,39]. The interfacial capacitance C was calculated by the system software using the relation, $C = (-Z''2\pi f)^{-1}$, where, Z'' is the imaginary part of the

---

[28] N. Sato, Corrosion 45, 354 (1989).
[29] K. E. Heusler, in Passivity of Metals, R. P. Frankenthal and J. Kruger, Editors, p.772, The Electrochemical Society, Princeton NJ, (1978).
[30] N. E. Hakiki, M. Da Cunha Belo, A. M. P. Simons and M. G. S. Ferreira, J. Electrochem. Soc. 145, 3821 (1998).
[31] N. E. Hakiki, M. F.Montemor, M. G. S. Ferreira and M. da Cunha Belo, Corrosion Science 42, 687 (2000).
[32] M. F.Montemor, M. G. S. Ferreira, N. E. Hakiki and M. da Cunha Belo, Corrosion Science 42, 1635 (2000).
[33] M. Da Cunha Belo, N. E. Hakiki and M. G. S. Ferreira, Electrochimica Acta 44, 2473 (1999).
[34] Agatino Di Paola, Electrochimica Acta 34, 203 (1989).
[35] D. D. Macdonald, K. M. Ismail, and E.Sikora, J.Electrochem. Soc., 145, 3141 (1998).
[36] L. Zhang, D. D. Macdonald, E. Sikora and J. Sikora, J. Electrochem. Soc.,145, 898 (1998).
[37] A.M.P. Simoes, M.G.S. Ferreira, B.Ront and M.da Cunha Belo, J. Electrochem. Soc., 137, 82 (1990).
[38] P. Schmuki and H. Bohni, J. Electrochem. Soc., 139, 1908 (1992).
[39] P. Schmuki, M. Buchler, S. Virtanen, H. Bohni, R. Muller, and L.J.Gauckler, J. Electrochem. Soc., 142, 3336 (1995).

impedance and f is the frequency. C, F/m^2, is related, in turn, to the charge carrier density, N_D , by the following relation[30]:

$$\frac{1}{C^2} = \frac{2}{e\varepsilon\varepsilon_0 N_D}\left[E - E_{FB} - \frac{kT}{e}\right] \qquad (2.2)$$

where

e = elementary electron charge, 1.6021x10^{-19} coulomb (-e for holes)
ε_o= permittivity in vacuum, 8.85 x10^{-12} F/m
ε = dielectric constant, assumed as 15.6 for 304 SS and 12.0 for Alloy-22[34]
N_D = charge carrier density, m^{-3}
E = applied potential, V
E_{FB} = flat band potential, V, k = Boltzman constant, 1.3807x10^{-23} J°K^{-1}and
T = temperature, °K

According to (2.1), the slope of the $1/C^2$ vs. potential plot gives the charge carrier density N_D, from the relation

$$N_D = \frac{2}{e.\varepsilon.\varepsilon_o.m} \qquad (2.3)$$

where m is the slope of the Mott-Schottky plot in the region of interest. A positive slope indicates n-type semiconductivity; and a negative slope p-type[31,32,33,40].

Passive-film thickness, d, was measured with a 3-kHz 10-mV ac impedance signal at the formation , using the relation:

$$d = \frac{\varepsilon\varepsilon_0 A}{C} \qquad (2.4)$$

where, A is the surface area. A higher frequency was selected to minimize the contribution of double layer (Helmholtz) capacitance, which results from charge redistributions within the solution at the surface[34]. Helmholtz capacitance has no affect on the potential vs. $1/C^2$ plot or on the calculation of charge carrier density within the passive film[30,31,32,33,34]. On the other hand, the interfacial capacitance C includes the passive film, is very sensitive to charge carrier density, and provides a reasonable measure of d from equation (2.3).

2.3 Results And Observations

Polarization Behavior

Figure 2.2 confirms the well known excellent corrosion resistance of Alloy-22 compared to 304 SS. For Alloy-22, the corrosion potential is more noble, the primary potential for passivation is more noble, the critical current density for passivation is lower, the anodic Tafel slope is higher, and the passive current density is somewhat lower than for 304 SS. Kinetics of hydrogen reduction in the active (non-passive) state, as measured by the Tafel slope of cathodic polarization curve is relatively faster for 304 SS (-102 mV/decade) than Alloy-22 (-117 mV/decade).

[40] T.-B. Du, British Corrosion Journal, 37, 18 (2002)

Passive current measurements

Figure 2.3 compares the passive currents on 304 SS under constant applied potential of 0.2 V and 0.3 V (SCE) with those produced during continuously changing potentials of the OCRE. The initial current transient for the WE in the OCRE system shows a sizeable current peak, which is associated with the high critical current for passivation for 304 SS, as described in the DISCUSSION section. After completion of passive film formation, the passive current decayed in a manner similar to that during potentiostatic conditions, characteristic of film thickening. Figure 2.4 shows the schematic of the mixed potential theory, which explains the increase in corrosion potential with increase in dissolved oxygen content.

A linear relation between log i vs. log t is apparent in both potentiostatic and OCRE testing. The slopes, n, of the plots are close to –1, as summarized in Table 2.1. Jones and Greene[22] reported similar slopes for Type 304L stainless steel, but their reported current densities were an order of magnitude lower than those presently reported for 304 SS. Such a large difference in current density can be attributed to the lower carbon content of 304L and other possible variations in alloy chemistry of the heats tested. For 304 SS in Figure 2.3, the slopes of passive current decay during potentiostatic and OCRE tests were almost identical. The current decay curves of 0.2 V and 0.3 V were parallel with 0.3 V showing somewhat higher current densities, possibly within the range of experimental reproducibility.

For Alloy-22, the passive current decay curves at 0.2 and 0.3 V were nearly identical, as shown in Figure 2.5. Similar to 304 SS in Figure 2.3, the OCRE currents were higher than the potentiostatic currents during the initial period of film formation. The current peak was much less pronounced for Alloy-22, because of the rather minor active current peak for Alloy-22 shown in Figure 2.2. The slope of the log i vs. log t was around -0.85 for all the test conditions, significantly lower than for 304 SS, as summarized in Table 2.1.

Figure 2.6 compares passive-current decay and corrosion potential increase with time during OCRE tests for 304 SS and Alloy 22. The passive current decay of both alloys followed a linear relation between log i vs. log t, with considerably lower passive-current densities than those of 304 SS. The corrosion potential of OCRE of alloy-22 varied linearly with log time, because the alloy was passive even at –100 mV (SCE), the earliest recorded potential in Figure 2.6. For 304 SS, the corrosion potential of the unpolarized OCRE leveled off to approach a constant value after about 5 to 10 h in both Figures 2.3 and 2.4.

Mott-Schottky Measurements

Figure 2.7 compares the M-S plots of 304 SS passivated under constant potentials of 0.2 V and 0.3 V and two others after identical variable potential transients with and without dissolved oxygen. One variable-potential curve was measured directly from the

OCRE in Figure 2.1, exposed to dissolved oxygen. The other was derived from the WE in Figure 2.1, which was controlled at potentials identical to those of the OCRE but without dissolved oxygen. The four plots are at least qualitatively identical and the same is true for Alloy-22, as shown by the results of analogous experiments in Figure 2.8. Thus, we conclude that passive films on these alloys exhibit the same electronic properties, and probably have the same chemical structure, whether formed by constant or variable potential control in deaerated solutions, or by exposure to dissolved oxygen with variable open-circuit corrosion potential in oxygenated solutions.

As indicated previously, a positive slope of potential vs. $1/C^2$ indicates n-type semiconduction and a negative slope indicates p-type in the passive film[31,32,33]. The passive films formed at constant potentials showed both n-type and p-type behavior for both alloys. However, p-type behavior for Alloy-22 (Figure 2.8) was only slightly evident compared to 304 SS. Slope decreased and thus N_D decreased for both alloys as applied potential decreased below the formation potentials of 0.2 and 0.3 V. Slope becomes independent of prior formation potential as potential decreases. We feel that effects of formation potential are transient and that N_D is generally a direct function of the applied potential and relatively independent of the prior formation potential. Table 2.1 summarizes the charge carrier densities for n-type film behavior of the two alloys. Film electronic properties near the formation potentials are viewed to be more relevant to the objectives of this investigation, and the p-type behavior at more active potentials is not further considered here.

There is a slight but perhaps significant difference between $1/C^2$ values at all the potentials between the WE and OCRE 304 SS specimens, which could be attributed perhaps to minor effects of dissolved oxygen and nitrogen. Little or no similar effects are apparent for Alloy-22. Charge-carrier densities, N_D, in passive films formed on OCRE and WE of both alloys were almost the same, indicating that the passive films formed in aerated and deaerated solutions, respectively, have similar electronic properties.

Table 2.1 summarizes the passive-film thickness formed on 304SS and alloy-22 under different conditions. The passive film on Alloy-22 was thinner than that of 304 SS and the thickness increased with increase in film formation potential. The relation between passivation kinetics, film thickness, and formation potential is discussed in the next section.

2.4 Discussion

Passive-Current Density Measurements

Passive current decay kinetics of passive electrodes in OCRE tests were near the same as those of conventional potentiostatic tests. Thus, the long held assumption has been confirmed that constant-potential tests give a good approximation of passive-film growth in variable potential conditions resulting from passivation by dissolved oxidizers. Almost identical Mott-Schottky behavior of passive films grown with dissolved oxygen or constant potential indicate that the passive film structure and current-conduction

mechanisms are the same for all conditions of potential and dissolved oxygen concentration. Dissolved oxygen apparently provides the necessary potential for passivation with little or no role of oxygen in the passive film provided from the ambient electrolyte solution.

The anodic current-density peak which appeared during the initial 30 minutes, of OCRE testing, (Figure 2.3 for 304 SS, Figure 2.5 for Alloy-22) can be related to the anodic polarization behavior of the alloys[27]. After oxygen was introduced, the dissolved oxygen in the reference cell steadily increased, potential drifted slowly in the noble direction, and anodic current increased on the WE, while potential was in the active region of the anodic polarization curve . Passivation started only when the diffusion limited oxygen reduction current exceeded the critical current density (i_c) for passivation. From the polarization curves of the alloys in Fig. 2.2, it is apparent that the highest OCRE current density coincided with the active current peak for each alloy. Thereafter, the current density decayed above the primary passive potential, E_{pp}, (which was about 50 mV(SCE) for Alloy-22 (Fig. 2.2) and -100 mV(SCE) for 304 SS) when the reduction current exceeded the critical current for passivation. The increase in corrosion potential with film thickening or decrease in passive current could be explained by mixed potential theory.

After the initial current peak, the passive current decay following the relation $i = i_o t^n$ where n was close to -1 for 304 SS and -0.85 for Alloy-22 (Table 2.1). The decay kinetics was nearly identical to those measured potentiostatically at 0.2 and 0.3 V (SCE) in Figure 2.3 and 2.5. No current peak was observed when the test was conducted without initially deoxygenating the reference cell. More noble corrosion potential of the OCRE, above E_{pp} and fully passive from the beginning of the test produced continuous current decay.

The variation of corrosion potential with log time followed a linear relation:

$$E = m_1 \log t + A_1 \quad (2.5)$$

where, E = corrosion potential,
m_1 = slope of potential vs. log time
A_1 = constant.
The slope, m_1, for Alloy-22 was about 97 mV/decade and for 304 SS the slope m_1 in the region of passive potentials was 82-97 mV/decade.

The passive current decay can be expressed from (2.1) as:

$$\log i = \log i_o + n \log t. \quad (2.6)$$

The slope n takes negative value as the current decays with time.

Substituting (2.6) into (2.5) and rearranging yields

$$E = m_1/n \, (\log i) + A_2 \quad (2.7)$$

From (2.7), the Tafel slope for the OCRE tests could be expressed as

$$dE/d(\log i) = m_1/n \quad (2.8)$$

For Alloy-22, the value was calculated to be about -114 mV/decade, which is almost similar to the cathodic Tafel slope (-117 mV/decade) determined from the standard potentiodynamic polarization curve as in Fig. 2.2. Similarly, for 304 SS also the calculated slope -97 mV/decade matches with the potentiodymically determined value of -102 mV/decade.

Passive-film structure

Passive films of stainless steels and nickel base alloys are considered to be highly doped semiconductors[41]. Sato[28] and Heusler[29] have correlated passive-film stability with semiconducting properties of the passive film, especially type of semiconductivity and charge carrier density. Observation of p-type and n-type behavior in Mott-Schottky plots indicates that the passive film of 304 SS is a two-layered structure, as envisaged by Cunha Belo et al.[33] Hakiki et al[30,31] also showed that type 304 and 316 stainless formed a two-layered passive film in which the inner layer was Cr-rich p-type semiconducting oxide and the outer layer was a n-type semiconductor. Whereas, Sato[28] proposed that the inner layer of the passive film could be n-type and the outer layer could be p-type semiconductors. In this present study, M-S plots of 304 SS specimens showed both p-type and n-type behavior whereas, alloy-22 specimens showed only n-type behavior. Similar M-S behavior of Alloy-22 has been reported by Bellanger and Rameau[42]. Dunn et al[43] also proposed that the conducting mechanism of passive film of Ni-Cr-Mo could be transportation of cation interstitials or anion vacancies indicating that the corrosion resistance film is of n-type semiconductor, as the steady-state passive current density was found to be independent of applied potential or pH in their experiments. Based on the M-S results of the 304 SS, it could be proposed that the inner corrosion resistance barrier film of 304 SS in 1 N H_2SO_4 could be of n-type semiconductor and the outer layer could be of p-type semiconductor. The passive film of Alloy-22 is predominantly a n-type semiconductor.

The charge carrier density has been observed to be a strong function of passive film formation potential[33,34]. In OCRE technique, as the WE follows the drift in corrosion potential of OCRE, a semiconducting character sensitive to formation potential is an appropriate parameter for studying the passive films. The charge carrier density of passive-film of both 304SS and Alloy-22 decreased with increase in formation potential (Table 2.1). Similar results were reported for types 304 and 316 stainless steels in borate buffer solution[30] and zinc in 0.1-M sodium borate and 1.0-M sodium hydroxide solution[35]. Di Paola[34] reported a donor concentration of $3.8 \times 10^{21} cm^{-3}$ for type 304 SS passivated in 1-N H_2SO_4 at 200 mV(SCE) which agrees with the present data. However, the donor density reported for passive film of 304 SS formed in borate buffer solution (pH=9.0, and 0.3 V) was $5.6 \times 10^{20} cm^{-3}$, about an order less than the value observed in the present investigation. The difference in charge density could be attributed to the pH of the film-formation solution. Di Paola[34] also observed that the charge carrier density

[41] A. K. Vijh, in "Oxides and Oxide Films" J.W.Diggle, Editor, p.63, Marcel Dekker Inc, NY, (1973).
[42] G. Bellanger and J.J. Rameau, J. Mater. Sc., 31, 2097 (1996)
[43] D. S. Dunn, C. S. Brossia and O. Pensado, Corrosion 2001, Paper No. 01125, Houston, TX, NACE International, (2001).

was lower at near neutral pH and higher at more acidic / basic pH values. This agrees well with the point defect model of Macdonald et al (PDM)[44], which postulates the following reaction at the oxide film/ solution interface as:

$$V_O^{2+} + H_2O \leftrightarrow 2H^+(aq) + O_O \qquad (2.9)$$

where V_O^{2+} is oxygen vacancy and O_O is oxygen atom in the oxide lattice. As the pH decreases the reaction shifts to left hand side of (2.9), creating more oxygen vacancies, which increases the charge carrier density.

The PDM postulates[44,45] that for thicker films (>5 $x10^{-10}$ m), the passive current transients could be expressed by equation (1) with n = -1. For thinner films, the same expression holds with n = -0.5. As the slope of log t vs. log i plot of 304 SS was around -1, it appears that 304 SS has a thicker passive film (> 0.5 nm). Di Paola[34] reported the thickness of passive film of 304 SS in 1 N H_2SO_4 to be 0.79-0.92 nm. In this study the thickness of the passive film of 304 SS is estimated to be about 0.75-0.9 nm depending on the film-formation potential, which satisfies the thick film criterion proposed by Macdonald et al[44,45].

Estimated passive film thickness for Alloy-22 was 0.42- 0.48 nm (Table 2.1), which is a borderline value for thicker film criterion (>0.5 nm) causing the slope of current decay plot to lie between -1 (thicker film) and -0.5 (thinner film). Bellanger and Rameau[42] calculated the thickness of passive film of Alloy-22 formed at 0.3 V (SCE) in pH 3 solution of Na_2SO_4 at 20°C as 0.5 nm by quantifying the total charge consumed during passivation. Absence of significant p-type behavior of passive-film of Alloy-22 supports the view that the film is primarily a thin single-layered structure.

Variations of the open-circuit corrosion potential show little or no effect on the passive-current decay kinetics (Figure 2.3 and 2.5), in agreement with predictions of the point defect model (PDM) of Macdonald[44] . According the PDM[44,45], for n-type semiconductor film, the passive current density is independent of the applied potential because the difference in potential is accommodated by film-thickness variation, thus maintaining a constant electric field across the passive film. The passive current is the result of flux of ions moving across the passive film and is a function of electric field. If the field is constant for a given chemistry of the film, the kinetics of film formation also will be similar in the passive range of potentials, whether the field results from a potentiostat or dissolved oxygen.

2.5 Summary And Conclusions

- The Open Circuit Reference Electrode (OCRE) technique is a potential-control testing method capable of continuously measuring stainless-alloy passive currents in aqueous electrolytes without dissolved oxidizers, while simulating variable open circuit conditions with dissolved oxidizers.

[44] D. D.Macdonald, J. Electrochem. Soc., 139, 3434 (1992)
[45] C. Y. Chao, L. F. Lin and D. D. Macdonald, J. Electrochem. Soc., 128, 1187 (1981).

- The OCRE system was also able to measure initial anodic current transients during solution oxygenation and consequent passivation of stainless alloy surfaces.
- After formation of a stable complete film, the passive anodic current densities, i, and current-decay kinetics were almost identical, following the conventional rate law, $i = i_o t^n$, for both OCRE conditions with dissolved oxygen and potentiostatic conditions in deoxygenated 1-N sulfuric acid. Thus, conventional potentiostatic passive current measurements give a good approximation of passive corrosion rates in the presence of dissolved oxygen, and probably most other dissolved oxidizers, as well.
- A dissolved passivating oxidizer such as dissolved oxygen apparently provides only the necessary potential for passivation and provides no chemical species necessary for passivation.
- A relatively thick (0.70 – 0.94 nm) two-layered passive film was observed on 304 SS in 1-N sulfuric acid, consisting of inner n-type and outer p-type semiconductor layers. A considerably thinner (0.42 – 0.48 nm) n-type passive film was observed on Alloy-22, with only weak evidence of an outer p-type layer.
- Measured values of passive-film thickness, passive-current decay exponent, n, and charge carrier densities are consistent with literature values and with the point-defect model (PDM) of the passive film proposed by Macdonald et al.

Table 2.1. Summary of Passive Film Electronic Properties Formed Under Potentiostatic and OCRE Conditions For 304 SS And Alloy-22 (Corroborative Data - For Information Only)

Measured parameter	Alloy	Potentiostatic control		OCRE control	
		0.2 V	0.3 V	WE	OCRE
Current decay exponent, n	304 SS	-0.96 to -1.01	-0.93 to -1.06	-1.01 to -1.10	N/A
	Alloy- 22	-0.73 to -0.84	-0.82 to -0.87	-0.82 to -0.85	N/A
Charge carrier density, N_D, (cm^{-3})	304 SS	$3.48x10^{21}$	$2.87x10^{21}$	$3.34x10^{21}$	$3.36x10^{21}$
	Alloy-22	$4.14x10^{21}$	$3.46x10^{21}$	$3.64x10^{21}$	$3.22x10^{21}$
Film thickness, d (nm)	304 SS	0.74	0.90	0.75	0.78
	Alloy-22	0.42	0.48	0.44	0.45

Note: Carrier Charge Density and Film Thickness data is from file "**Table 2-2.xls**" in 017KR.009. The Current Decay Exponent is calculated by taking the slope of the log-log plot of current vs. time data available in files, "**Comparison of OCRE&PS data of 304.xls**", and "**Comparison of OCRE&PS data of alloy-22.xls**" in 017KR.004 using the in-built linear regression function in Microsoft Excel 2000.

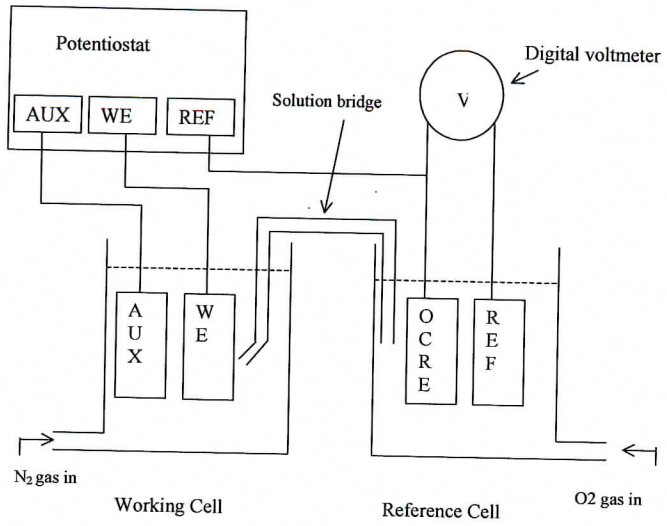

Figure. 2.1: Schematic illustration of the experimental set up for passive current measurement using Open Circuit Reference Electrode (OCRE) technique. (Corroborative Data - For Information Only)

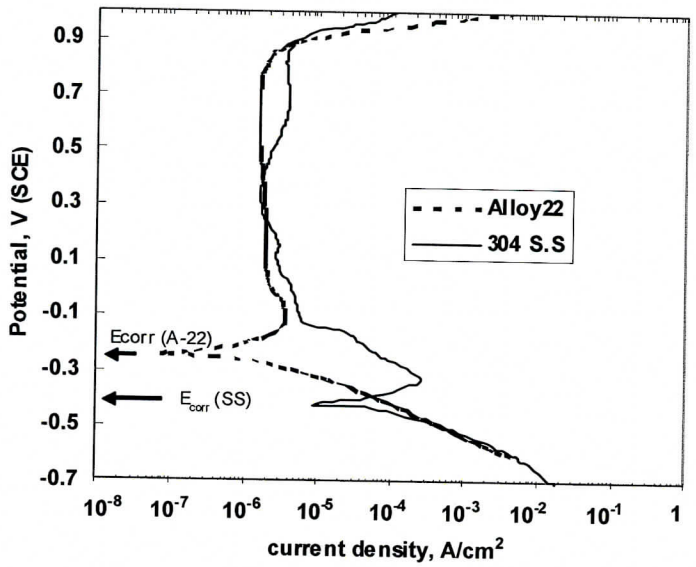

Figure. 2.2: Potentiodynamic polarization curves of type 304 SS and Alloy-22 in 1 N H_2SO_4 at 25° C (Corroborative Data - For Information Only)

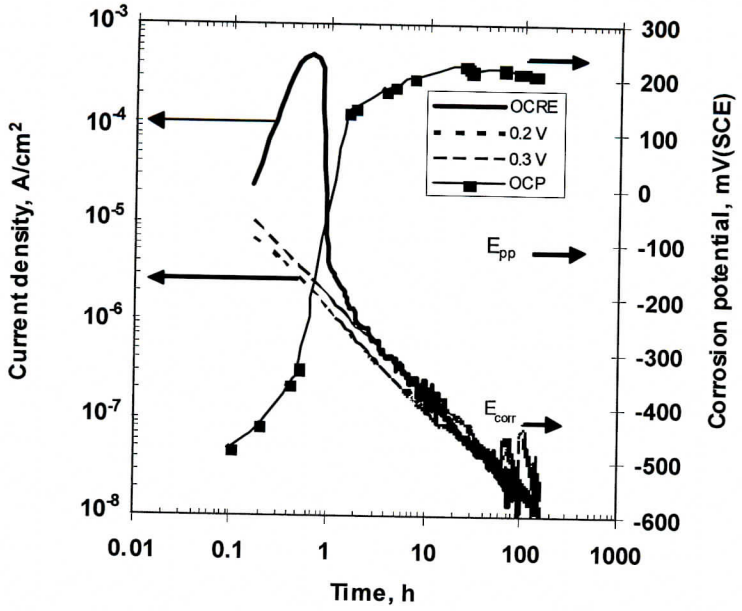

Figure. 2.3: Passive current decay and open circuit corrosion potentials (OCP) of 304 SS in 1 N H_2SO_4 at 25 °C under conventional potentiostatic conditions compared to the OCRE test condition. (Corroborative Data - For Information Only)

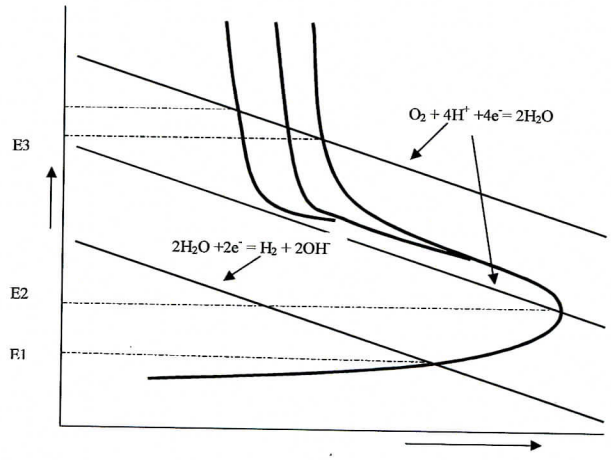

Figure. 2.4: Schematic illustration of increase in corrosion potential with increase in dissolved oxidizers in the solution and with thickening of oxide layer using mixed potential theory. (Corroborative Data - For Information Only)

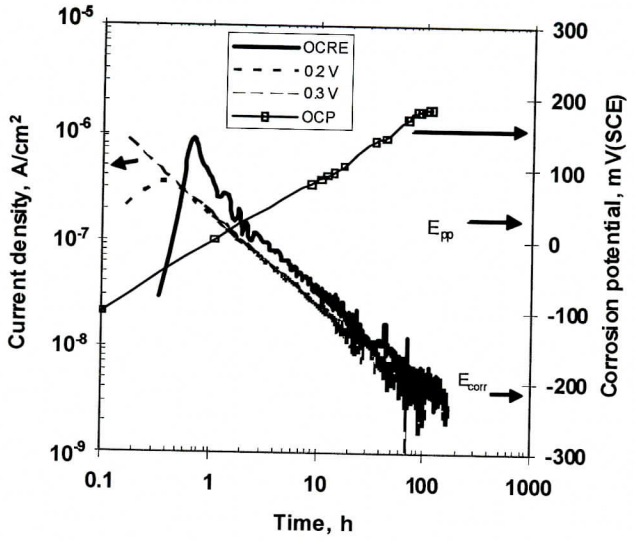

Figure. 2.5: Passive current decay and open circuit corrosion potential (OCP) of Alloy-22 in 1 N H_2SO_4 at 25 °C under conventional potentiostatic conditions compared to OCRE test condition. (Corroborative Data - For Information Only)

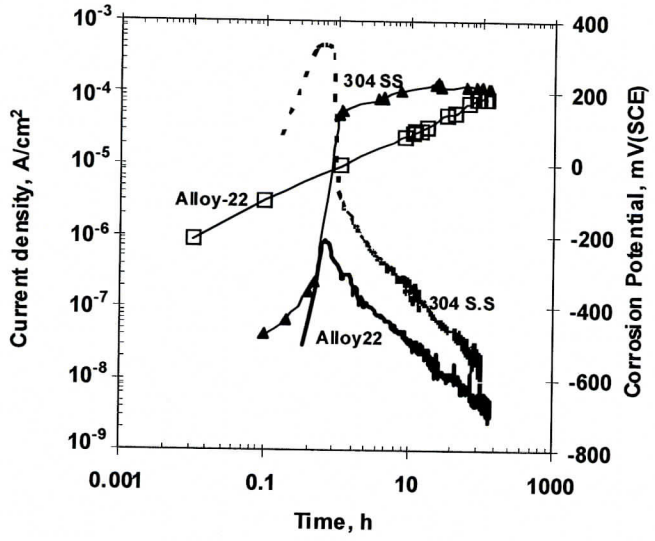

Figure. 2.6: Passive current decay during open circuit reference electrode (OCRE) technique in 1 N H_2SO_4 at 25° C and variation of corrosion potential of the reference cell specimen (oxygen purged) of type 304 SS and Alloy-22. Initially the reference cell was deaerated with nitrogen. (Corroborative Data - For Information Only)

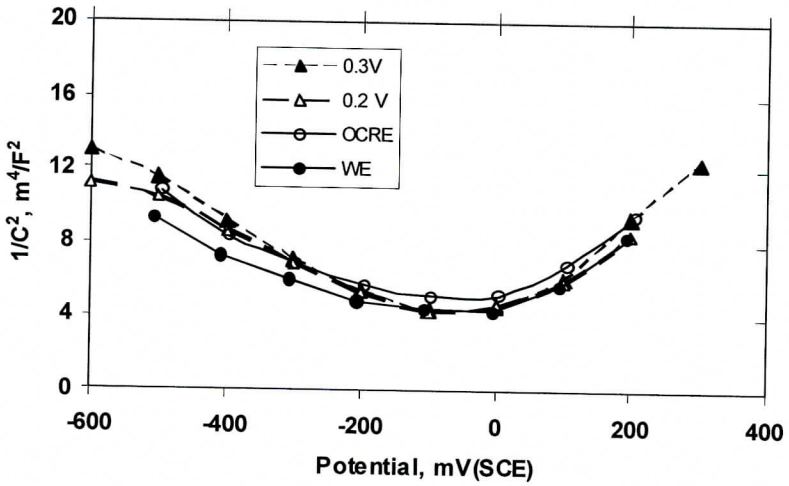

Figure. 2.7: Mott-Schottky plots of 304 SS WE specimens after potentiostatic passivation at 0.2 and 0.3 V (SCE) for 158 h in deoxygenated 1 N H_2SO_4 in comparison with OCRE and WE specimens in 1 N H_2SO_4 after 147 h of OCRE test. (Corroborative Data - For Information Only)

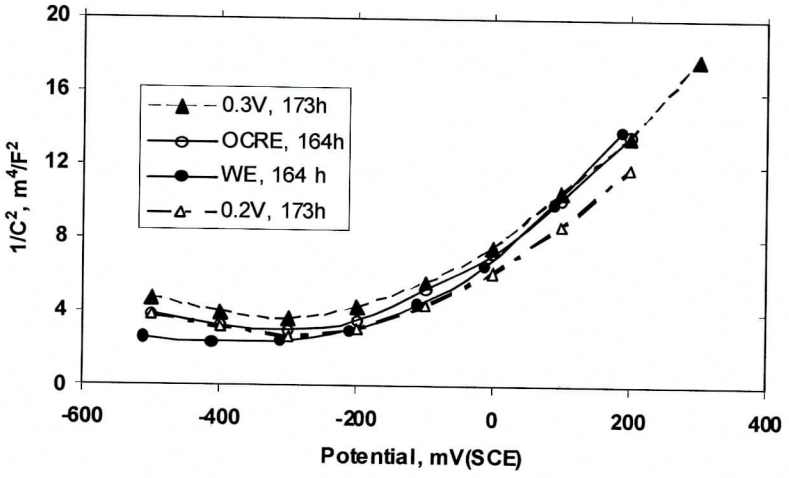

Figure. 2.8: Mott-Schottky plots of Alloy-22 WE specimens after potentiostatic passivation at 0.2 and 0.3 V (SCE) for 173 h in deoxygenated 1 N H_2SO_4 in comparison with OCRE and WE specimens in 1 N H_2SO_4 after 164 h of OCRE test. (Corroborative Data - For Information Only)

Non-Q: 3. SUBTASK 1b - Stress Corrosion Cracking (SCC) Model Development And Verification

CORRELATION OF CURRENT TRANSIENTS TO FILM RUPTURE DURING TENSILE LOADING OF TYPE 304 SS AND ALLOY-22 IN 4 M NaCl SOLUTION AT 60° C

3.1 Introduction

The PI, Dr. Denny Jones, and a post-doctoral associate, Dr. Fengmei Song, worked together on this subtask to develop a new SCC model. Documentation of the model in accordance with Quality Assurance Procedures of the UCCSN QA Program was not completed due to the untimely passing away of Dr. Jones, and to Dr. Song's subsequent move to another research institute. All experiments performed to support the model development were carried out in compliance with the UCCSN QA Program.

Stress corrosion cracking (SCC) of stainless alloys is often related to the kinetics of film rupture and reformation[46,47,48,49]. The crack growth rate during SCC is related to the anodic current density at the crack tip following Faraday's law as[50]:

$$v = iM/zF\rho \tag{3.1}$$

where, v = crack velocity, i = crack tip current density, M = atomic weight, z = mean number of electrons transferred per atom, F = Faraday's constant, 96450 coulomb/g-mole, and ρ = density.

In the above equation, the crack tip current density is related to the dissolution charge density, Q, for one cycle of film rupture and repassivation as[48]:

$$i = Q/t_f \tag{3.2}$$

where, $Q = \int i(t)dt$ (3.3)

t_f = time for one cycle of film breakdown and repair
$i(t) = i_o(t/t_o)^{-n}$ is an expression for the current transient at the crack tip,
i_o = corrosion current of the bare metal
t_o = time at which the bare metal current starts to decay, and
n = exponent of current decay.

---

[46] R. W. Staehle, "Stress Corrosion Cracking and hydrogen Embrittlement of Iron-Base Alloys" (Firminy, 1973), Eds., R.W.Staehle, J. Hochmann, R. D. McCright and J. E. Slater, NACE, Houston, (1977) p.180
[47] I. Maier and J. R. Galvale, Corrosion, 36(1980)60.
[48] D. D. Macdonald and Urquidi-Macdonald, Corrosion Sc., 32(1991)51.
[49] F. P. Ford and P. L. Andresen, Proc. 3rd Int. Sym. Env. Degrad. Mater. Nucl. Power Syst. Water Reactors, The Metallurgical Soc., Warrendale, PA (1988)2789.
[50] J. F. Newman, Corrosion Sc., 21(1981)487

The exponent of current decay, n, basically describes the repassivation kinetics of the metal surface in the given environment.

During SCC of a ductile material, the crack tip undergoes a considerable amount of plastic deformation and strain hardening. The size of the plastic zone near the crack tip is proportional to the square of the ratio of stress intensity at the crack tip to the yield strength of the material[51]. According to the localized surface plasticity model proposed by Jones[52], the anodic current density of the crack tip resulting from anodic dissolution could cause attenuation of the strain hardening, inducing localized surface plasticity. During a film rupture and repassivation cycle of SCC, the crack tip has different material conditions, viz., initially it has the bulk material property, then it strain hardens and further it shows enhanced plasticity at the surface. These changes in material condition could affect the film formation kinetics also. Generally the film formation properties are related to the chemistry of the material. The effect of cold working or strain hardening on the repassivation kinetics has not been documented in the literature for stainless alloys, especially for alloy-22.

The objective of this study is to investigate the effect of strain hardening on the film rupture behavior of stainless alloys such as AISI 304 stainless steel (304SS) and a Ni-Cr-Mo-W alloy, Alloy-22 using smooth tensile specimen and potential controlled straining electrode technique.

3.2 Experimental

The chemical composition in weight %, of 304 SS (UNS S30400) and Alloy-22 (UNS N06022) materials investigated in this study as provided by the manufacturer is as follows:

	304 SS	Alloy-22
Cr:	18.2	21.7
Ni:	8.42	Balance
Mo:	--	13.1
Fe:	Balance	3.5
W:	--	2.8
Co:	--	1.3
Mn:	1.71	0.24
Si:	0.44	0.03
S:	0.026	<0.001
C:	0.04	0.002
P:	0.023	0.01
V:	--	0.15

The materials were tested in the mill-annealed (as-received) condition. Tensile specimens with a gage length of 25.4 mm (1.0 in) and gage diameter of 5.1 mm (0.2 in) were machined out of the as received plate stock. Other dimensions of the specimen are shown

[51] D. P. G. Lisbury, "Embrittlement by the Localized Crack Environment" Ed., R. P. Gangloff, The Metallurgical Soc., Warrendale, PA (1984)149.
[52] D. A. Jones, Corrosion, 52 (1996) 356.

in Fig. 3.1. The shoulders of the specimens were masked with a thin epoxy coating to avoid any crevice type corrosion between the O-ring seal and the metal surface. Gage length portion of the specimen was polished down to 600 grit emery paper and thoroughly washed with alcohol and distilled water before introducing it into the electrochemical cell. The electrochemical test cell had a 150 mm diameter thick walled glass tube secured between two thick PTFE circular sheets using four stainless steel tie rods. Two O-rings provided leak proof seal between the flat ends of the glass tube and the PTFE sheets. Required number of ports were provided in the PTFE lids to accommodate the tensile specimen, counter electrode (2 mm Pt rod), reference electrode (Ag/AgCl), heating element, gas purge, thermocouple, and a condenser. 4 M NaCl solution was prepared using analytical grade chemical and distilled water. The solution was de-aerated by continuously purging an industrial grade nitrogen gas during the experiment. All the tests were carried out at 60°C (140° F). The temperature was controlled within ±1°C using a PID temperature controller. Cyclic polarization studies were carried out to determine the passive range of potentials of the specimens in 4 M NaCl solution at 60°C according to ASTM G61. Polarization was carried out on the tensile specimens exposing the gage length surface and the reducing cross sectional surface. The exposed surface area was roughly estimated to be about 8 cm^2.

Initially the specimen was passivated at -250 mV vs Ag/AgCl for about one hour so that the passive current was around 2-3 μA and did not vary too much with time. This passive potential was selected based on the cyclic polarization results. After reaching a 'steady' passive current, tensile tests were carried out under potentiostatic control by maintaining the potential of -250 mV. The specimens were pulled at different velocities such as 0.00254 mm/s, 0.0254 mm/s and 0.254 mm/s corresponding to initial strain rates of 10^{-4}/s, 10^{-3}/s and 10^{-2}/s respectively. During the first run, the specimen was strained to 20% at a given cross head velocity and the resulting transient current was recorded. After reaching 20% elongation the pulling was stopped; the strain was maintained constant and the current transient was monitored for about 300 s. Then the specimen was unloaded completely and the passivation was continued till it reached a steady passive current value. Again the specimen was strained to 10% (corresponding to initial gage length of 25.4 mm) with the previous cross head velocity and the current transient was recorded during pulling as well as after stopping pulling and maintaining the strain. This procedure was repeated for two more runs. Similar tests were carried out at different cross-head velocities (strain rates). At 10^{-4}/s strain rate, the effect of the magnitude of first run pre-straining on the subsequent runs were investigated by straining to 10, 20, and 30% at the first run and after unloading the subsequent runs were carried out by straining to 10%. The experimental procedure is schematically given in Fig. 3.2. Here, the strain rates and %strain are calculated based on the initial gage length. With the increase in number of loading cycles the gage length of the specimen increased. In all the tests, the change in length was kept as a constant (2.54 mm), correspondingly the actual %strain will be less than 10%. During the straining tests, the current transients were continuously recorded electronically by interfacing the potentiostat with a computer. The recorded current values were subtracted from the base 'steady' state passive current values and reported.

3.3 Results

3.3.1 304 SS

Fig. 3.3 gives the cyclic polarization curves of 304 SS and alloy-22 in 4 M NaCl solution at 60°C. As the surface area was not exactly calculated, only current values are reported in place of current density. The passive potential region of 304 SS was from -500 mV to -200 mV (Ag/AgCl). The pitting prevention potential for 304 SS was around -280 mV. The passive range of alloy-22 was from -400 mV to +200 mV. The passive current was less than that of 304 SS. There was no localized corrosion as the reverse scan traced the anodic scan without crossing the vertical passivation line of Alloy-22. Observation of the polarized specimen under a microscope also confirmed the absence of localized corrosion attack.

Fig. 3.4 (a) illustrates the current transients during straining of 304 SS at a rate of 0.254 mm/s (10^{-2}/s). Fig 3.4 (b) is the corresponding load elongation curves. During run 1, the mill-annealed specimen was strained to 20 % and the current started increasing just before reaching the yield point (about 82% of the yield strength). This increase in current from the steady passive current could be attributed to the film rupture and exposure of bare metal surface to corrosive attack and subsequent repassivation. The current was increasing continuously throughout the straining process and started decaying after the pulling was stopped. Complete unloading and reloading to 10% strain (run 2) did not increase the current as much as in the previous run. The current values of the subsequent unloading and reloading (strain hardening) cycles were almost similar to that of the run 2. The maximum current recorded during second run was about 30% of the current of the first run at 10% strain. The yield stress of the specimen increased with increase in strain hardening cycles. Correspondingly, the load for the initiation of film rupture (when the current started to increase from the steady value) also increased with strain hardening cycles. The estimated film rupture strain of second run was higher than that of the first run. However, the strain for film rupture decreased with subsequent runs.

Fig. 3.5 shows the results of straining the electrode at a rate of 0.0254 mm/s (initially at 10^{-3}/s). The current transients followed the similar trend of 10^{-2}/s strain rate strain hardening cycles. The maximum current observed was much lower than the faster strain rate tests. The estimated film rupture strain also was less than that of faster strain rate tests when compared the corresponding strain hardening cycles between the two strain rates. The maximum current of the first strain hardening cycle at 10^{-3}/s was about four times higher than the subsequent hardening cycles.

Fig. 3.6 shows the current transients during straining at a rate of 0.00254 mm /s (10^{-4}/s). The first straining cycle of 304 SS to 20% elongation recorded a maximum current of 0.175 mA at about 6% elongation and the current decreased with further elongation and reached almost a plateau after 13% elongation. Subsequent cycles of straining to 10% recorded a continuous increase in current. The maximum current values were about one third of the first run. Almost similar behavior was observed for the strain rate of 10^{-3}/s also. However, 10^{-2}/s tests showed only increase in current values throughout the

straining period. The possible reason for this behavior is discussed in the next section. A very little increase in strain to rupture the film was observed for the run 2 as compared to the run 1 of 10^{-4}/s tests. As the flow stress is a function of strain rate, the load at which the plastic flow started and the maximum load after each run increased a little with the increase in strain rate. Changing the final strain of the first run from 20% to 30% and subsequent runs at 10% did not show much difference in current values. Straining to 10% during first run and subsequent three runs also showed almost similar trend of the previous test runs, indicating that amount of strain hardening to more than 10% did not have an effect on subsequent strain hardening cycles. However, there was a clear difference in current transients between the specimen strained from mill-annealed condition and the specimen already strained by more than 10%. The film rupture strain was found to increase with increase in strain rate.

3.3.2 Alloy-22

Fig. 3.7 (a) shows the current transients of the tensile tests carried out at a pulling rate of 0.254 mm/s (10^{-2}/s) on Alloy-22 specimens. Fig. 3.7(b) shows the corresponding load-elongation plots. Straining the specimen from mill-annealed condition to 20% resulted in monotonous increase in current. The current started increasing only after the yield point reached. The recorded maximum current decreased with the increase in strain hardening cycles. It was observed that the current continued to increase for about 2s after stopping the pulling. The repassivation kinetics of the strain hardening surfaces was observed to be similar. The difference between the current values for a given strain between the first run and subsequent runs is smaller as compared to that of 304 SS. The estimated film rupture strain decreased with increase in the number of strain hardening cycles.

Fig. 3.8 shows the current transient results of the tests carried out at a pulling rate of 0.0254 mm/s (10^{-3}/s) on alloy-22 specimens. The current reached a maximum value at 10% of the strain and remained almost constant till 20% of the strain. The current started to increase after reaching the yield point. Subsequent runs also followed the same trend. The current increased continuously throughout the straining period in the subsequent runs. The recorded maximum current of the subsequent runs was about two third of the first run. The estimated film rupture strain increased for the second run as compared to the first run and decreased with further runs.

Fig. 3.9 shows the results of the current transients during straining at a rate of 0.00254 mm/s (10^{-4}/s). The current reached a maximum and started decaying with continued straining till 20%. The maximum current was not clearly recorded because of a leakage problem in the cell. The subsequent runs till 10% strain showed continuous increase in current as observed in other tests.

The recorded current decreased with decrease in strain rate for both 304 SS and alloy-22. Alloy-22 showed much lower current values than that of 304 SS. For 304 SS, film rupture was found to initiate before the incipient of yielding, whereas, alloy-22 showed initiation of film rupture only after yielding, especially during first run of straining. The increase in current from the steady passive current value, which signifies the initiation of

a film rupture event, was observed to be a function of the yield strength of the material and the strain rate.

3.4 Discussion

Straining the 304 SS in mill-annealed condition in the first run for any strain rate resulted in higher current than that of subsequent runs. This behavior could be attributed to the following reasons. In mill-annealed condition, the stacking fault energy of 304 SS is very low[53] and therefore the co-planar slip system is widely separated. When the large slip step emerges out of the surface it creates an additional bare metal surface, by shearing the passive film. When the specimen starts to plastically deform, the current increases dramatically, as the emergence of slip planes shear the passive film and create more and more bare surface area. Simultaneously, the bare metal surface repassivates. However, in this region, the dissolution corrosion current, i_o, is more predominant than the repassivation component. If the strain rate is lower ($< 10^{-2}$/s), the rate of bare surface creation slows down after a certain plastic deformation as the material strain hardens. The dislocation density increases as the material strain hardens. The coplanar slip system becomes finer, making the complete shearing of the passive film difficult. In this region, repassivation current is more predominant than the dissolution current. During the second run, the material was in strain-hardened condition. The slip planes could not be widely separated and because of higher stress requirement new slip systems could be activated. Therefore, emergence of finer slip steps would not create large areas of nascent bare metal surface as the height of the slip step would not be sufficient to shear the film. However, a bare surface could be created due to stretching and rupturing of the film. In this situation, the passive film is assumed to have enough ductility to not be sheared by the fine slip steps. As the rate of bare surface production is slower, the resulting corrosion current also is smaller. More over, during straining large amount of surface steps would be created. These surface steps could result in relatively faster nucleation of surface film during repassivation. So, during subsequent runs, exposure of bare metal to corrosion attack may not be longer, which would result in lower current. However, for complete understanding of the repassivation characteristics, comparison should be made between different strain rates with and without strain hardening.

At higher strain rates the current increased monotonously throughout the straining till 20%. This shows that at higher strain rates, only the most favorably oriented slip planes are active and this results in larger slip steps creating more bare metal surface area. As very little time is allowed for repassivation, most of the recorded current is due to dissolution current. So, the rate of increase of current is higher with higher strain rates.

Keddam and da Silva[54] proposed that the dynamic increase of current could be related to the strain rate as:

---

[53] F. P. Ford, "Embrittlement by the Localized Crack Environment" Ed., R. P. Gangloff, The Metallurgical Soc., Warrendale, PA (1984)117.

[54] M. Keddam and J. Vieira Da Silva, Corrosion Sc., 20(1980)167.

$$I_{max} = C\left(\frac{d\varepsilon}{dt}\right)^{\alpha} \tag{3.4}$$

where, C = a potential independent constant in the passive range of potentials
α = slope of log-log plot of current vs strain rate.

The maximum current values at different strain rates for the first run (starting material in mill-annealed condition) and the average of all maximum current values for the subsequent runs (material in strain-hardened condition) were plotted as shown in Fig 10(a) and (b) respectively. The slope of the strain rate vs maximum current was 0.65 for 304 SS and 0.73 for Alloy-22 in mill-annealed condition. Shibata et al[55] reported a slope of 0.8 for iron in a borate buffer solution. Keddam and da Silva[54] reported the slope of the iron straining electrode in sulfuric acid to be closer to unity.

After strain hardening, the slope of the current vs strain rate plot of 304 SS decreased to 0.5; whereas for alloy-22 the slope, 0.8, was slightly higher than that of the mill-annealed condition. The decrease in the slope of 304 SS after strain hardening indicates that the material is more susceptible to corrosion. The slopes are much shallower compared to the slope of the passive current decay of the materials in passivating environments. Therefore, it is questionable that how well the slope of the present study correlates with the slope of the repassivation kinetics determined by the rapid straining electrode method and scratching electrode method. Recently F. Song et al.[56] proposed a theoretical model to describe the current transients during straining of stainless alloy electrodes at different strain rates. Details about this model are discussed in the next section. In this model, the passive film is considered to be brittle after the rupture strain, and the transient current I_t vs. time t after the specimen yield follows the relation:

$$I_t - I_{t_1} = \gamma\dot{\varepsilon}(t - t_1)^{1-n} / \sqrt{1 + \dot{\varepsilon}t} \tag{3.5}$$

where: $\gamma = \alpha\pi D_0 l_0 / (1-n)$, α is the repassivation kinetic coefficient or $\alpha = i_0 / t_0^{\,n}$, n is the repassivation kinetic exponent, and D_0 and l_0 are respectively the specimen gage diameter and gage length; t_1 is any time after specimen yield point and I_{t1} is the corresponding transient current; $\dot{\varepsilon}$ is strain rate, t is any time after t_1 and I_t is the transient current at t. When t_1 is considered to be the time at which the specimen starts to yield and $t_{t_1} = 0$, Equation (5) can be transformed to:

$$I_t = \gamma\dot{\varepsilon}^{n}(\varepsilon - \varepsilon_y)^{1-n} / \sqrt{1 + \varepsilon} \tag{3.6}$$

where ε is strain at time t and ε_y is the specimen yield strain. When the yield strain ε_y is considered not significantly affected by strain rate, the repassivation current I_t for a given strain, can be related to strain rate by:

$$I_t = k\dot{\varepsilon}^{n} \tag{3.7}$$

---

[55] T. Shibata, T. Takayama and G. Okamoto, USA-Japan Seminar on Passivity and its Breakdown on Iron and Iron-base Alloys, NACE (1976)165.

[56] F.M. Song, K.S. Raja, L.G. McMillion and D.A. Jones, "Development of a Film Rupture and Repassivation Model for Stainless Alloys" TMS Fall Meeting, Oct. 7-10, Columbus OH, (2002).

where: k is a constant related to strain. Equation (3.7), similar to equation (3.4), indicates that the slope of log-log plot of I_t vs. $\dot{\varepsilon}$ must yield the repassivation kinetic exponent "n".

The slope of the maximum current vs strain rate differentiates the mill-annealed material from the strain-hardened material. A steeper slope indicates that the material is more sensitive to the strain rate. Extrapolation of the strain rate vs maximum current plot to very low strain rate simulating the actual SCC test condition such as 10^{-6}/s to 10^{-8}/s would give an estimation of the crack growth rate at the corresponding strain level. Decrease in the slope of this plot indicates higher current at lower strain rates and hence enhanced crack growth rate. For example, extrapolation of the lines in Fig. 3.10(a) and (b) to the strain rate 10^{-7}/s would give the current values of 1.12 μA and 1.62 μA for 304 SS in mill-annealed condition and strain hardened condition respectively. Even though the maximum current values at higher strain rates decreased after strain hardening (in run 2 as compared to run 1), the estimated current was almost 40% higher after strain hardening at 10^{-7}/s. This extrapolation shows that, at lower strain rates strain hardening could increase the current density. In case of alloy-22, the estimated current at 10^{-7}/s was 0.036 μA for mill-annealed condition and 0.011 μA for strain-hardened condition. It appears that prestraining improves the corrosion resistance of alloy-22. Similar observations were by Kamide and Sakazume[57] for nickel base alloy 600 tested in 0.5 M H_2SO_4 + 0.1 M NaCl solution at room temperature. The passive current density was observed to decrease with the increase in prestrain up to 30% during anodic polarization. Initial active dissolution of surface containing high dislocation density followed by formation of more resistant Cr-rich film was attributed to the decreased passivation current[56]. In alloy-22 also, the increase in dislocation density could facilitate easy diffusion of larger atoms like Mo and W to the surface through dislocation channels and movement of divacancies, which could result in improved corrosion resistance.

3.5 Film Rupture and Repassivation (FRRM) Model

The initial step in the mechanism of SCC in aqueous corrosive environments is often considered to be rupture of the passive film by either static or dynamic mechanical tensile strain[58,59,60]. Film rupture is immediately followed by repassivation (new film growth) at the film-rupture sites. The film repassivation rate is a key parameter used in SCC models, and the repassivation kinetics has been broadly studied[59,61,62,63,64,65,66,67].

[57] H. Kamide and T. Sakazume, Corrosion Engineering (Zairyo-To-Kankyo), 50(2001)811.
[58] F.P. FORD, P.L. ANDRESEN, Development and Use of a Predictive Model of Crack Propagation in 304/316L, A533B/A508 and Inconel 600/182 Alloys in 288°C Water, in G.J. Theus, J.R. Weeks (Eds.), Proceedings of the Third International Symposium on Environmental Degradation of Materials in Nuclear Power Systems - Water Reactors, pp.789-800, Traverse City, Michigan (1987).
[59] F.P. FORD, Corrosion, 52, 5, 375 (1996).
[60] D.D. MACDONALD, M. URQUIDI-MACDONALD, Corrosion Science, 32, 1, 51 (1991).
[61] H.S. KWON, E.A. CHO, K.A. YEOM, Corrosion, 56, 1, 32 (2000).
[62] T. MURATA, R.W. STAEHLE, Theory and Application of Straining Electrode, in: G. Okamoto (Ed.), Proceedings of the fifth International Congress on Metallic Corrosion, pp.513-518, Tokyo, Japan, (1972).
[63] X.G. ZHANG, J. VEREECKEN, Corrosion, 45, 1, 57 (1989).
[64] M. KEDDAM, J. VIEIRA DA SILVA, Corrosion Science, 20, 167 (1980).
[65] D.A. JONES, V.S. RAJA, L.G. MCMILLION, K.S. RAJA, Film Rupture and Repassivation on Straining Stainless Steel Electrodes, Proceedings of Corrosion/2002, Paper 02421, NACE, Colorado (2002).

The most common measurements of repassivation kinetics utilize rapid-pulse loading or scratching of a passive electrode[61,62]. The resultant mechanical strain (due to the rapid-pulse loading) generates film-ruptured surfaces, where under a controlled potential, the total anodic metal oxidation current generated at the ruptured sites can be recorded with time. Measurement of the resulting current spikes requires sophisticated instrumentation to record often very high currents within milliseconds or less, with a necessity to compensate for large IR-drop errors. It is not obvious that the rapid straining and the large stresses thus created at the film ruptured sites are relevant to the slow strain rates required for SCC. Therefore, an alternative model has been developed to calculate the repassivation kinetics from experimental conditions closer to those of actual SCC.

Slow Electrode Straining Test (SEST) is a technique similar to slow strain rate testing (SSRT) but having higher strain rates. This technique has been successfully utilized by many others for studying SCC or film repassivation kinetics[63,64,65,66,67]. When a tensile specimen is loaded in tension under potentiostatic conditions, as the passive film ruptures, an anodic current generated at the film ruptured sites will flow through the solution to the counter electrode. This current can then be recorded accurately with controlled straining time.

Since the transient current reflects film repassivation kinetics, a quantitative description of the transient current vs. time may permit the determination of parameters related to the repassivation kinetics. The subsequent sections discuss a mathematical model, newly developed to quantify these parameters. The values of the parameters thus obtained can then be compared to those widely documented using different techniques[59,61]. A higher strain rate in the study of repassivation kinetics may be used e.g. 0.01 /s to minimize metal dissolution into solution, useful for more accurate attainment of repassivation kinetics[65].

3.5.1 A New Film Rupture And Repassivation Model

Since film rupture of the specimen occurs as multiple events for a tensile specimen and the current at a ruptured site is related to the repassivation history of the site, the transient current vs. time relation is complex. A new film rupture and repassivation model (FRRM) is developed for SEST (Slow Electrode Straining Test) to correlate the transient current vs. time with the aim of attaining values of the parameters related to the film repassivation kinetics.

The film repassivation kinetics at a film-ruptured site are given as[58]:

$$i_a = \alpha t^{-n} \tag{3.8}$$

where: i_a is film repassivation current density at the film rupture site, α is a constant related to material properties and solution conductivity, t is time, and n (>0) is the repassivation kinetic exponent. "n" is the parameter to be determined using the new FRRM.

---

[66] D.A. JONES, C.D. KIM, B.E. WILDE, Corrosion, 33, 50 (1977).
[67] T.P. HOAR, J.C. SCULLY, J. Electrochem. Soc., 111, 348 (1964).

The following assumptions were made for development of the FRRM:

- the original passive film and the new repassivating film at the film-ruptured sites, each is fully brittle,
- the contribution of metal dissolution (into solution) to the transient current at the film-ruptured sites is insignificant compared to that of repassivation due to higher strain rates, and
- the distribution of the film-ruptured sites and the change of the passive film thickness due to mechanical elongation are all ignored.

The purpose of the new FRRM is to understand the relationship between the total repassivation current (I_t) and time (t) and to utilize this relationship to obtain the repassivation kinetic exponent "n".

Typically, for SEST (Slow Electrode Straining Test) the specimen gauge length varies with elongation time and follows the relationship given by:

$$l_\theta = l_0(1 + \dot{\varepsilon}\theta) \tag{3.9}$$

where l_θ is the gauge length at an instant time θ, l_0 is the original gauge length prior to any elongation (t=0), $\dot{\varepsilon}$ is strain rate. θ is in this work distinguished from time t and refers to any time between 0 and t, or $0 \le \theta \le t$.

At time θ, the cross-sectional diameter (D_θ) is

$$D_\theta / D_0 = \sqrt{1/(1+\dot{\varepsilon}\theta)} \tag{3.10}$$

where D_0 is the original gauge diameter prior to elongation (t=0) and a constant gauge volume with elongation is assumed for both elastic deformation and plastic deformation. Note the constant volume assumption for elastic deformation, which has no effect on the modeling results since only in the plastic deformation region the model is used to obtain the repassivation kinetics. Plenty experimental evidence[63,64,65] has showed that only near the plastic region a measurable transient current resulting from film rupture can be obtained useful for the attainment of repassivation kinetics.

Consider a tensile specimen being strained at a given strain rate, $\dot{\varepsilon}$, and dl_θ is the length increment of the specimen gauge during a time interval $d\theta$ between θ and $\theta+d\theta$. When the passive film (original and repassivated) ruptures, dl_θ equals the accumulated length of those film-ruptured sites created within the same time interval and it does not vary with elongation; further elongation of the specimen breaks this new film and creates new fresh surface which contributes to a newer accumulated length change. Figure 3.11 schematically shows the variation of the gauge geometrical parameters with elongation at four different times:

- at the original gauge length before elongation (t=0, $D=D_0$, $l=l_0$),

- at the yield point ($t=t_y$, $D=D_y$, $l=l_y$),
- at any time θ after yield ($t=\theta$, $D=D_\theta$, $l=l_\theta$), and finally
- at a time t ($\geq\theta$) after the time in step 3, ($t=t$ ($\geq\theta$), $D=D_t$, $l=l_t$).

Figure 3.11 indicates that $0<t_y\leq\theta\leq t$. From this point onward, θ is exclusively referred to instant time in the plastic region ($\theta\geq t_y$). In Figure 3.11, the original passive film and the repassivating film at the film ruptured sites are distinguished using solid and gray broken lines respectively. It is assumed that up to the yield point ($t=t_y$), the passive film elongates but stays unbroken or at least no significant portion of the passive film is broken. Figure 3.11 shows that at t=t,

$$dl_{\theta t} = dl_\theta = dl_t = l_0\dot{\varepsilon}d\theta \tag{3.11}$$

where $dl_{\theta t}$ is the value at time "t" of the elongation (dl_θ) created between θ and $\theta+d\theta$ where $t\geq\theta$. As mentioned earlier, dl_θ does not change with time and equals its value at time t ($dl_{\theta t}$), or $dl_\theta=dl_{\theta t}$. dl_t refers to film ruptured length created at the time interval between t and t+dt, and for a constant strain rate and a brittle passive film, is equal to dl_θ ($dl_t=dl_\theta$).

Since the specimen shrinks in diameter with elongation ($D_\theta\geq D_{\theta t}=D_t$), the total film-ruptured surface area created between θ and $\theta+d\theta$ ($dS_\theta=\pi D_\theta dl_\theta$) becomes, at a later time t,

$$dS_{\theta t} = \pi D_t dl_{\theta t} = \pi D_0 l_0\dot{\varepsilon}d\theta/\sqrt{1+\dot{\varepsilon}t} \tag{3.12}$$

Equation (3.12) has taken into account the conversion of dS_θ to $dS_{\theta t}$, and indicates $dS_{\theta t}=dS_t\leq dS_\theta$ (Figure 3.11). Note dS_θ decreases with time as the gauge diameter decreases with time. dl_θ does not change with time ($dl_\theta=dl_{\theta t}$). For constant strain rate, $dl_\theta=dl_t$.

Since the repassivation current density at a film-ruptured site is related to the history of the site, for a film ruptured site created at a time θ, the repassivation current density at a later time t becomes[58,59,60,63]:

$$i_{a(\theta t)} = \alpha(t-\theta)^{-n} \tag{3.13}$$

The total repassivation current I_t vs. time of elongation t therefore is

$$I_t = \int i_{a(\theta t)}dS_{\theta t} = \gamma_1\int(t-\theta)^{-n}d\theta/\sqrt{1+\dot{\varepsilon}t} \tag{3.14}$$

where $\gamma_1=\alpha\pi D_0 l_0\dot{\varepsilon}$. The integration limit of Equation (3.14) is from any time after the yield point t_1 ($t_1\geq t_y$) to t-δ, which is taken as the upper integration limit because Equation

(3.8) is valid only after a small time δ from starting repassivation at a film ruptured site[59,63].

The integration results of Equation (3.14) from t_1 to t-δ yields, for n=1,

$$I_t - I_{t_1} = \gamma_1 \ln[(t-t_1)/\delta]/\sqrt{1+\dot{\varepsilon}t} \tag{3.15}$$

For n≠1,

$$I_t - I_{t_1} = \gamma_2[(t-t_1)^{1-n} - \delta^{1-n}]/\sqrt{1+\dot{\varepsilon}t} \tag{3.16}$$

where $\gamma_2 = \gamma_1/(1-n)$.

When straining of the specimen is stopped at a time t_c ($t_c \geq t_1 \geq t_y$, and $\dot{\varepsilon}=0$), when a constant strain is maintained, the specimen gauge diameter, length and surface area each keeps constant regardless of time. For any time after t_c ($t \geq t_c$), $dS_{\theta t} = \pi D_0 l_0 \dot{\varepsilon} d\theta/\sqrt{1+\dot{\varepsilon}t_c}$ which $dS_{\theta t}$ does not change with continuing time, and the repassivation current varies with time t based on Equation (3.14) following

$$I_t = \gamma_1 \int (t-\theta)^{-n} d\theta/\sqrt{1+\dot{\varepsilon}t_c} \tag{3.17}$$

The integration limit of Equation (3.17) ranges from t_1 to t_c-δ, and the integration results are, for n=1,

$$I_t - I_{t_1} = \gamma_1 \ln[(t-t_1)/(t-t_c+\delta)]/\sqrt{1+\dot{\varepsilon}t_c} \tag{3.18}$$

For n≠1,

$$I_t - I_{t_1} = \gamma_2[(t-t_1)^{1-n} - (t-t_c+\delta)^{1-n}]/\sqrt{1+\dot{\varepsilon}t_c} \tag{3.19}$$

3.6 Conclusions

- During straining, the maximum current value as a result of film breakdown and repassivation, increased with increase in strain rate for both 304 SS and alloy-22. Straining in mill-annealed condition showed larger increase in current compared to the strain hardened material.
- Initiation of film rupture occurred before reaching the yield point in case of 304 SS and after yield point in case of alloy-22.
- A linear relation was observed in log-log scale between the strain rate and the maximum current value during straining. The slope of this plot can be compared to the exponent of passive current decay.

- The slope of maximum current vs strain rate for 304 SS in mill-annealed condition was 0.65 and with strain hardening it decreased to 0.5. This decrease in slope indicates more susceptibility of the material to corrosion.
- The slope of the maximum current vs strain rate for alloy-22 in mill-annealed condition was 0.73 and with strain hardening it increased to 0.8.
- A preliminary FRRM model has been developed and may be used for calculating the film rupture and repassivation kinetics during SCC. Assuming brittle passive film, this new model allows a theoretical determination of the film-repassivation kinetic exponent "n". Factors like: (1) the intermediate ductility of the passive films, (2) metal dissolution at the film-ruptured sites, and (3) the effect of environment and material properties on the repassivation, can be incorporated into the model, as part of future work, to improve it.

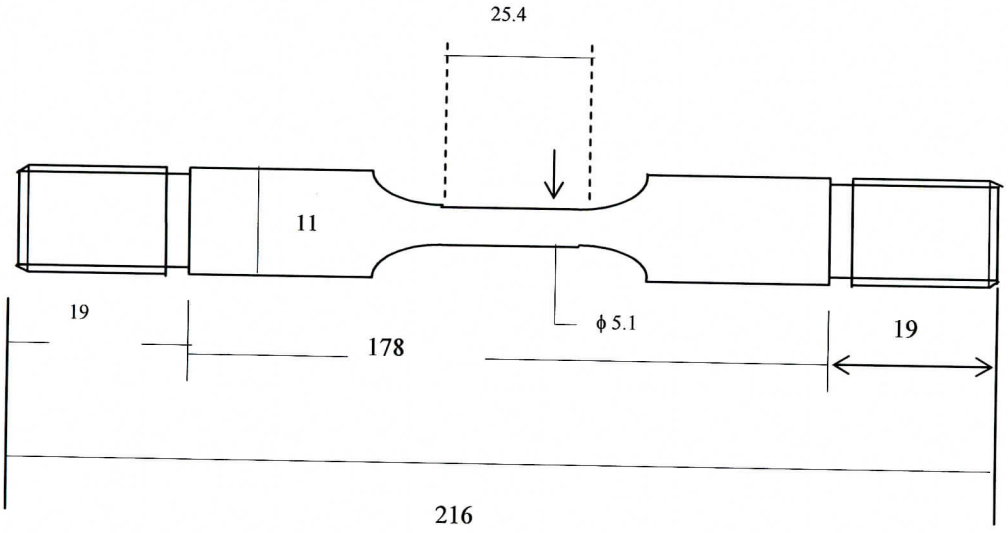

Figure 3.1: Diagram of the cylindrical tensile specimen. All dimensions are in mm. (Non-Q: For Information Only)

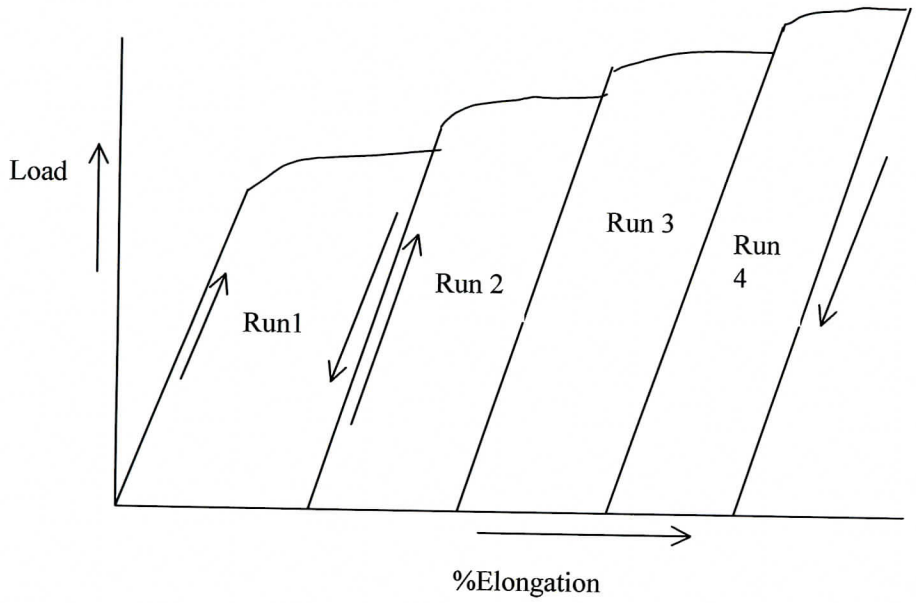

Figure 3.2 Schematic of the tensile test runs to investigate the strain hardening effect on current transients of 304 SS and alloy-22 in 4 M NaCl solution at 60°C. (Non-Q: For Information Only)

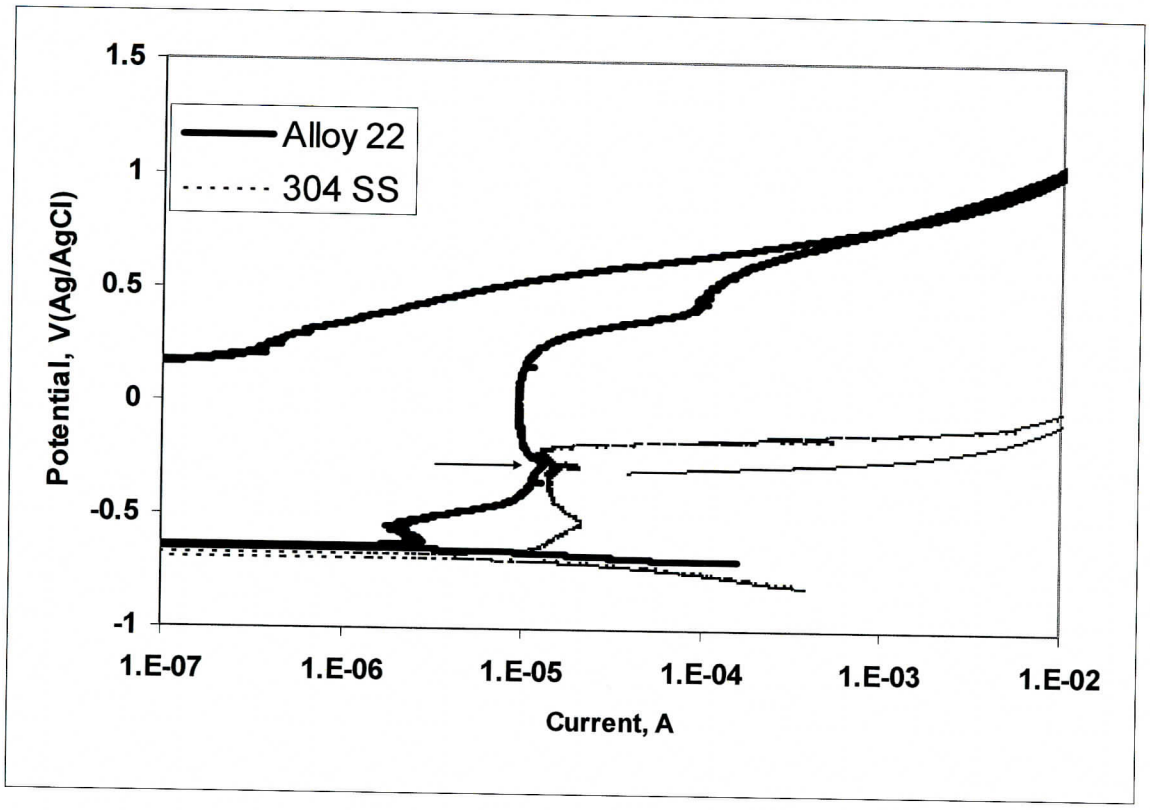

Figure 3.3: Cyclic polarization of 304 SS and Alloy-22 in 4 M NaCl solution at 60°C. (Non-Q: For Information Only)

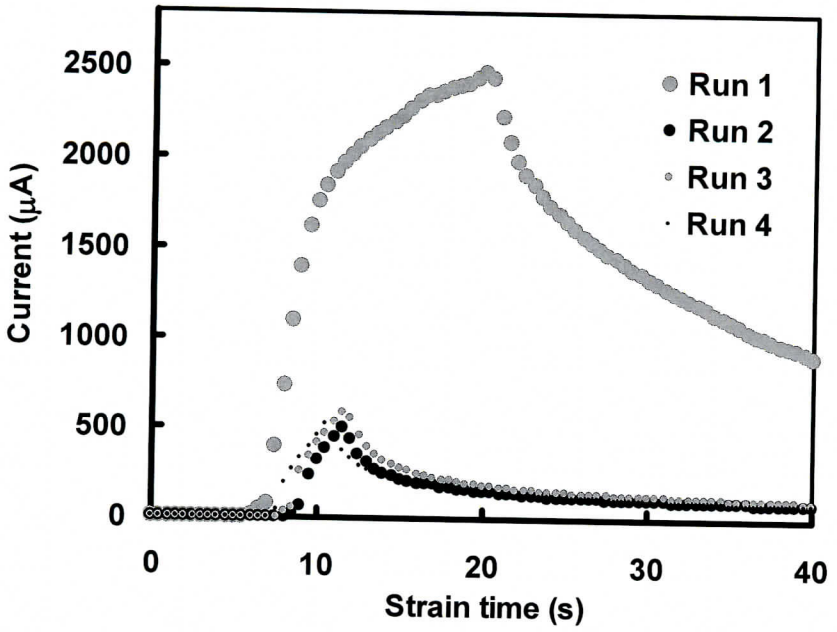

(a)

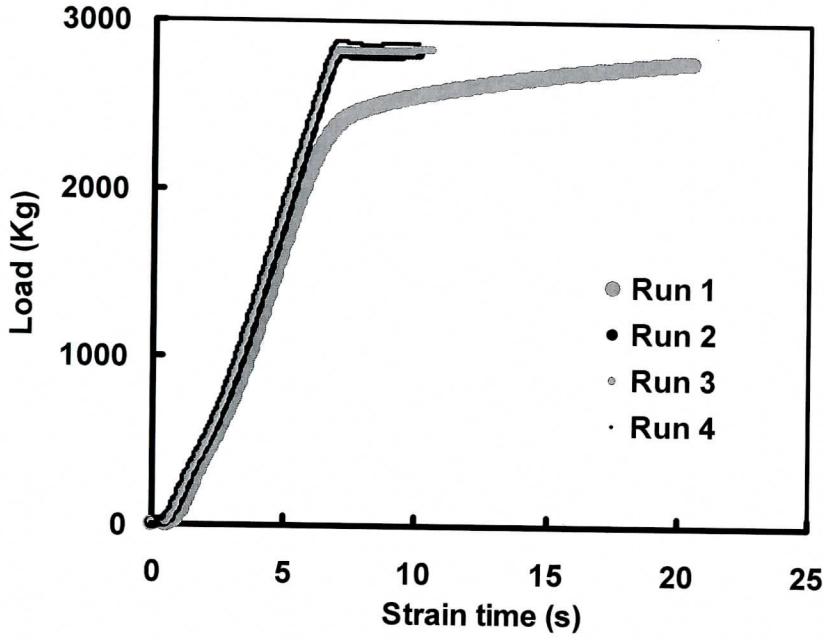

(b)

Figure 3.4: Tensile tests for SS304 using load-unload-reload cycles; all tests operated potentiostatically at -250 mV (Ag/AgCl) at a constant pulling rate of 0.254 mm/s: (a) transient currents and (b) Load. Run 1: 20% strain and Runs 2-4 each 10% strain. (Non-Q: For Information Only)

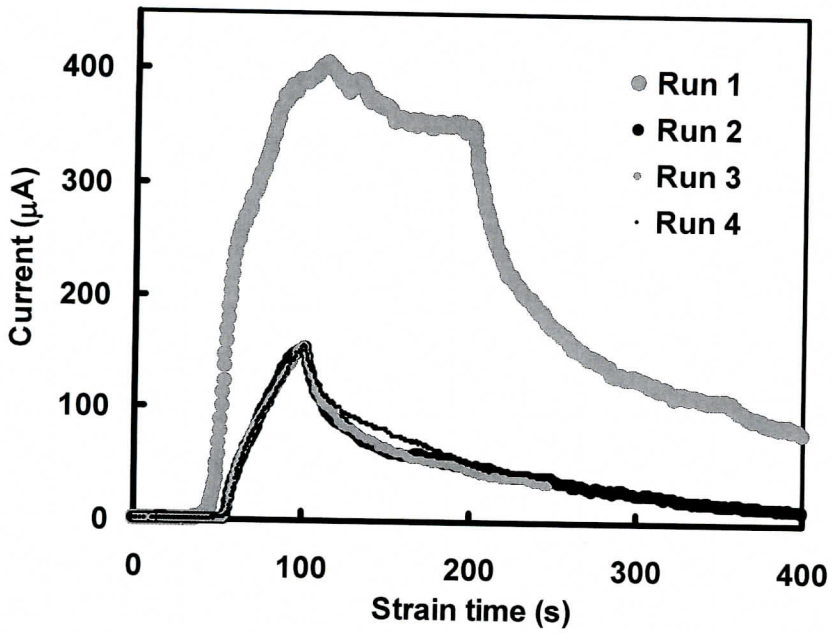

Figure 3.5: Transient currents of four tensile tests for SS304 using load-unload-reload cycles; the pulling rate is 0.0254 mm/s and the potential is -250 mV (Ag/AgCl). (Non-Q: For Information Only)

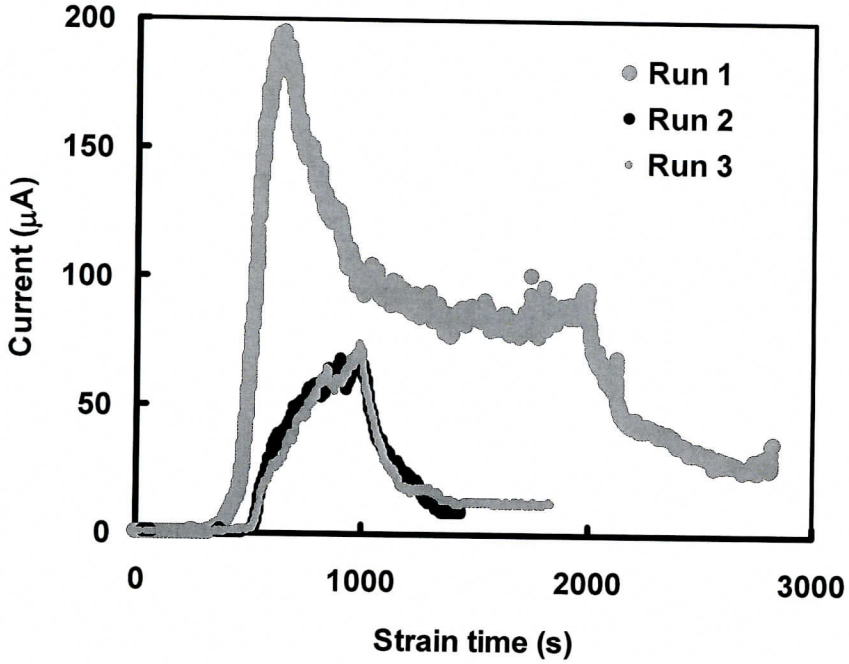

Figure 3.6: Transient currents of three tensile tests for SS304 using load-unload-reload cycles; the pulling rate is 0.00254 mm/s and the potential is -250 mV (Ag/AgCl). (Non-Q: For Information Only)

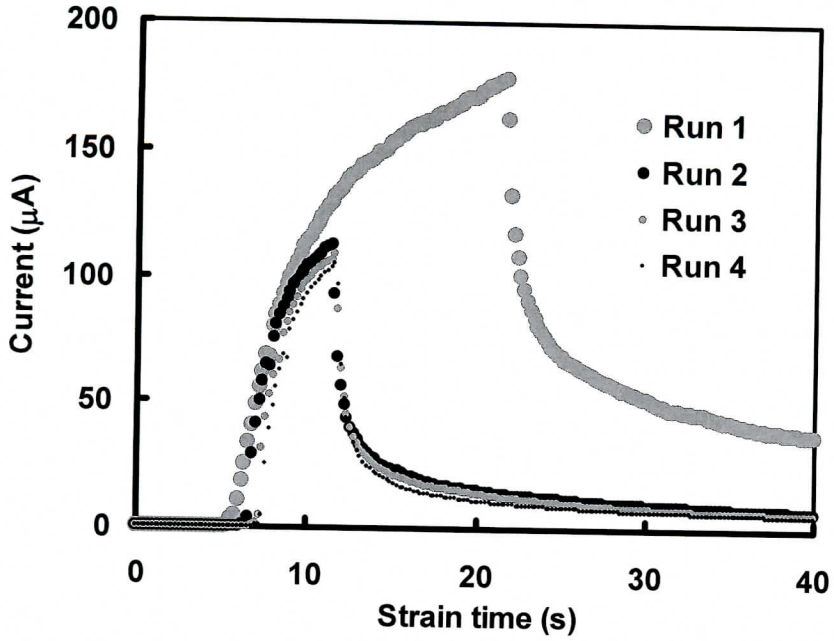

(a)

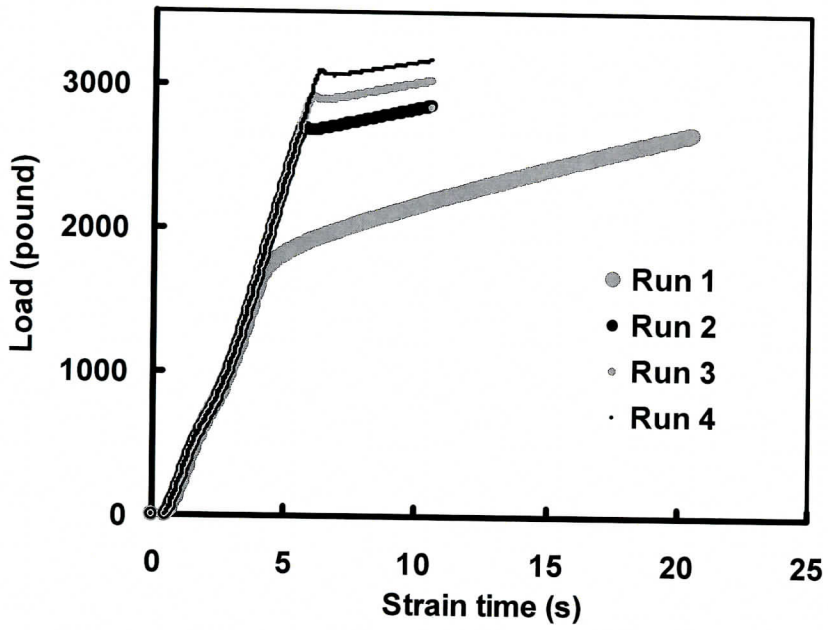

(b)

Figure 3.7: Tensile tests for Alloy-22 using load-unload-reload cycles; all tests operated potentiostatically at -250 mV (Ag/AgCl) at a constant pulling rate of 0.254 mm/s: (a) transient currents and (b) Load. Run 1: 20% strain and Runs 2-4 each 10% strain. (Non-Q: For Information Only)

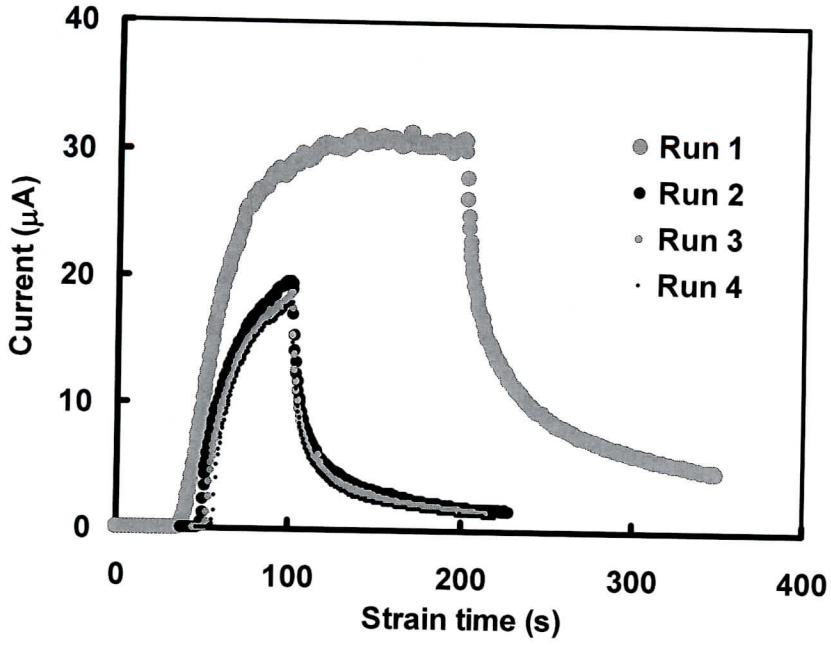

Figure 3.8: Transient currents of four tensile tests for Alloy-22 using load-unload-reload cycles; the pulling rate is 0.0254 mm/s and the potential is -250 mV (Ag/AgCl). (Non-Q: For Information Only)

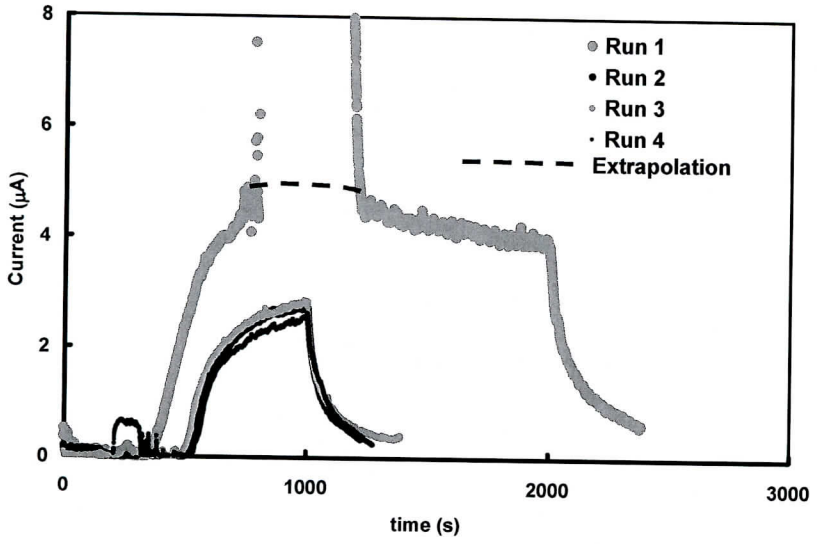

Figure 3.9: Transient currents of four tensile tests for Alloy-22 using load-unload-reload cycles; the pulling rate is 0.00254 mm/s and the potential is -250 mV (Ag/AgCl). The dashed curve simply connects the broken data lost due to an electrolyte leakage. (Non-Q: For Information Only)

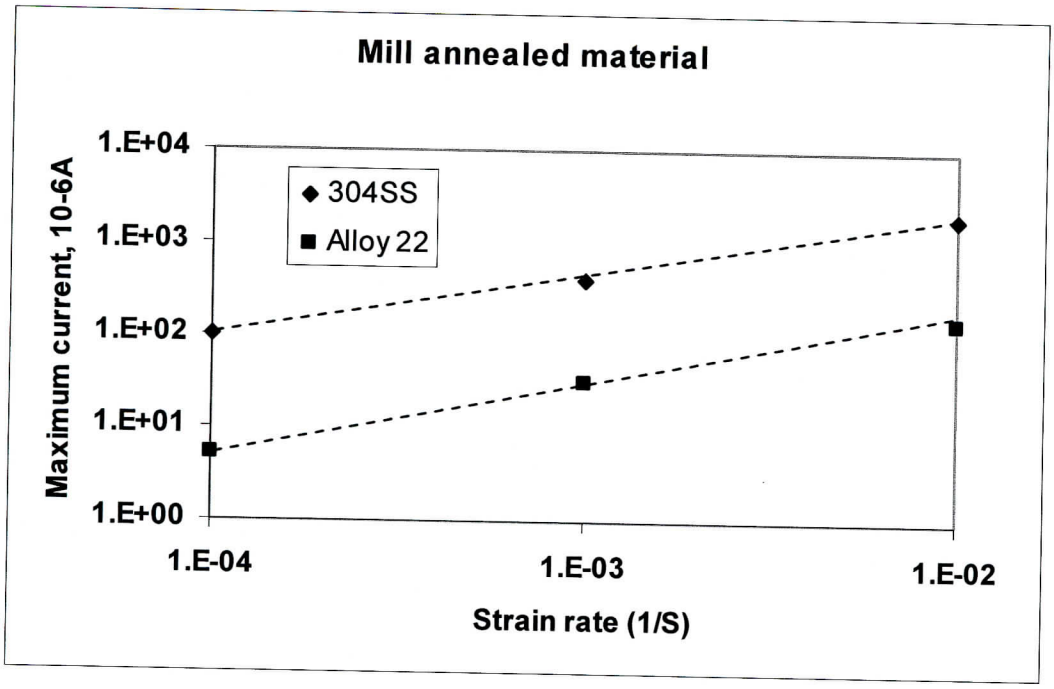

Figure 3.10(a): Maximum recorded current during straining of the specimen in mill-annealed condition as a function of strain rate. (Non-Q: For Information Only)

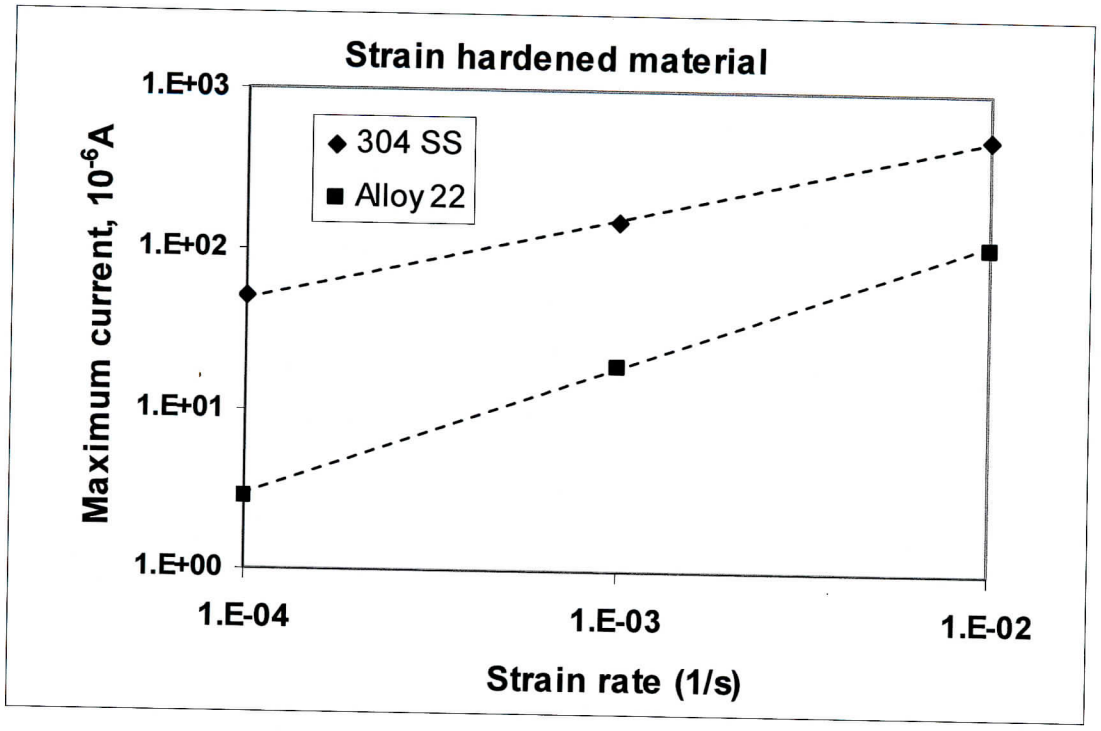

Figure 3.10(b): Maximum recorded current during straining of the specimen in strain hardened condition as a function of strain rate. (Non-Q: For Information Only)

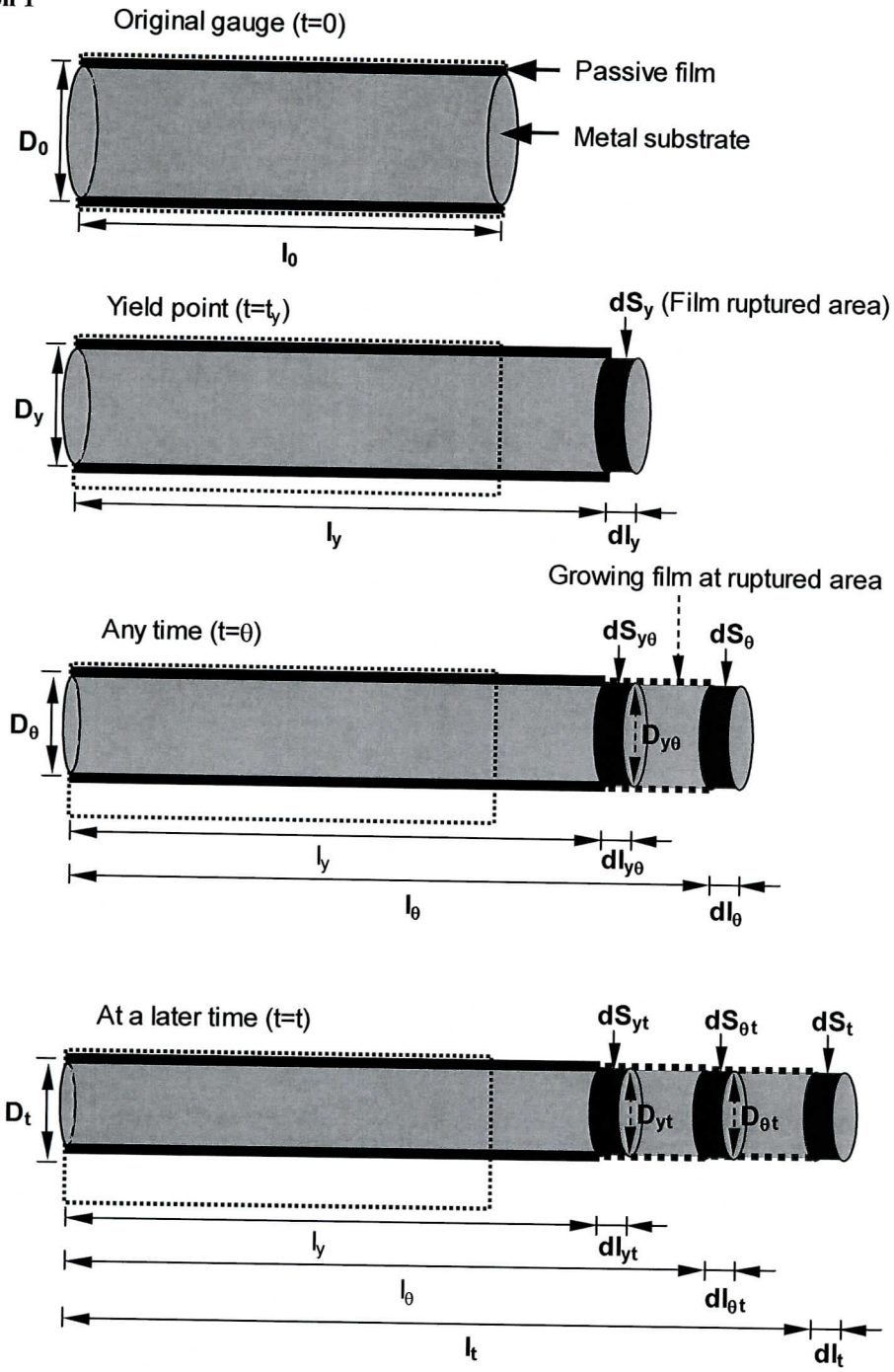

Figure 3.11: Schematic for variation of gauge geometrical parameters with elongation. (Non-Q: For Information Only)

Methodology Development/Corroborative Work: 4. SUBTASK 1b: Plasticity Enhanced by High Anodic Current Densities at Film Rupture Sites

4.1 Introduction

During the course of research outlined in the Scientific Investigation Plan (SIP-UNR-014) it became apparent that additional Creep experiments were required to determine the effect of high anodic current densities at the film rupture sites in the passive films of Alloy-22. The research in this subtask was scoping work and method development performed to meet this necessity. The method was developed using 304SS specimens because 304SS has been extensively studied and its performance under similar test conditions is well characterized making it the ideal choice for method development and verification. Unqualified 304SS was used to minimize cost and expedite schedules of the method development task. All other aspects of experiments performed during method development were carried out in compliance with the UCCSN QA Program. ***The testing procedures and techniques established in this subtask were used in generate quality-affecting data for the Q half of subtask #1b, "Plasticity Enhanced by High Anodic Current Densities at Film Rupture Sites."***

In his model for unified mechanism of stress corrosion cracking Jones[1,2] proposed that brittle crack initiation could occur due to development of a local plastic region beneath the passive film rupture sites which has been mechanically constrained by surrounding rigid metal covered by passive film. Divacancies generated by the anodic dissolution of the film rupture sites are considered to annihilate strain hardening and promote local plastic regions at the near-surface volume of the slip bands. Relief of strain hardening due to vacancy-dislocation interaction would result in increase in creep strain[2]. The correlation between creep and SCC has been observed by many researchers. In Andresen and Ford[3] model on SCC crack growth, the rupture of passive film was considered to occur by accumulation of creep strain. Was and co-workers[4,5,6] also considered creep as a predominant factor controlling SCC of Alloy 600 components in pressurized water reactor environments. Increased steady state creep rate was observed in water as compared to argon (inert) environment at 360°C[5].

Nishimura and co-workers[7,8,9,10] studied SCC of austenitic and ferritic stainless steels in 0.83 M H_2SO_4 and 0.83 M HCl solutions at 80°C and observed a correlation between steady state creep rate and SCC failure time. The deformation of specimens exposed to corrosive environments revealed three regions similar to that high temperature creep elongation vs. time curve viz., primary creep region controlled by applied stress and considered as crack incubation period, a secondary region which showed a steady state elongation correlated to the crack induction process and tertiary creep which occurred due to crack propagation and reduction in net-cross section leading to fracture. The SCC failures in laboratory scale required a minimum steady state creep rate of 10^{-10} m/s.

Revie and Uhlig[11,68] studied the effect of impressed anodic and cathodic currents on the creep behavior of thin copper wire in deaerated acetate buffer solutions. In the absence of corrosion, the creep strain followed a logarithmic relation with time as in the case of ambient air. When an external anodic current density of 0.9 mA/cm^2 (corresponding to a dissolution rate of 0.33 nm/s) was impressed on the specimens under a tensile load, the creep rate increased by several folds. Similar effects were observed for cathodic current densities also.

Even though low temperature creep is not a predominant failure mechanism of engineering components that are not exposed to corrosive environments, creep strain has been associated with SCC failures. Therefore, it is important to study the low temperature creep behavior of Alloy-22 in corrosive environments in order to understand its effect on SCC. In general, SCC is reported to occur over a range of electrochemical potentials at which passivity is observed. Corrosion potential of an ambient environment drifts in the noble direction in the presence of dissolved oxidizers. Carrying out creep experiments under constant electrochemical potentials may or may not represent the real environmental conditions. In order to investigate the passivation behavior by simulating the enoblement / drifting of potential in the presence of dissolved oxidizers, an open circuit reference electrode (OCRE) technique was proposed[12]. In this technique, the potential of the working electrode (in de-aerated environment) was potentiostatically controlled to follow the corrosion potential of a reference electrode (having identical chemistry and geometry as that of working electrode) exposed to the environment with dissolved oxidizers. The OCRE technique was followed to study the current transient behavior of the creeping specimen. In this case the corrosion potential of the stressed specimens (working electrode) was polarized to follow the potential of the open circuit reference electrode (OCRE), which was an unstressed specimen with identical material conditions.

The objectives of this study are:

- To investigate the creep behavior of Alloy-22 in chloride containing environments and to correlate the current transients observed with the creep elongation with crack initiation events.
- To investigate the creep-corrosion interaction of type 304 SS in the above environments for comparison, as it expected that SCC could be observed in 304 SS and not in Alloy-22.
- To understand the role of vacancy flux (created during corrosion process) on the creep deformation and its implication to SCC.

4.2 Experimental

Material

304 SS was procured in mill-annealed condition (Talley Metals Technology Inc., Hartsville, SC). The chemical composition of the material and other properties were (as provided by the mill sheet of the supplier, certificate serial # 000363792, dated 11/27/02,

[68] R. W. Revie and H. H. Uhlig, Acta Metall., 22 (1974) 619

Heat # G7421): 0.016% C, 0.4% Si, 0.028% S, 0.028% P, 1.72% Mn, 18.48% Cr, 8.66% Ni 0.48% Mo, 0.41% Cu, 0.19% Co, 0.075% N and Fe balance. Grain size: ASTM 4, 0.2% Yield strength ~77000 psi, Tensile strength: 102000 psi, %elongation: 43.

In this investigation, specimens were tested in mill-annealed condition and sensitized condition. Sensitization of 304 SS was carried out in a muffle furnace at 680°C (furnace-set temperature) for 24 h. However, the actual aging temperature of the specimens was not known.

Tensile Specimen

Tensile specimens with a gage length of 25.4 mm (1.0 in) and gage diameter of 5.1 mm (0.2 in) were machined out of the as received plate stock. Other dimensions of the specimen are shown in Fig. 4.1(a). The shoulders of the specimens were masked with a thin epoxy coating to avoid any crevice type corrosion between the O-ring seal and the metal surface. Gage length portion of the specimen was polished down to 600 grit emery paper and thoroughly washed with alcohol and distilled water before introducing it into the electrochemical cell.

Environment:

The creep tests of 304 SS were carried out in different environments such as:

- 3.9 M NaCl + 0.1 M HCl solution at 80°C (mill-annealed specimens only).
- 5 N H_2SO_4 + 0.5 N NaCl at 30°C (mill-annealed specimens only).
- 0.5 M $Na_2S_2O_3$ at 30°C(sensitized specimen only)

The temperatures were controlled by a PID temperature controller and a J-type thermocouple.

Electrochemical Cell

The electrochemical test cell (Fig. 4.1 (b)) had a 130 mm diameter, 100 mm long and 7 mm thick-wall glass tube secured between two 12.5 mm thick PTFE circular lids with the help of four 4mm diameter stainless steel tie rods. Two O-rings provided leak proof seal between the flat ends of the glass tube and the PTFE lids. Required number of ports were provided in the PTFE lids to accommodate the tensile specimen, counter electrode (2 mm Pt rod), reference electrode (Ag/AgCl), heating element, gas purge, thermocouple, and a condenser. An extra port was provided to accommodate the open-circuit reference electrode (OCRE). The OCRE, an 11 mm diameter and 100 mm long cylindrical rod, had similar composition as that of the working electrode, but it was not loaded. The immersed length of the OCRE was about 50 mm. The solution was heated with a quartz heating element (16 mm dia. and 75 mm heating length, Glo-quartz, Tucson, AZ).

Creep Loading Frame

Constant load type creep frames (Applied Test System, PA) with a lever-arm ratio of 20 were used for creep studies (Fig. 4.1(c)). The weights in the loading pan and the resulting load on the specimens were calibrated against a NIST certified load cell using standard

QA procedures (Bechtel Nevada). The error in the load calculations using a magnification factor of 20 was less than 0.2 % between 0-20000 lbs. The loading lever was maintained in the horizontal position as the specimen deformed with the help of a magnetic-level relay circuit. The lever adjusted itself to the initial horizontal position to the ground for every 0.08 mm elongation of the specimen.

Measurement of Deformation

Creep deformation was measured by using a plunger-type digital indicator with a least count of 0.01 mm (Mitutoyo, Digimatic Model-S1012E). The digital indicator was mounted on a low-alloy steel bracket which again was secured to the end of one shoulder of the specimen using two nuts. The plunger of the indicator was activated by attaching a long cylindrical rod-bracket assembly to the other end of the shoulder of the specimen. Thus, the extension of the specimen recorded included not only the extension of the gage length but also the entire length of the specimen excluding the threaded portions. As the diameter of the specimen shoulder was more than two times of the gage diameter, the observed creep elongation could be attributed to the reduced cross section only.

Constant Load Creep Testing Under Electrochemical Conditions

Constant load creep tests were carried out on 304 SS specimens in different electrochemical conditions viz., 1. under open circuit reference electrode (OCRE) condition (both mill-annealed and sensitized specimens), 2. under applied cathodic potential (-400 mV) with reference to a standard reference electrode Ag/AgCl electrode (only mill-annealed specimen), and 3. under an applied constant current (-100mA) conditions. In case of OCRE condition, the corrosion potential of the stressed creep tensile specimen is polarized and made to follow the free corrosion potential of the unstressed specimen having identical chemistry of that of creep specimen. For OCRE test condition, the connection of the potentiostat to the electrochemical cell is as followed: the working electrode (creep tensile specimen) is connected to the working electrode terminal of the potentiostat. Platinum counter electrode is connected to the auxiliary electrode lead. The OCRE (unstressed identical material specimen) is connected to the reference lead of the potentiostat. In order to make the potential of the stressed specimen to follow the corrosion potential of the unstressed specimen, the applied potential is set to zero vs. reference electrode (OCRE in this case) in the potentiostatic menu. Both the working electrode and the OCRE were in the same non-deaerated solution. Therefore, the potential difference occurred because of the stressed condition of the working electrode as against the un-stressed condition of the OCRE.

The specimen was conditioned to reach a steady state free corrosion potential (in case of OCRE condition) for about an hour before loading. Then the potential of the specimen (WE) was set at 0 V with reference to OCRE. In unstressed condition, open circuit corrosion potentials of both WE and OCRE would be same. Therefore, measured current also would be almost zero. Then the specimen would be stressed to a required level by adding weights to the weight pan of the creep frame. The creep frame has lever-arm ratio of 20:1 which means, addition of 10 lbs to the weight pan will result in a load of 200 lbs to the specimen.

The calculation of required weight to be placed on the pan is as followed:

$$W = (SxA)/R \quad (4.1)$$

Where, W = weight on the pan, pounds
S = required stress on the specimen, in psi
A = Area of the specimen gage cross section, in squared inch
R = lever arm ratio, 20 in this case.

Extra tare weight required for balancing the arm at zero load should be added to the calculated weight, W.

The average 0.1% yield strength of the 304 SS = 69000 psi
Gage diameter = 0.2 inch
Area of cross section of the gage: $\pi D^2/4$ = 0.031416 sq.in or 20.27 mm^2
Load corresponding to yield = 69000*0.031416 = 2167 lbs
Load Corresponding to ~97% yield strength: 2167*0.97 = 2103 lbs ~2100lbs
Load Corresponding to ~110 % yield: 2167*1.1 = 2384 lbs ~2400lbs

The creep elongation measurement started as soon as the specimen was loaded in increments of 600 lbs. Immediately after loading the specimens to the desired stress level (generally varied from 90 – 110 % of the yield strength), the specimen deformed at a faster rate. The change in dial indicator reading was noted for every 15 seconds during initial one hour after loading. When the deformation rate slowed down, the time taken for every 0.01 mm elongation was noted.

If SCC did not occur, the creep strain rate of the specimen decreased with time and the elongation was less than 0.03 mm per day (>0.01 mm/8h). In such case, the specimen was unloaded and loaded again to a higher value (about 5% higher than its previous load). Creep elongation and current transients were measured with each increment of load.

4.3 Results

Figure 4.2 shows the results of constant load creep tests under OCRE conditions, loaded at 2100 lbs (97% of 0.1% yield strength (YS)) of 304 SS (mill-annealed) in 3.9 M NaCl + 0.1 M HCl solution at 80°C. The creep strain and corrosion current have been plotted as a function of time. The total strain recorded during creep had two components viz., 1. elastic strain and 2. inelastic strain, which included both instantaneous plastic strain and time dependant creep strain. Time dependant inelastic strain was observed on the specimen loaded below the yield strength of the material. As the specimens were loaded abruptly to the desired load levels, very high plastic strains were observed. Higher observed strains could be partly attributed to the higher corrosion currents also. The instantaneous strain rate after applying the 2100 lbs of load in steps of 600 + 600 + 600 + 300 lbs was about 5 $x10^{-5}$/s. This creep strain rate decreased logarithmically in the primary creep region. After exhaustion of the primary creep, a secondary creep process

followed with a steady state creep strain rate. The calculated steady state creep rate was 2.2 $x10^{-6}$/s. Tertiary creep usually follows the steady state creep. However, in this experiment, the tertiary creep occurred too abruptly and it was not possible to note the change in elongation with time manually.

The corrosion current increased sharply immediately after loading. This current was the result of anodic polarization of stressed creep specimen with reference to the corrosion potential of the un-stressed 304 SS specimen immersed in the same electrolyte. The positive current was an indication that the surface of the creep specimen became more active when stressed. As very large current was recorded, it is tempting to assume that dissolution could be concentrated on slip steps. During steady state creep process, the corrosion current started decreasing with time. This could be attributed to the formation of a re-precipitated salt layer on the specimen surface. The volume of the test electrolyte was about a liter and it was static. Large amount metal ions were dissolved in the electrolyte initially as indicated by the high magnitude of the corrosion current. After reaching the solubility limit, these ions started precipitating on the surface of the specimen. Decrease in corrosion current resulted in decrease in creep strain rate as observed in Fig. 4.2. Nishimura[7] attributed the steady state creep rate to the crack nucleation and growth events. Coalescence of small cracks created a single large crack and initiated the tertiary creep process. Sharp increase in current was observed during tertiary creep. The 304 SS (mill-annealed) specimen failed within 25.6 hours by SCC in 3.9 M NaCl+0.1 M HCl solution at 80 C under 97% of YS load.

Fig. 4.3 shows the results of constant load creep tests under OCRE conditions, loaded at about 2400 lbs (110% of 0.1% YS), of 304 SS (mill-annealed in 3.9 M NaCl + 0.1 M HCl solution at 80°C. Initially the specimen was loaded at 2370 lbs. The instantaneous creep strain rate immediately after loading was about $1.4x10^{-4}$/s, which exhausted logarithmically during primary creep region. Competition between preferential corrosion at the slip steps and the strain hardening resulted in secondary creep process with a steady state creep strain rate of $1.28x10^{-5}$/s. During steady state creep, the load was increased by 30 lbs. This small increase in load could unlock the dislocations piled-up due to strain hardening in the steady state creep process. Therefore, a brief primary creep was observed before these newly activated dislocations were trapped during strain hardening process. The steady state creep strain rate increased to $3x10^{-5}$/s with the small increase in load.

The corrosion current increased sharply with initial stressing of the specimen and reached more or less a steady state during secondary creep process. The addition of small load increased the current significantly and the increase was monotonous till failure. The specimen failed within 2.5 hours. As the total charge released during this creep test was less than the previous case (for which the failure time was about 25 h with about similar magnitude of current) not much of salt film could be observed on the specimen surface that affected the current.

Fig. 4.4 shows the creep test results of 304 SS (mill-annealed) in OCRE condition with a constant load of 2400 lbs in 3.9 M NaCl + 0.1 M HCl solution at 80°C. This test was almost a repetition of the previously described test with an exception that 2400 lbs of load was applied from the beginning of the test. The specimen failed by SCC within 1.75 h. The steady state creep strain rate was 2.6×10^{-5}/s. The corrosion current increased steadily with increase in creep strain. Multiple cracks were seen on the specimen surface. Active dissolution at the crack tips was evident.

Fig. 4.5 shows the results of creep test in 5 N H_2SO_4 + 0.5 N NaCl solution at 30°C under OCRE condition when loaded at 2100 lbs (97% of 0.1% YS) of 304 SS (mill-annealed). The specimen failed by SCC within 24.4 hours. Initially the increase in corrosion current was not significant. The steady state creep strain rate was about $2\text{-}3 \times 10^{-6}$/s, an order of magnitude lower than that observed in 3.9 M NaCl +0.1 M HCl solution at 80°C for similar load condition. This could be attributed to the lower current values observed during initial creep. The increase in strain during secondary creep was marginal. Low current values and small increase in strain indicate that presence of presumably a passive film on the surface could as a barrier to dislocation movements. Most of the creep strain occurred during tertiary creep showing exponential relation with time. The corrosion current also showed exponential increase with time in the tertiary creep region.

Fig. 4.6 shows the results of creep test of 304 SS (mill-annealed) at -400 mV (Ag/AgCl) in N H_2SO_4 + 0.5 N NaCl solution at 30°C. No SCC failure could be observed. The primary creep region showed a semi-logarithmic relation with time. Exhaustion of primary creep was not followed by steady state creep unlike in the previous experiments. Trapped dislocations were reactivated by complete unloading-reloading-to a higher value-event. Increase in load increased the instantaneous strain rate followed by exhaustion of mobile dislocation. No steady state creep rate was observed under at cathodic potential of -400 mV. Application of a constant cathodic current of -100 mA also did not affect the creep behavior of the material.

Fig. 4.7 shows the results of creep test of 304 SS (sensitized) in 0.5 M $Na_2S_2O_3$ solution at 30°C under OCRE test condition. SCC was not observed on the specimen after 97 hours of exposure and the test was interrupted. The absence of SCC failure on this specimen could be attributed to improper sensitization of the material. Initially it was assumed that the carbon content of the material was about 0.04% and sensitization was carried out at 680°C for 24 h. Later, the mill-sheet indicated that the carbon content of the material was low (0.016%), which required longer aging times (>100h) and lower temperatures (600-650°C) for a continuous sensitized grain boundary network. Double loop EPR test carried out on the sensitized specimens in 0.5 M H_2SO_4 + 0.01 M KSCN solution at 30°C showed a reactivation current ratio of 0.04. Microstructural observations indicated only discrete carbide precipitations along the grain boundaries along with intra-granular precipitation. Absence of continuous network of carbide precipitation along the grain boundaries could be attributed to the absence of intergranular SCC in this material. Therefore, only primary creep regions could be observed during creep tests with incremental load conditions. The corrosion current was very low in general. Initial loading to 2200 lbs caused a sharp increase in corrosion current to 17.6 μA, which

decayed with time. Second large current spike of 4.62 μA was observed when the load increased to 2400 lbs. Increase in loads to 2500 and 2600 lbs resulted in current spikes of 0.2 and 0.37 μA respectively.

Fig 4.8 (a)–(d) and 4.9 (a)-(c) show the creep strain rate vs. time plots in log-log scale which were re-plotted from the creep strain vs. time data. Fig. 4.8 (a) shows the creep strain rate vs. time for 304 SS (mill-annealed) under a cathodic potential of -400 mV. Initially the creep strain rate was 3.08×10^{-6}/s which decayed to 4.2×10^{-9}/s with a slope of -1 in log-log scale in 24 h. Fig. 4.8 (b) shows the change in creep strain rate with time when the specimen already crept at 1900 lbs was unloaded and reloaded to 2100 lbs. The creep strain rate 1.85×10^{-5}/s decayed to 5.9×10^{-9}/s in about 87 h with a slope of -0.88. Further increase in load to 2400 lbs caused increase in strain rate (2.7×10^{-4}/s), which decayed with a slope of -0.95 to 1.47×10^{-7}/s within 25 h, as shown in Fig. 4.8 (c). Similar results were observed for 2500 lbs load condition also. The initial strain rate was 7.4×10^{-5}/s, which decayed with a slope of -1 to 4.1×10^{-8}/s, as shown in Fig. 4.8 (d).

Sensitized 304 SS in 0.5 M $Na_2S_2O_3$ solution also showed similar creep strain rate decay behavior as described above. Initial loading at 2200 lbs caused a strain rate of 5.3×10^{-5}/s, which decayed with a slope of -1 to 2.6×10^{-8}/s within 22 h, as shown in Fig. 4.9(a). Increasing the load to 2400 lbs resulted in a strain rate of 1.84×10^{-4}/s. The strain rate decreased with log time with a slope of -0.96 to a value of 8.3×10^{-8}/s within 22 h as given in Fig. 4.9 (b). Fig. 4.9(c) shows the creep strain rate for 2500 lbs load condition. The initial creep strain rate of 7.8×10^{-6}/s decayed with log time with a slope of -1 to 3.6×10^{-8}/s within 29.2 h.

4.4 Discussion

4.4.1 OCRE

When the specimen was loaded, initially very faster increase in strain could be observed. As the increase in strain was noted manually from the digital indicator, it was not possible to determine the instantaneous rate of change of strain. Similar observations were made by other researchers also[14,15,16]. A. H. Cottrell[16] also observed instantaneous high strain rates as soon as the desired stress was applied completely to the specimens. The observation, that occurrence of abrupt strain rate when the specimen was loaded above yield point and falling of this strain rate to lower values upon stopping the loading ($d\sigma/dt = 0$) was considered as an evidence that the strain rate had two components viz, loading strain rate and creep strain rate. According to Alden[14], two kinds of strains are measured during deformation, which are caused by competition between thermal (viscous strain) and mechanical (plastic strain) release of dislocation segments from obstacles and sources. Plastic strain is time independent and creep is recovery controlled. At a given strain rate, the deformation by plastic strain is accomplished by a small number of mobile dislocations moving at a higher speed[15]. Whereas, in case of viscous strain, which is time dependant, the dislocation release occurs by thermal energy and strain rate is a function of stress and temperature. Viscous creep is glide controlled. Viscous flow occurs by high density of mobile dislocations moving at a lower speed[14].

Low temperature creep in ambient conditions (non corrosive environments) has been observed for austenitic stainless steels at the stress levels as low as 25% of the yield strength of the material[13]. Dislocations are responsible for plastic strain and dislocation density is considered to be a function of applied stress.

Total dislocation density of a material can be expressed as a function of applied stress as[14]:

$$\sigma = \sigma^* + \alpha.G.b.\rho_t^{0.5} \qquad (4.2)$$

σ = applied stress
σ^*= threshold stress above which dislocations multiply
α = a constant.
G = Shear Modulus
ρ_t = total dislocation density

Generally it is very difficult to measure the mobile dislocation density alone.

The creep strain rate is expressed as[15]:

$$\frac{d\varepsilon}{dt} = \rho_m b v \qquad (4.3)$$

where,
$d\varepsilon/dt$ = strain rate
v= dislocation velocity
b = Burgers vector
ρ_m = mobile dislocation density

The decrease in creep strain rate with time is attributed to two effects[13,14,15,16], viz., 1. decrease in mobile dislocation density and 2. decrease in velocity of mobile dislocations due to viscous drag. These effects could affect the creep strain rate either individually or in combination. Mobile dislocation density was observed to be affected by the magnitude of stress and stress rate and the dislocation velocity was affected by the stress rate[17]. Oehlert and Atrens[17] observed that when the specimens were loaded at different stress rates to the desired stress level, higher stress rate of loading resulted in higher creep rate. However, in the present investigation, the loading rate (stress rate) was not monitored as weights were added in steps to load the specimen with increments of 600 lbs initially and 300 or 100 lbs thereafter to obtain the desired magnitude. Same procedure was followed in all the tests so that rate of loading was more or less same in all the specimens.

As discussed earlier, the decreasing creep strain rate is the result of trapping of mobile dislocations as they interact with other dislocations. The progressively trapped dislocations pile up at the barrier, resulting in strain hardening of the material. Back stress caused by dislocation pile-ups retards the dislocation movement as the mobile dislocations are acted upon a viscous drag. In pure metals, like copper, the viscous drag was observed to be low as compared to that of stainless steel[15]. Higher viscous drag could

be attributed to the presence of solute atoms in substitutional and interstitial positions. When the load was increased to higher values the falling creep rate increased again. According to the relation (4.2), increase in applied stress should result increased total dislocation density, which indicates that new dislocations are emitted with increase in stress value. It is reasonable to assume that these new dislocations are mobile before they get trapped. Oehlert and Atrens[17] argued that trapped mobile dislocations may not be reactivated when the stress increased. This argument was based on their observation that the creep strain rate did not change when they unloaded the specimen by 25% and reloaded again back to the original value. Overall, during low temperature constant load creep process in an ambient non-corrosive environment, the continuous decrease in creep strain rate could be attributed to the strain hardening behavior of the material. In order to have a constant strain rate, the stress should be raised continuously so that the rate of trapping of mobile dislocation is equal to the rate of generation of mobile dislocations provided that the dislocation velocity remains constant. However, with strain hardening, more viscous drag force is expected to occur and the velocity will decrease. Therefore, in order to compensate for the decrease in mobile dislocation velocity, the density of mobile dislocation should increase with strain hardening for a steady state creep rate. Increase in temperature could help reactivating the trapped mobile dislocations, as the barriers are short range ordered.

When creep occurs in a corrosive environment under active conditions as investigated by Revie and Uhlig[11], substantial increase in creep strain rate was observed as compared to that in ambient conditions. Vacancies or divacancies that were created during anodic dissolution diffused into the specimen and interacted with dislocation arrays. Vacancy-dislocation interaction resulted in dislocation climb and easier slip, which increased the creep strain rate during creep process under anodic dissolution condition.

During OCRE tests in this present investigation, the stressed creep specimens were anodically polarized with respect to their unstressed counterparts. The change in corrosion potential due to stress can be expressed as

$$dE = -\sigma V_m/zF \,, \tag{4.4}$$

where, σ = tensile stress, Vm = molar volume, z= number of charge transfer, F = Faraday's constant.

Even though the difference between the corrosion potentials of stressed and unstressed specimens would be only a few millivolts according to the Nernst equation (4.4), relatively large currents were observed in this study. During deformation, higher dislocation pile-ups could be expected, as surface acts as a source of dislocation as well as obstacle for mobile dislocations[18]. At the dislocation pile-ups, the potential at the localized deformation sites could be more active than the surface area, which was free of dislocation pile ups. Assuming that there is a planar pile up of n dislocations, the local deformation potential may be expressed as[19]:

$$\Delta\varphi = \frac{\varepsilon_F n(\mu b)^2 A_1}{6e\pi^2 r^2 (1-\upsilon)^2} \tag{4.5}$$

where,
$\Delta\varphi$ = deformation potential
εF = Fermi energy
μ = shear modulus
n = number of dislocations in the pile-up
b = Burgers vector
r = radius of dilatation ~ 10 b
υ = Poisson's ratio
e = electronic charge
A1 = Constant

Assuming 10 dislocations in a pile up the estimated difference in deformation potential was about -160 mV, in case of copper[18]. Similar behavior could be expected in case of stainless steel also especially in sulfuric acid + chloride solution and NaCl solution at 80°C. Localized large potential difference at slip steps could result in large dissolution currents. Generation of vacancies due to this localized dissolution could interact with dislocation pile-ups aiding them to climb and annihilate strain hardening. During steady state creep process, it could be envisaged that localized dissolution process at the dislocation pile-ups/slip steps pumps in vacancies that unlocks the trapped dislocations balancing the rate of immobilization of dislocations (by strain hardening) and rate of creation of mobile dislocations (by unlocking trapped dislocations). In other words, during steady state creep, there is a balance between strain hardening (decrease in mobile dislocation density) and localized plasticity (increase in dislocation activity either by increase in velocity or mobile dislocation density). If sufficient amount of vacancies was not created, a steady state creep strain rate was not observed as in the case of cathodically polarized 304 SS (mill-annealed) and sensitized 304 SS in thiosulfate solution. These results clearly indicate that localized anodic dissolution should be present for increased dislocation activities. Absence of dissolution would not create vacancies and in turn would not result in annihilation of strain hardening. Limited number of experiments carried out in this investigation indicates that SCC is accompanied by a steady state creep strain rate. Nishimura[8] also observed similar results and proposed that if the steady state creep rate is below $4x10^{-9}$/s, no SCC could be observed in laboratory scale. A steady state creep strain rate is required for accumulation of strain for passive film rupture according to the SCC model proposed by Ford and Andresen[3]. Based on the results of the present investigation it is reasonable assume that anodic dissolution enhanced localized plasticity of the material which in turn increased/caused a steady state creep strain rate. SCC could be observed if the environment could cause localized active dissolution at the slip steps. However, it is not known how the dislocation activities at the surface are affected by the environment. As the surface energy of the material could be affected by the environment, reduction in surface energy could release the surface dislocations more easily, as described by Rehbinder effect.

4.5 Conclusions

304 SS (mill-annealed) failed by SCC in 3.9 M NaCl + 0.1 M HCl solution at 80°C under 97-110% of 0.1% YS loads and in 5 N H_2SO_4 + 0.5 N NaCl solution at 30°C within 25 hours.

A steady state creep strain rate was observed during SCC failures which varied from $2x10^{-6}$/s to $3x10^{-5}$/s. Anodic dissolution enhanced localized plasticity of 304 SS which in turn resulted in a steady state creep strain rate.

During cathodic polarization, when the anodic dissolution was not predominant, the creep strain rate decreased with time showing a linear relation in log-log plot. The slope of the strain rate decay with time was about -1, indicating strain hardening. A steady state creep strain rate was absent if the dissolution and in turn vacancy generation was not significant.

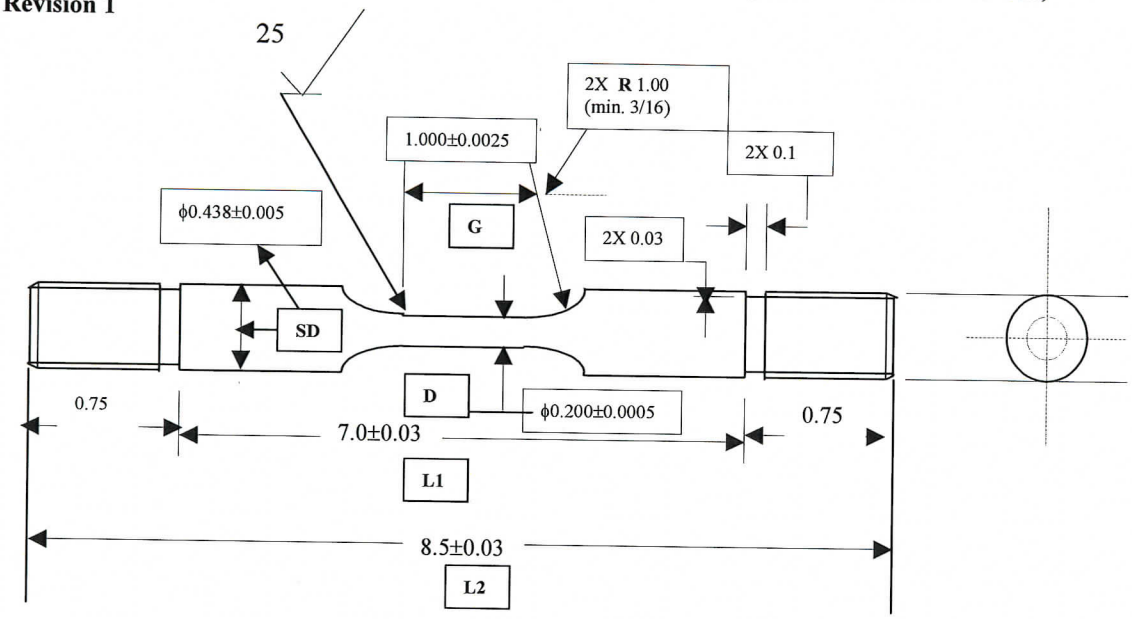

Figure. 4.1 (a) Schematic diagram of tensile specimen used in creep test. (Corroborative Data - For Information Only)

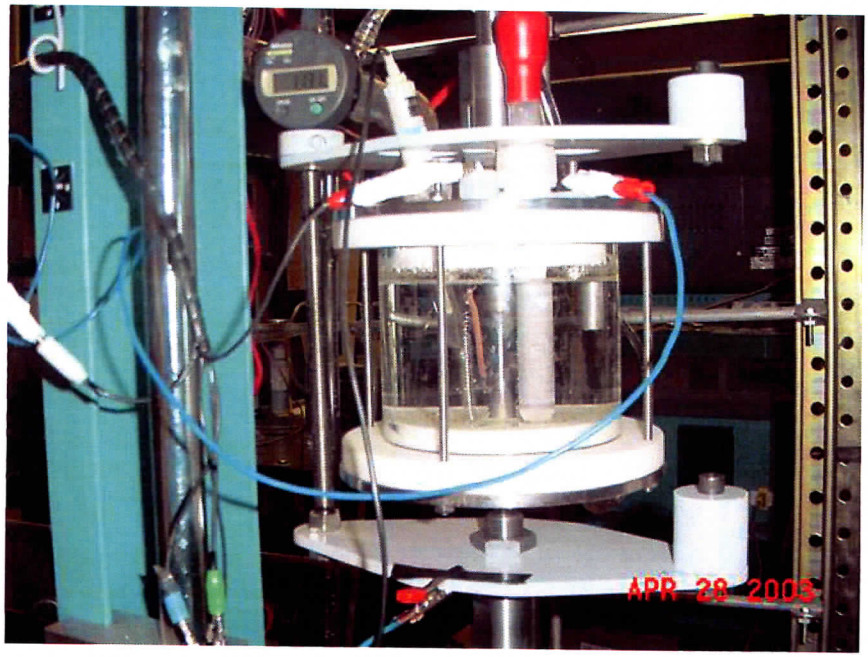

Figure. 4.1 (b) Electrochemical cell-dial indicator assembly for creep experiments (Corroborative Data - For Information Only)

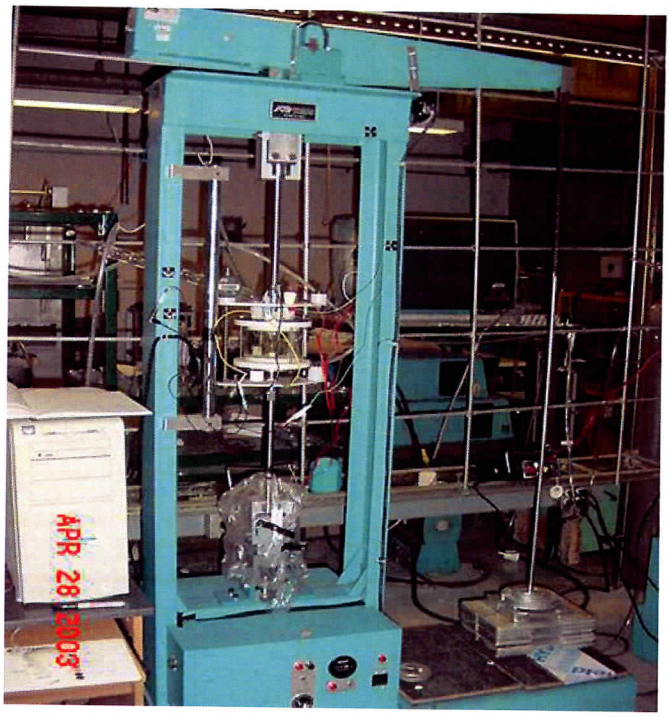

Figure. 4.1(c) Experimental Set-up for Creep Testing. (Corroborative Data - For Information Only)

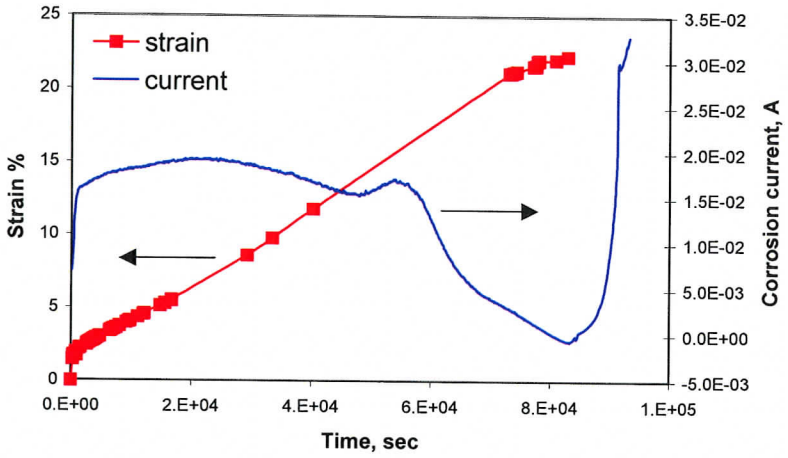

Figure. 4.2 Creep-corrosion current vs. time for 304 SS (mill-annealed) in 3.9 M NaCl + 0.1 M HCl at 80°C in OCRE condition. The specimen was loaded at 97% of yield strength of the material (2100 lbs). (Corroborative Data - For Information Only)

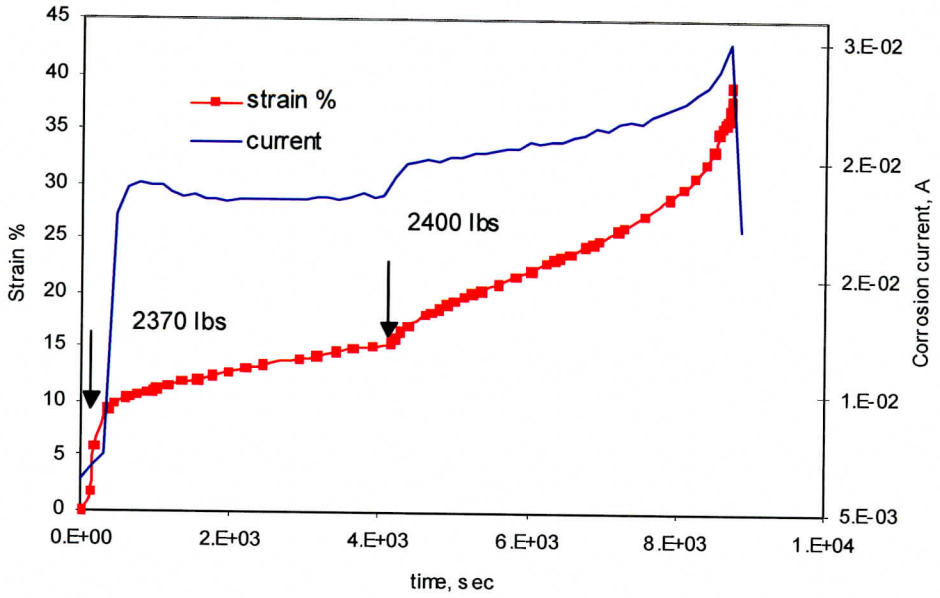

Figure. 4.3 Creep-corrosion current vs. time for 304 SS (mill-annealed) in 3.9 M NaCl + 0.1 M HCl at 80°C in OCRE condition. The specimen was loaded initially at 109.7% of yield strength of the material (2370 lbs), then the load was increased by 30 lbs to 2400 lbs. (Corroborative Data - For Information Only)

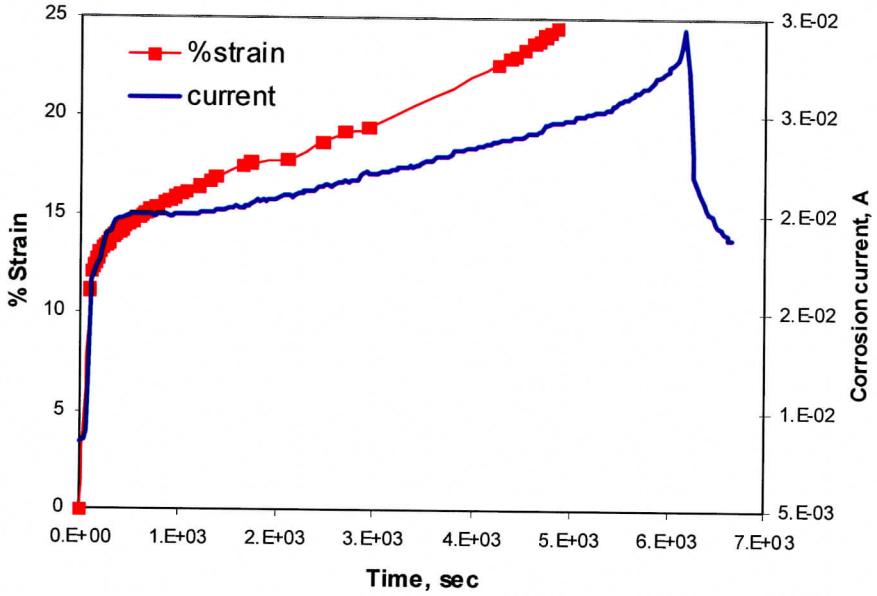

Figure. 4.4 Creep-corrosion current vs. time for 304 SS (mill-annealed) in 3.9 M NaCl + 0.1 M HCl at 80°C in OCRE condition. The specimen was loaded to 2400 lbs (110.75%) from the beginning of the creep test. (Corroborative Data - For Information Only)

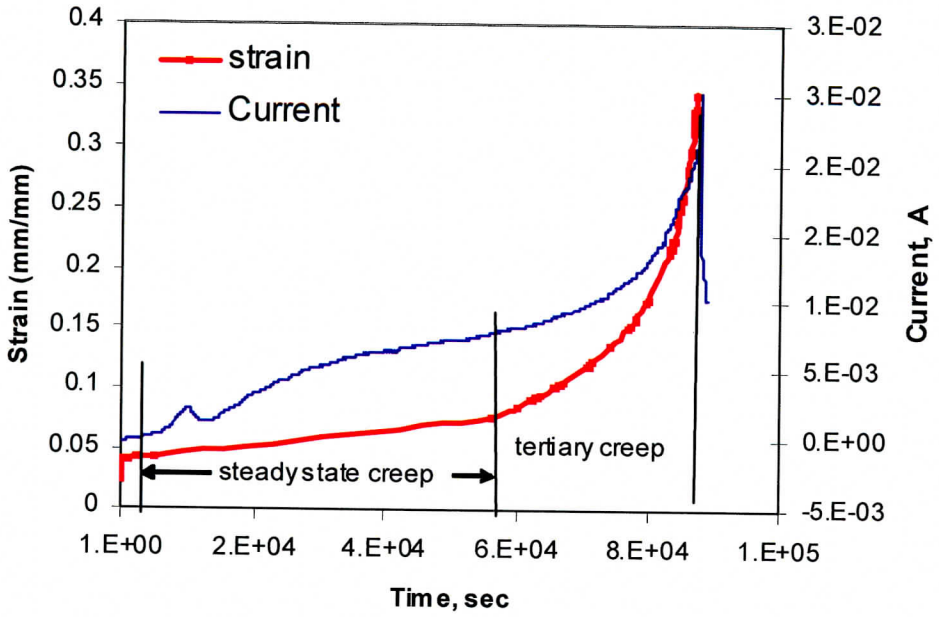

Figure. 4.5 Creep elongation of 304 SS (mill-annealed) in 5 N H_2SO_4 + 0.5 N NaCl solution at 30°C under OCRE test condition at 97% YS (2100 lbs). (Corroborative Data - For Information Only)

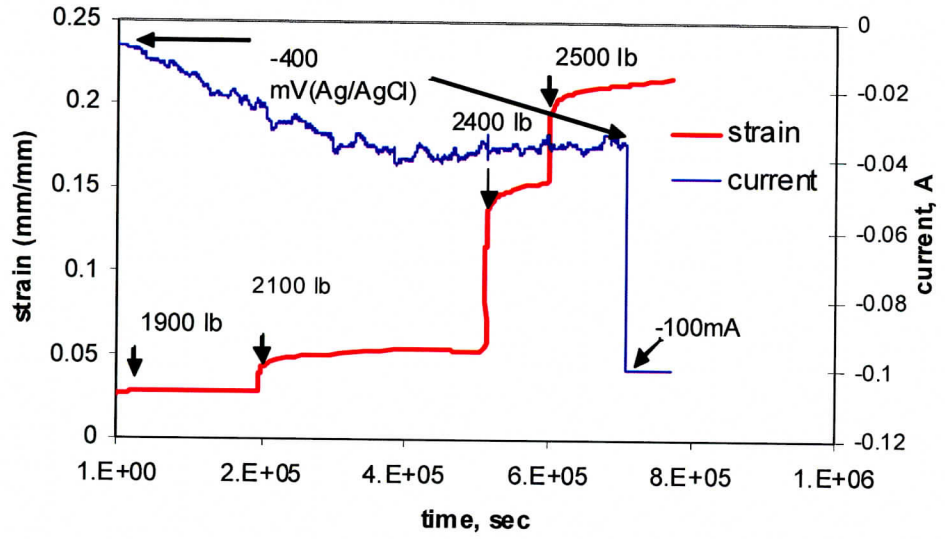

Figure. 4.6 Creep elongation of 304 SS (mill-annealed) in 5 N H_2SO_4 + 0.5 N NaCl solution at 30°C under a cathodic potential of -400 mV (at 1900–2500 lbs, 88-115% YS) and -100 mA (at 2500 lbs). (Corroborative Data - For Information Only)

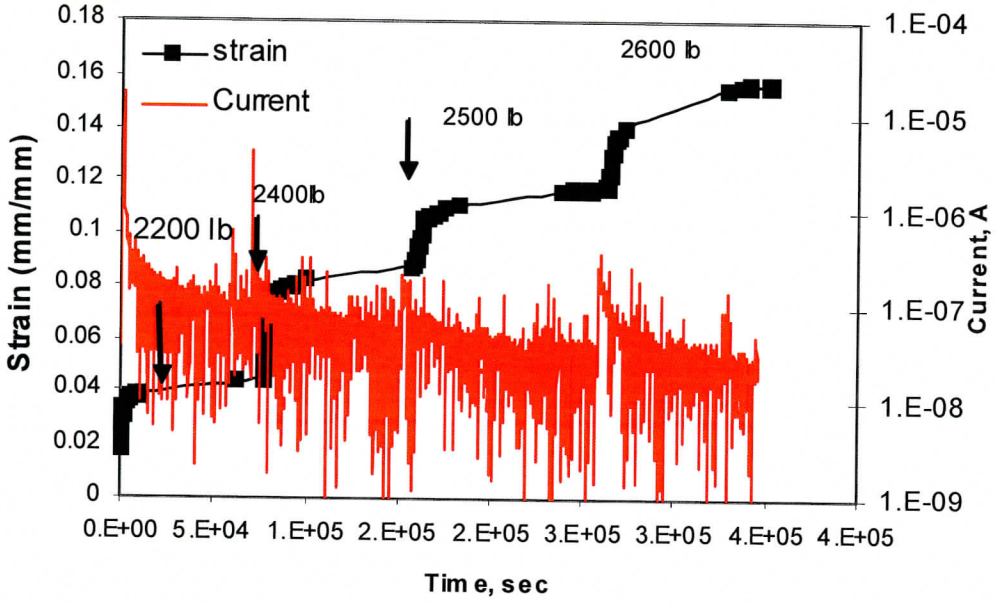

Figure. 4.7 Creep elongation of 304 SS (sensitized) in 0.5 M $Na_2S_2O_3$ solution at 30°C under OCRE test condition with different load levels, starting from 2200 lb – 2600 lbs. (Corroborative Data - For Information Only)

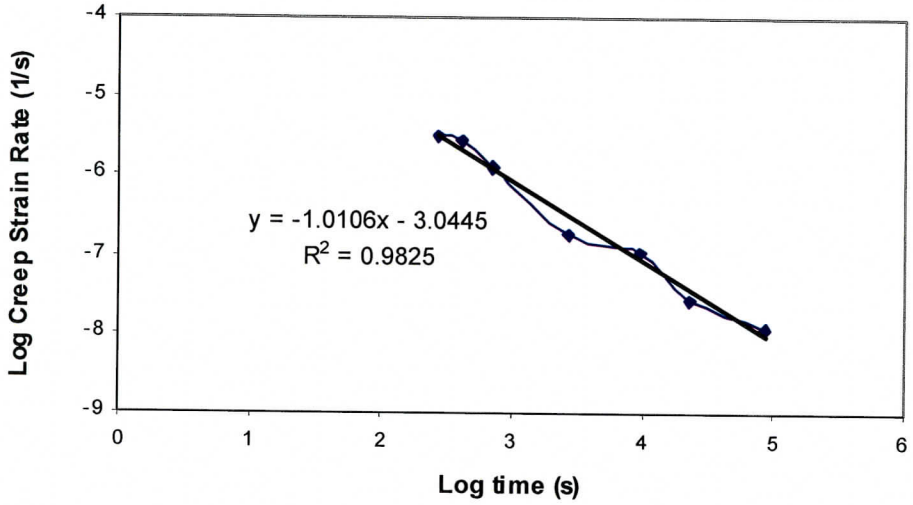

Figure. 4.8(a) Decreasing creep strain rate with time of 304 SS (mill-annealed) at -400 mV under a constant load of 1900 lb (88% YS) in 5 N H_2SO_4 + 0.5 N NaCl at 30°C (Corroborative Data - For Information Only)

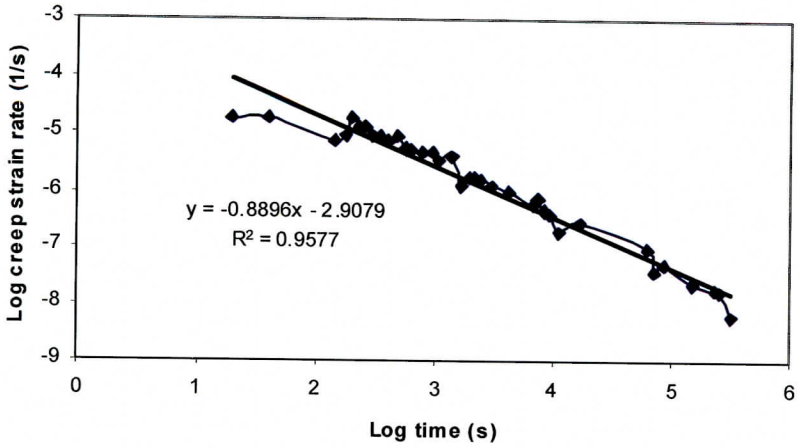

Figure. 4.8(b) Decreasing creep strain rate with time of 304 SS (mill-annealed) at -400 mV under a constant load of 2100 lb (97% YS) in 5 N H_2SO_4 + 0.5 N NaCl at 30°C. The specimen was unloaded from 1900 lbs and reloaded to 2100 lbs. (Corroborative Data - For Information Only)

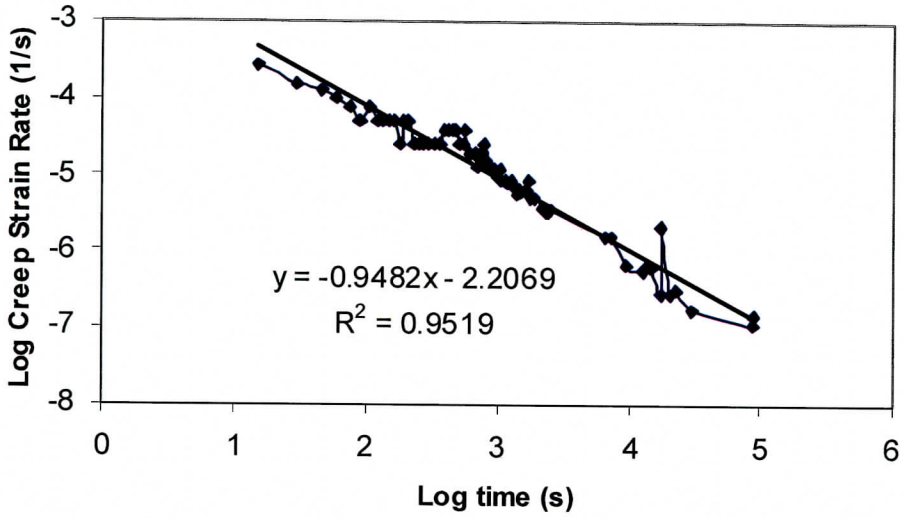

Figure. 4.8(c) Decreasing creep strain rate with time of 304 SS (mill-annealed) at -400 mV under a constant load of 2400 lb (110% YS)) in 5 N H_2SO_4 + 0.5 N NaCl at 30°C . The specimen was unloaded from 2100 lbs and reloaded to 2400 lbs. (Corroborative Data - For Information Only)

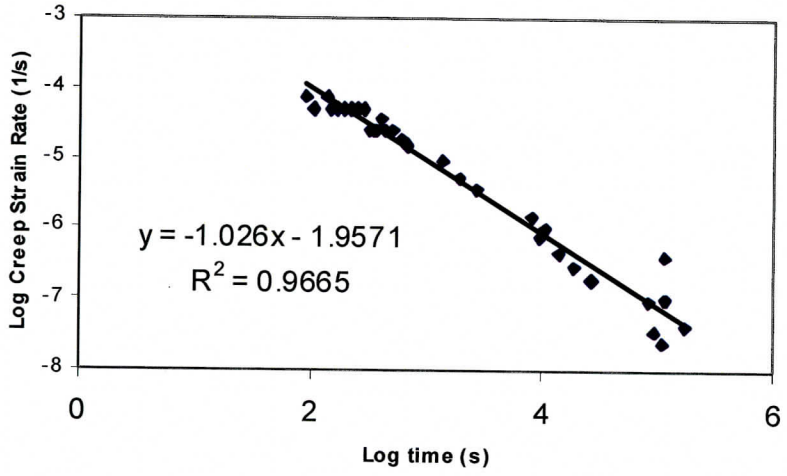

Figure. 4.8(d) Decreasing creep strain rate with time of 304 SS (mill-annealed) at -400 mV under a constant load of 2500 lb (115% YS)) in 5 N H_2SO_4 + 0.5 N NaCl at 30°C . The specimen was unloaded from 2400 lbs and reloaded to 2500 lbs. (Corroborative Data - For Information Only)

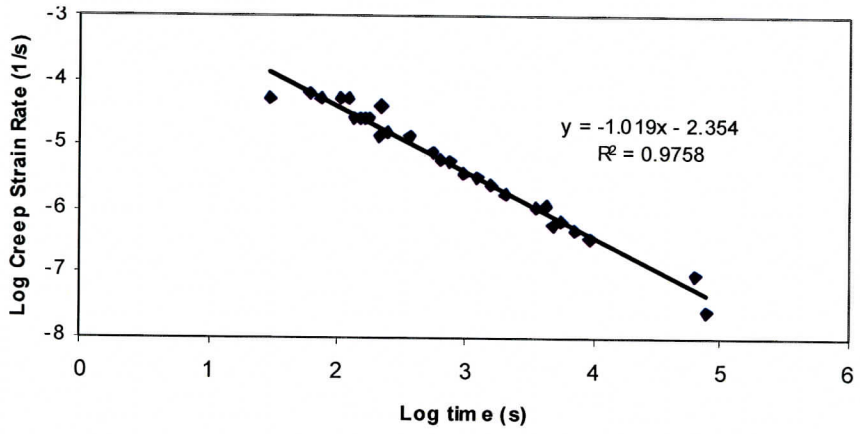

Figure. 4.9(a) Decreasing creep strain rate with time of 304 SS (sensitized) in 0.5 N $Na_2S_2O_3$ at 30°C at a constant load of 2200 lbs (OCRE test condition). (Corroborative Data - For Information Only)

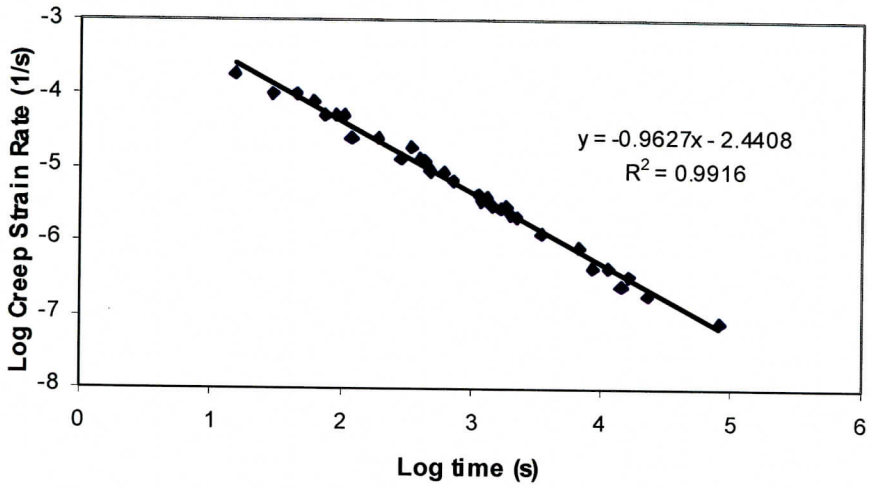

Figure. 4.9(b) Decreasing creep strain rate with time of 304 SS (sensitized) in 0.5 N $Na_2S_2O_3$ at 30°C at a constant load of 2400 lbs (OCRE test condition). The specimen was unloaded from 2200 lbs and loaded again to 2400 lbs. (Corroborative Data - For Information Only)

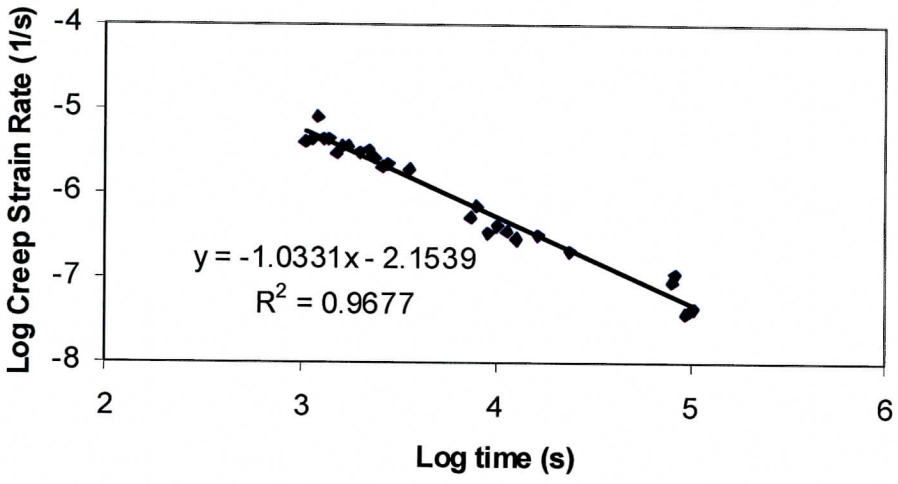

Figure. 4.9(c) Decreasing creep strain rate with time of 304 SS (sensitized) in 0.5 N $Na_2S_2O_3$ at 30°C at a constant load of 2500 lbs (OCRE test condition). The specimen was unloaded from 2400 lbs and loaded again to 2500 lbs. (Corroborative Data - For Information Only)

Non-Q: 5. SUBTASK 2:Seismic Enhancement of Corrosion Fatigue in Alloy-22

Prediction of Long-Term Ground Motions in the Potential Repository

This subtask consisted of the following steps: 1) the prediction of seismic activity at the repository, 2) Finite element modeling of the Waste Package (WP) containers to determine the loading of the WP containers due to seismic activity, and 3) experimental determination of the corrosion fatigue behavior of Alloy-22 due to cyclic seismic loading. While step one was completed on schedule, it was found that development of a qualified finite element model of the Waste-Package container could not be completed within the contract performance period. DOE has developed a qualified finite element model of the Waste Package container, and permission to use this model to continue the subtask was requested. However, national security concerns delayed the release of the model to UNR beyond the time available for performance of the contract. Because of this delay none of the planned experimental work could be conducted, since results from the finite element model were required for experimental design of this task. It was planned to use initial experimental results from the corrosion fatigue behavior of Alloy-22 to re-visit the predictions of seismic activity. The data for seismic activity predictions presented in this section were generated using arbitrary cutoffs for frequency and amplitude. The experimental results obtained would be essential in addressing what frequency and amplitude ranges would prove to be the most critical to the lifetime predictions of Waste Package containers. Therefore, this section was not qualified as per QAP-3.3 since the experimental results needed to complete the model were unavailable due to the delays in obtaining the Finite Element Model Mesh from the DOE.

5.1 Outline of the Approach

The goal is to realistically predict the ground motion at various frequencies of engineering interest in the potential repository at Yucca Mountain. This involves estimating the characteristics of earthquakes whose ground motion may have a potentially damaging affect on the caskets over a time period of 10,000 years; for purposes here, we assume that the minimum damaging effect has a threshold of 0.001 g (1 g = acceleration of earth's gravity field at the surface ~ 980 cm/s^2). The essential characteristics will be the recurrence times of such earthquakes, their time-domain and spectral-domain amplitudes at the potential repository, and the effective duration of motion. The estimation of these parameters invokes a number of assumptions, approximations, and empirical relations in seismology. We are guided, to some extent, by the volume of Wong and Stepp (1998)[69] who presented the work of many "experts" on ground-motion predictions at the potential repository. The results of that work are presented as peak ground accelerations (PGA) and as spectral accelerations versus magnitude and distance of earthquakes from the repository. The one parameter missing

[69] Wong, I. G., and J. C. Stepp, 1998. Probabilistic seismic hazard analysis for fault motion displacements and vibratory ground motion at Yucca Mountain, Nevada: Final Report, Yucca Mountain Project, Las Vegas, Nevada (MOL #19980619.0640).

from their predictions is the duration of ground motion, an important parameter for stress-corrosion testing of materials that might be used in fabrication of actual waste caskets. Peak acceleration times duration would more validly represent the possible damage to casket materials, especially in the case of cumulative effects from repeating earthquakes. The caskets must be able to withstand stress fracturing under possibly corrosive conditions over the 10,000-year critical, highly radioactive part of the repository's life.

5.2 Hypothetical 10,000-Year Catalog of Earthquakes

The objective then is to estimate the entire suite of ground motion produced by earthquakes, occurring anywhere, at Yucca Mountain. There are at least two approaches to this estimation. One would be to take actual seismograms recorded at Yucca Mountain for different magnitudes and source regions and to utilize these, or slight variations of such, many times over to simulate what may happen in 10,000 years. The problem with this approach is that the history of seismic recording at Yucca Mountain is very short, starting in the late 1970's. High-resolution, 3-component digital recordings have only been available since 1996 at Yucca Mountain. With this limited span, the extant recordings represent only a tiny fraction of the ground-motion time series that would be recorded over a 10,000-year period. Many of the important source regions are not yet represented in the extant recordings, and certainly most of the major or great earthquakes are not represented. The second approach, which we will take, is to create a 10,000-year catalog of earthquakes and then to simulate the ground-motions at Yucca Mountain from those earthquakes.

To do this, we begin by creating a hypothetical 10,000-year catalog of important earthquakes, applying the minimum 0.001 g criterion. The catalog is most suitably generated from the statistics of known earthquake activity although long-term geologic evidence and modern geodetic evidence are often used to predict the long-term recurrence rates of large earthquakes. As we shall show later, only earthquakes within roughly 1000 km need to be considered in the generation of a catalog whose events are significant at Yucca Mountain. The known instrumental catalog spans little more than a century in the nearby source regions of the western United States, notably California. Near Yucca Mountain itself, the instrumental records only spans a few decades for earthquakes that may cause 0.001 g at Yucca Mountain. The 10,000-year catalog will be generated from our current best knowledge of activity.

A concept that is very helpful in generating the 10,000-year catalog is the basic recurrence rate of earthquakes. Earthquakes follow a power law on magnitude given conventionally as:

$$\log_{10} N = a - b\,M$$

where N is the number of earthquakes at a given magnitude M. The constants *a* and *b* are determined empirically from catalogs of actual earthquakes. Remarkably the slope *b* is fairly consistently in the range of roughly 0.8 to 1.2. For any given region, it is fairly stable such that even a short-duration catalog can yield a good estimate of *b*.

Mathematical manipulation of the recurrence equation reveals that N taken as the cumulative number rather than the incremental number will also have the same *b* value, excepting the points at large magnitude, but with a new *a* value.

Figure 5.1 shows a simple example of the above equation, but with a threshold imposed on lower magnitudes. This threshold (at M = 1 in the figure) is imposed by the detection capabilities of seismic networks within the noise background field; consequently, the smallest events are never observed. The threshold issue and its effect on the shape of actual recurrence curves is discussed in Von Seggern and Blandford[70] (1976). However, in relation to the discussion here, the instrumental detection threshold will be everywhere below the magnitudes of earthquakes capable of causing 0.001 g at Yucca Mountain. Although the behavior of the recurrence curves at small magnitude is understood in relation to threshold, the behavior at larger magnitudes is somewhat controversial although it is widely held, on a physical basis, that there is a cutoff at high magnitudes. This cutoff is effected by a rolloff appearance to the recurrence curve. Within instrumental time, the largest earthquake ever recorded was M 9.6 off the coast of Chile in 1960. Within a geologic context, every earthquake source region would seem to have an upper cutoff to the largest earthquake size based on the maximum extent of known faults or possible faults supported by the tectonic scale lengths of that region. Such cutoffs are extremely important in forming a 10,000-year hypothetical catalog of earthquakes and will be taken into account here. It is not possible to obtain 10,000-year information from our meager instrumental, or even historical catalogs; and so these cutoffs will be somewhat arbitrarily imposed.

To produce a 10,000-year catalog, we begin with a 25-year catalog (1978-2002) of instrumental seismicity. We started with the ANSS (Advanced National Seismic System) catalog. This catalog replaces the NEIC (National Earthquake Information Center) and includes both U. S. and worldwide earthquakes. The threshold of this catalog will be low enough that it will reliably report all earthquakes whose ground motion could exceed 0.001 g at Yucca Mountain, except for a very few which can be incorporated from the instrumental catalogs of the Yucca Mountain seismic networks. The latter catalog comes from our own work at the NSL (Nevada Seismological Laboratory) for the years 1993-2002 and from previous work of the USGS for the period 1978-1992. As with almost all catalog compilations, numerous problems with the data needed to be handled. Nuclear events, duplicate earthquakes, bogus earthquakes, and so forth, were carefully removed from the composite catalog. For all events, which collated between the ANSS and NSL catalogs, the NSL event was given preference to be in the final 25-year catalog.

Once the 25-year instrumental catalog was finalized, we proceeded to extrapolate it to a 10,000-year catalog using the spatial-temporal-magnitude statistics of the 25-year one. Here we are focusing on one particular point on the earth for ground-motion predictions. We arbitrarily defined it here as 36.8515N, 116.4563W, which is the location of one of the NSL stations directly above the potential repository. Viewing the catalog in terms of this one point, the spatial definition of the events can now be collapsed into distance from

[70] Von Seggern, D., and R. Blandford, 1976. Seismic threshold determination, Bull. Seismol. Soc. Am., 66, 753-788.

this point, and the actual earthquake latitudes and longitudes are irrelevant. (We presume that there are no azimuthal effects relevant to predicted ground motions in reducing the actual event locations into one dimension.) We then seek to determine the constants in the recurrence relation for earthquakes binned into contiguous distance ranges from Yucca Mountain. The binning was done with the following distance boundaries in km: 50, 100, 200, 300, 400, 600, 800, 1000, 1500, 2000, 2500, 3000, 3500, 4000, 5000, 6000, 7000, 8000, 9000, 10000, 11000, 12000, 13000, 14000, 15000, 17000, 20000.

For each of the 27 binned catalogs taken as a separate catalog, the cumulative recurrence data was computed and plotted. From these plots, a lower cutoff in magnitude, the detection cutoff discussed above, was visually estimated in order to exclude data for which the catalogs were less than 100% complete. Using only data above this cutoff, the constants in the recurrence relation were then estimated by the method of Aki[71] (1965). The resulting *a* and *b* values, enable us to extrapolate to 10,000 years the activity seen in the 25-year catalog. These values for the above distance boundaries, starting with 0-50 km, 50-100 km etc, are as follows: (a,b) = (4.8622, 0.9038), (4.6371, 0.8480), (6.0880, 0.9493), (6.5274, 0.9388), (6.4230, 0.9516), (6.5928, 0.9565), (5.6177, 0.7892), (5.7088, 0.7481), (6.8750, 0.9501), (6.0485, 0.7961), (5.8777, 0.7645), (7.1612, 0.9713), (6.7626, 0.8237), (7.5703, 0.9587), (8.1800, 1.0226), (8.5087, 1.0958), (8.6083, 1.0847), (8.7908, 1.0920), (8.9029, 1.0518), (8.7928, 1.0050), (8.6985, 0.9998), (9.3662, 1.1525), (9.3001, 1.1406), (8.1661, 0.9867), (8.7713, 1.1153), (8.8786, 1.2383), (9.3752, 1.3268).

As discussed above, the contribution from distant earthquakes to ground motion at Yucca Mountain is small. In order to measure that empirically, we examined an archive of earthquake recordings for station RPY above the potential repository. These recordings were of large regional and teleseismic events saved over a period of a few years when RPY had a broadband, velocity-response seismometer installed (Guralp CMG-40 with 0.03 Hz corner). We took these recordings, reduced them to ground motion, differentiated to obtain accelerometer-equivalent recordings, and then measured the peak acceleration on the horizontal components. In order to view this data, it is appropriate to normalize the values by the earthquake magnitude. The normalized values are plotted in Figure 5.2. A log-log line has been visually fit to the data up to the distance of 2000 km. Note that, with the exception of a few values, the earthquakes beyond 1000 km have insignificant ground motion compared to earthquakes at less than this distance. Even a magnitude 9 earthquake at a distance of > 2000 km would appear to rarely generate ground acceleration larger than 10^{-3} g ($10^{-12} * 10^{9}$), the criterion ground motion. We have thus limited our hypothetical catalog to just earthquakes at < 2000 km from Yucca Mountain.

The 10,000-year catalog is then created by merging separate catalogs generated up to the 2000-km cutoff, for each of the distance ranges as: 0-50 km - 7.0, 50-100 km - 7.5, 100-200 km - 7.5, 200-300 km - 7.5, 300-400 km - 8.0, 400-600 km - 8.0, 600-800 km - 8.5, 800-1000 km - 8.5, 1000-1500 km - 8.5, 1500-2000 km - 8.8. For each individual catalog, we use the recurrence-rate constants shown, but multiplying the constant *a* by the

[71] Aki, K., 1965. Maximum–liklihood estimate of b in the formula logÃ = a –bM and its confidence limits, Bull. Earthquake Res. Inst., Tokyo Univ., 43, 237-239.

ratio of 10000/25 = 400 to project from 25 years' actual data to 10,000 years' hypothetical data. Event distance is randomly generated from a uniform distribution of distance throughout the particular distance range. Inter-event times are randomly taken from a Poisson distribution which takes into account the *a* value of the recurrence relation multiplied by 400. Magnitudes are randomly generated consistent with the actual *b* value of the recurrence relation. The following upper magnitude cutoffs as discussed above.

These cutoffs do not have a rigorous basis. They vary from the low of 7.0 in the southern Great Basin near Yucca Mountain where active faulting is thought to be confined to faults of no more than roughly 50 km and therefore incapable of generating M > 7 earthquakes (Wong and Stepp, 1998)[69]. The M 8.8 cutoff in the 1500-2000 km range is for the penultimate Cascadian subduction earthquake off the coast of the state of Washington and Oregon. The lower cutoff was set uniformly at M = 3, recognizing that this quite liberal value allowed the hypothetical catalog to contain many earthquakes whose ground motion at Yucca Mountain would be less than the 0.001 g criterion.

The 10,000-year catalog generated as described above contained nearly 120,000 earthquakes. For comparison, another catalog was generated using no upper cutoffs on magnitude to see what the implications are of extrapolating earthquake recurrence with a constant *b* value. The statistics of the two catalogs are shown in Figure 5.3. The catalog with realistic high-magnitude cutoffs shows a fairly steep falloff due to the M 8.5 restriction in the 600-1500 km range, and the few events at M > 8.5 are due to the presumed penultimate Cascadian events. With roughly 30 of these, the recurrence time over 10,000 years is roughly every 300 years, in fair agreement with geologic evidence for Cascadian events (Goldfinger et al., 2002[72]). The "with magnitude cutoffs" points represent the catalog with realistic limitations on earthquake size, and this catalog has many fewer events at the high magnitudes than simple linear extrapolation along the *b* value would indicate. The result of this, as we shall see, is a corresponding falloff of numbers of high-acceleration events when acceleration predictions are plotted cumulatively in the manner of the magnitude recurrence curve.

5.3 Predicting the Accelerations at Yucca Mountain from the 10,000-Year Catalog

Given the 10,000-year catalog of earthquakes, each with a magnitude and a distance from Yucca Mountain, we use published empirical acceleration curves to estimate the likely PGA and the likely spectral accelerations at Yucca Mountain for each event in the catalog. Due to the very limited amount of actual data that has been used in determining these curves, this step entails considerable uncertainty in our process of predicting a 10,000-year history of acceleration at Yucca Mountain.

For distances < 100 km, we use results from the PSHA study (Wong and Stepp, 1998[69]). Further, we have picked only one set of regression coefficients from among the six "experts" contributing to that study. We use Anderson's coefficients in the "median

[72] Goldfinger, C.; C. H. Nelson; and J. E. Johnson, 2002. Geological Society of America, Cordilleran Section, 98th annual meeting, Abstracts with Programs - Geological Society of America, vol.34, no.5, p.36.

attenuation" relation (equation 6-1a in the PSHA study) and do not include any effects due to normal faults versus strike-slip faults; in other words, all events in the 10,000-year catalog are considered to have strike-slip mechanisms. Surely this is a simplification, but the hypothetical catalog does not contain information on focal mechanism; to generate such information would entail another level of analysis with probably no significant effect on the final outcome. We took the Anderson coefficients from Table I-1A (vertical motion in the PSHA study) for PGA and for the spectral frequencies 0.3, 0.5, 1, 2, 5, 10, and 20 Hz. Horizontal motion coefficients are also given; however, there is no significant difference between results using horizontal and vertical coefficients, given the levels of uncertainty for other steps in our estimation scheme.

For distances > 100 km, we use the coefficients developed by Atkinson and Boore[73] (1997, hereafter labeled "A-B") for PGA and for spectral accelerations at the same frequencies as used for < 100 km. A major adjustment was then performed in recognition of the fact that the A-B coefficients came largely from attenuation of earthquake waves in the central and eastern United States. Because such attenuation is not appropriate for earthquakes at regional distances in the western United States, we merely tied the A-B amplitude-distance relations to the Anderson ones at 100 km by determining the constant which, when divided into the A-B prediction, gave the Anderson prediction at 100 km. These constants for various frequencies are as follows: PGA-10.9, 20Hz-15.6, 10 Hz-7.98, 5 Hz-4.54, 2 Hz-0.62, 1 Hz-1.35, 0.5 Hz-1.09, 0.3 Hz-2.02. The effect is, in each case except one, to lower the A-B values.

Note that the factors are large for high frequencies and roughly unity for the lower frequencies, as expected for attenuation that is variable with frequency. The prediction of PGA and spectral accelerations was then programmed according to this scheme, and the entire 10,000-year catalog was run through the program to produce predicted accelerations for each event.

One additional important parameter was estimated within the prediction program: the duration of motion at Yucca Mountain for each event. Using such an estimate, the spectral accelerations can be applied in stress-fatigue testing as a harmonic wave of the predicted duration. Thus the cumulative stress damage at any given frequency could be determined in the lab with suitable samples subjected to the motions prescribed by the 10,000-year catalog of earthquakes. For any given earthquake, we initially estimate the duration to be from the P arrival time through the Lg phase at 3.0 km/s. This is sufficient for earthquakes whose rupture length is small compared to the epicentral distance to Yucca Mountain. For larger ruptures, an additional quantity of time based on magnitude should be added. We estimate rupture length L from the work of Wells and Coppersmith (1994)[74] as

$$L\ (\text{km}) = 10^{\,0.59*M - 2.44}$$

[73] Atkinson, G. M., and D. M. Boore, 1997. Some comparisons between recent ground-motion relations, Seismological Research Letters, 68, 24-40.

[74] Wells, D. L., and K. J. Coppersmith, 1994. New empirical relationships among magnitude, rupture length, rupture width, rupture area, and surface displacement, Bull. Seismol. Soc. Am., 84, 974-1002.

This gives, for instance, a 375-km rupture for an M = 8.5 strike-slip earthquake. From the rupture length, we estimate the additional duration by taking the length divided by a crustal fault rupture velocity of 3.5 km/s. This figure would be reduced by a fault geometry that was aligned along the path to Yucca Mountain; but, as for focal mechanism, we have no such information in our hypothetical 10,000-year catalog to do this adjustment and so use the crudely calculated value. The formula for duration in seconds is then

$$D = R/3.0 - R/8.0 + L/3.5$$

where R is the epicentral distance in km. A value of 6.0 km/s would be better than 8.0 km/s for earthquakes closer than about 130 km (Pg to Pn crossover) but the difference is only a few seconds, well within the uncertainties caused by other unknowns in this scheme.

The predicted values of duration and acceleration (PGA and spectral in units of g) are output for every earthquake in the 10,000-year catalog to complete the ground motion prediction at Yucca Mountain for use in the stress-fatigue testing. Figure 5.4 shows the cumulative curve of PGA's that resulted from this prediction exercise. Note that the curve shows a constant slope consistent with a constant *b* value in the range of roughly –3.6 to –2.0 on the $\log_{10}(g)$ scale or, equivalently, 0.0002 g to 0.01 g. The target of including all events producing 0.001 g or greater has been met and exceeded. Several tens of thousands of events with PGA less than this value exist in the catalog and are superfluous. Towards the higher values, the curve falls off rapidly starting at roughly 0.01 g. As indicated above, this behavior is expected due to the corresponding falloff in the recurrence versus magnitude curve in Figure 5.3. The falloff in Figure 5.3 above M 7.5 get translated, in a smeared fashion due to the acceleration-distance relations, into the falloff in accelerations above 0.01 g in Figure 5.4.

From Figure 5.4, we see that the highest acceleration predicted at Yucca Mountain for the 10,000-year interval is roughly 0.4 g. Because the catalog was created with a random-number generator, successive runs would give different results, but unlikely to exceed 1.0 g. Also, no aleatoric variability was imposed on the accelerations predicted for each event. This could provide scatter as large as a factor of ten or more (Wong and Stepp, 1998[69]), thus bringing the largest predicted acceleration to several g. In the context of the purpose of this exercise, to provide input for stress-fracturing tests, inclusion of this random effect does not seem warranted. Given the fact that the largest accelerations occur only a very few times (only about 40 events with > 0.1g in Figure 5.4), adding variation to the predicted accelerations will not significantly affect the stress-fatigue testing results.

Using only those events in Figure 5.4 with PGA > 0.001 g, we have plotted their estimated durations in Figure 5.5 in the manner of an incremental recurrence curve. Note that a relatively large number of short durations exist. The total duration of ground shaking is obtained by multiplying the duration of each bin by the number of events in

the bin. This total is $5.5*10^6$ s for the hypothetical 10,000-year catalog used here. This number of seconds amounts to approximately 64 days, or 0.17 years. This means that, for roughly 0.000017 of the total time, Yucca Mountain would be experiencing ground motions which have, somewhere in the recording, a PGA > 0.001 g. This is not, of course, the same as experiencing that level of PGA or higher for the entire 0.000017 fraction of time. For the durations estimated here, values near the PGA probably only occur for a small window of the predicted duration. The spectral amplitudes would be a more reliable indication of ground-motion over the entire time of the estimated durations.

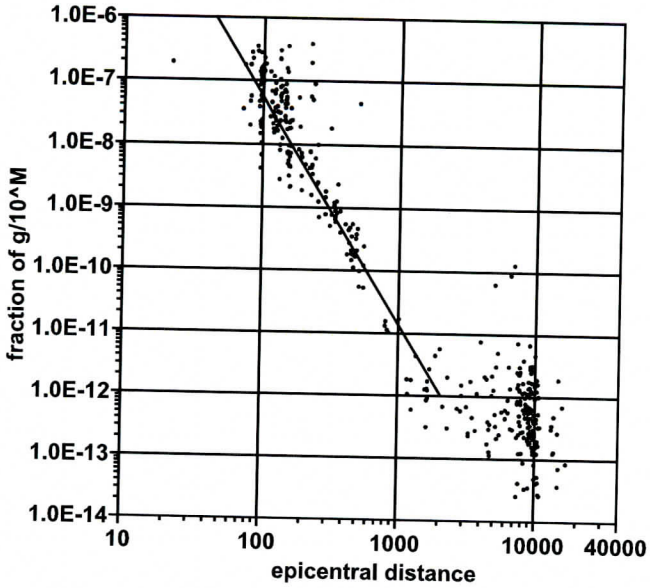

Figure 5.1. Example of power law relationship for earthquakes with a threshold (M=1) imposed on lower magnitudes, showing peak accelerations and epicentral distance for regional and teleseismic events. Accelerations have been normalized by the event magnitude. (Non-Q: For Information Only)

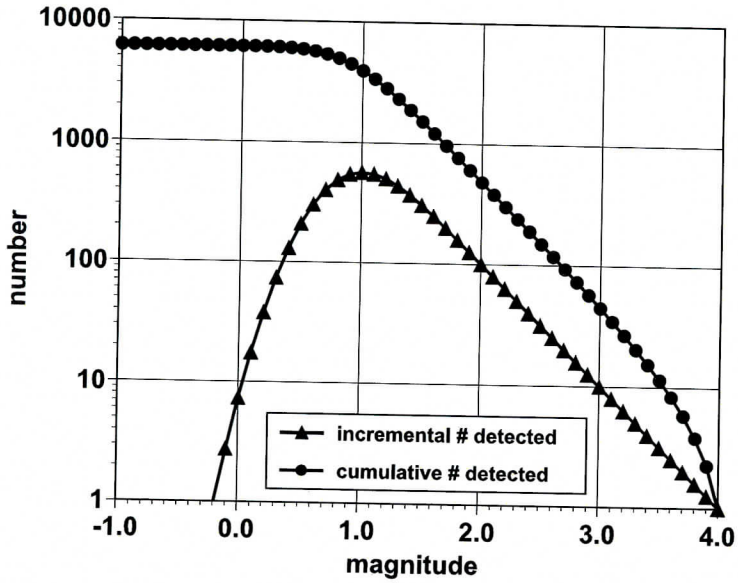

Figure 5.2. Examples of earthquake recurrence curves using $a = 3.0$ and $b = 1.0$ in the recurrence relation. (Non-Q: For Information Only)

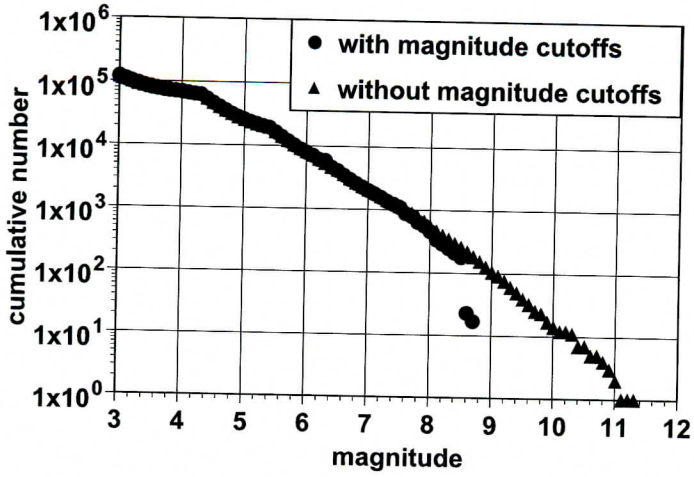

Figure 5.3. Hypothetical recurrence curves which result from either using or not using upper magnitude cutoffs to limit the maximum size of earthquakes in the various source regions. (Non-Q: For Information Only)

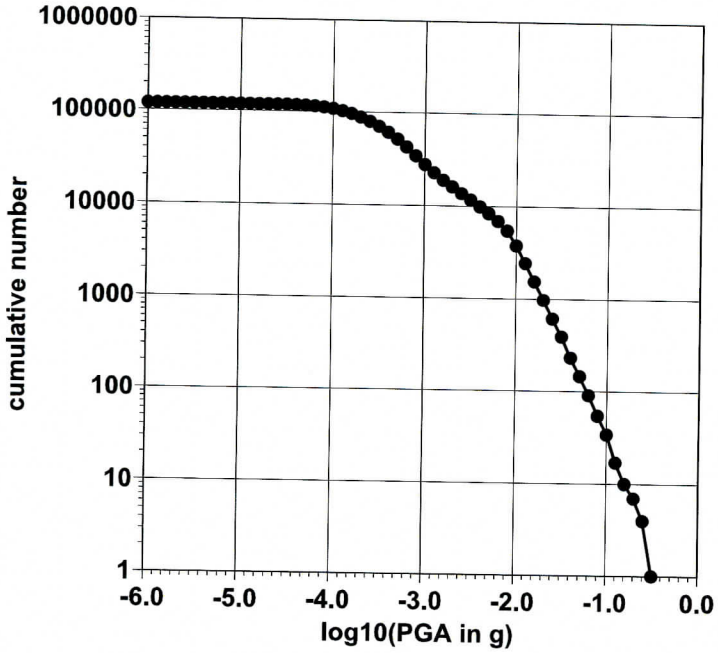

Figure 5.4. Recurrence curve for accelerations at Yucca Mountain from the hypothetical 10,000-year catalog of earthquakes. (Non-Q: For Information Only)

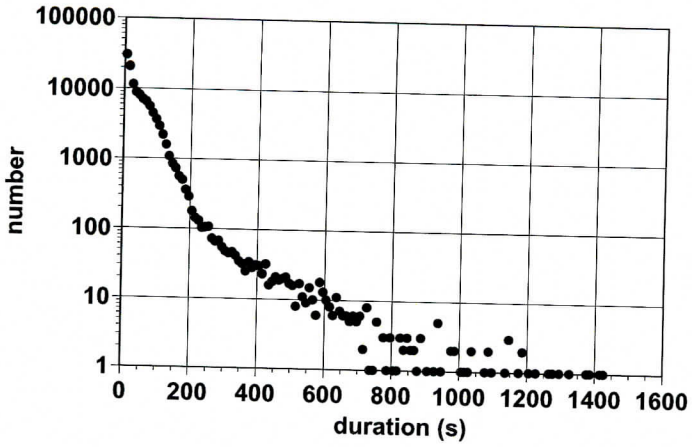

Figure 5.5. Histogram of predicted durations of seismic shaking at Yucca Mountain from the hypothetical 10,000-year catalog of earthquakes. (Non-Q: For Information Only)